DISS. ETH No. 29077

VAN DER WAALS TUNNEL JUNCTIONS FOR LIGHT AND MEMORY

A thesis submitted to attain the degree of

DOCTOR OF SCIENCES OF ETH ZURICH

(Dr. sc. ETH Zurich)

presented by

SOTIRIOS PAPADOPOULOS

Diploma in Electrical and Computer Engineering
Faculty of Engineering
Aristotle University of Thessaloniki

born on 31.07.1988

citizen of Greece

accepted on the recommendation of

Prof. Dr. Lukas Novotny, examiner

Prof. Dr. Stéphane Berciaud, co-examiner

Prof. Dr. David J. Norris, co-examiner

2023

This work was carried out at the
Photonics Laboratory,
Department of Information Technology and Electrical Engineering,
ETH Zurich

Εάν μη έλπηται,
ανέλπιστον ουκ εξευρήσει.
– Ηράκλειτος

If you do not hope for
the unexpected, you will not find it.
– Heraclitus

Acknowledgments

The years of my PhD studies have been one of the most interesting periods of my life. I grew personally and scientifically and this is a result of interaction with many people in many different levels. I will share my gratitude in-person with all the people that played an important role in this journey, however, I would also like to briefly acknowledge here few of them.

First to be mentioned here is certainly Prof. Lukas Novotny who entrusted me with a PhD position in the group and enabled me to work in the field of 2D materials which I very much enjoyed. The working environment he has formed in the group played an important role in my development as both a person and a scientist. Thank you Lukas for your trust and support!

Moving on, I am grateful for the support and the team spirit of the 2D subgroup. I never felt alone with such great colleagues that could so effectively absorb problems and frustration but were also able to share moments of joy and success. Klaus, Markus, Sebastian, Achint, Anna, Ronja, Shengyu, Lujun and Antti, thank you!

Moving on, it is true that nothing would have been the same without my groupmates, bandmates and friends Fons and Alfonso. You made the difficult and stressing periods much more tolerable with your great character and companion. Thanks a lot!

I would also like to acknowledge here the support from Dr. Alexandros

Emboras and Prof. Mathieu Luisier. Thank you for always being available to discuss and share your knowledge and opinion.

In addition, I want to thank Barbara for tackling successfully all the administrative hustle and complexities that appeared throughout the years. Barbara, I am always surprised with how you do this so well and I wanted to thank you for your support and confidence that made everything so much easier and sometimes even fun!

Moreover, I would like to express my sincere gratitude to the whole Photonics Laboratory for such a helpful, supportive and fun working environment. I feel lucky to have been given the chance to work with all of you. It has been a great pleasure to spend these years together.

I also want to thank Prof. David Norris and Prof. Stéphane Berciaud for participating in my PhD examination committee and for providing useful comments and corrections for the final version of my thesis.

Finally, I want to thank my family and friends for their tireless support throughout all the years. I could only manage this because I knew you were there for me if I needed it. Thank you!

Abstract

The isolation of two-dimensional (2D) materials, crystals thinned down to one atomic layer, captured the interest of the scientific community and provoked substantial research efforts during the last two decades. With the increasing technological demands of modern society, 2D materials have emerged as an alternative platform that holds potential for tackling the challenges of the future. The possibility of incorporating different materials into heterostructures opened up an unforeseen prospect for innovation in various technological disciplines. In this work, we experimentally explore electrically driven light emission and memory applications by employing insulators, conductors and semiconductors from the family of 2D materials. First, we investigate light emission from tunnel junctions that are optically coupled to 2D semiconductors and we demonstrate a novel way for driving light emission in these materials, namely through energy transfer from tunneling electrons to excitons. In addition, we explore the transport characteristics of such devices and we observe strong conductance resonances due to increased coupling to the excitonic states, demonstrating in that way all-electrical measurements of optical properties. Finally, we expand the spectrum of the investigated phenomena by studying non-volatile memory devices (memristors) with 2D semiconductor tunnel junctions. More specifically, we explore experimentally and theoretically the role of crystal defects in the memristive performance, revealing in that way a defect density range for optimized operation. This work explores the diversity of physical phenomena that can be probed within the 2D material platform, with the prospect of new discoveries and innovative applications for the technology of the future.

Zusammenfassung

Die Isolierung von zweidimensionalen (2D) Materialien, d. h. von Kristallen mit der Dicke von einer Atomschicht, hat das Interesse der wissenschaftlichen Gemeinschaft geweckt und in den letzten zwei Jahrzehnten zu erheblichen Forschungsanstrengungen geführt. Angesichts der steigenden technologischen Anforderungen der modernen Gesellschaft haben sich 2D-Materialien als alternative Plattform erwiesen die Herausforderungen der Zukunft zu bewältigen. Die Möglichkeit, verschiedene Materialien in Heterostrukturen einzubauen, eröffnet ungeahnte Perspektiven für Innovationen in verschiedenen technologischen Disziplinen. In dieser Arbeit erforschen wir experimentell die elektrisch angetriebene Lichtemission und Speicheranwendungen unter Verwendung von Isolatoren, Leitern und Halbleitern aus der Familie der 2D-Materialien. Zunächst untersuchen wir die Lichtemission von Tunnelübergängen, die optisch mit 2D-Halbleitern gekoppelt sind. Durch den Energietransfer von tunnelnden Elektronen zu Exzitonen zeigen wir anschliessend einen neuartigen Weg, um die Lichtemission in diesen Materialien anzutreiben. Darüber hinaus erforschen wir die elektrischen Transporteigenschaften solcher Bauelemente und beobachten starke Leitfähigkeitsresonanzen, welche auf eine verstärkte Kopplung mit den exzitonischen Zuständen zurückzuführen sind, und demonstrieren auf diese Weise rein elektrische Messungen der optischen Eigenschaften. Zuletzt erweitern wir das Spektrum der untersuchten Phänomene, indem wir nichtflüchtige Speicherbauelemente (Memristoren) mit 2D-Halbleiter-Tunnelübergängen untersuchen. Namentlich erforschen wir sowohl experimentell als auch theoretisch die Rolle von Kristalldefekten für die memristive Leistung und ermitteln dadurch einen Defektdichtebereich für

einen optimierten Betrieb. Diese Arbeit erforscht die Vielfalt der physikalischen Phänomene, die innerhalb der 2D-Materialplattform erforscht werden können, mit der Aussicht, neue Entdeckungen und innovative Anwendungen für die Technologie der Zukunft zu ermöglichen.

Foreword

The work presented in this thesis would not have been possible without contributions from several people. First to be mentioned here is Dr. Lujun Wang, with whom we worked closely together on 2D material light emitting devices. Lujun exfoliated most of the hBN flakes used in the devices presented in chapters 3, 5 and 6 and along with contributions from Jing Huang and myself, he fabricated the devices whose transport measurements appear in Fig. 6.3. The temperature dependent measurements in the same figure were performed by Dr. Jian Zhang from EMPA. Moreover, I received valuable input from Prof. Javier Garcia de Abajo and Dr. Fadil Iyikanat for understanding the results presented in chapter 6. Fadil also provided calculated dielectric functions of MoS_2 monolayers used in calculations in chapter 4. Furthermore, I am grateful to Dr. Achint Jain for providing broad knowledge in 2D material stacking techniques as well as for his support in electron-beam lithography for the fabrication of the gold evaporated device presented in chapter 7. In addition, I received great support and useful advise from Dr. Alexandros Emboras and Paul Lehmann on memristor measurements as the ones presented in chapter 7. Moreover, Prof. Mathieu Luisier provided valuable insight for understanding many details of the thesis and helped interpreting experimental results in chapter 3 and chapter 7. Prof. Tarun Agarwal performed *ab-initio* quantum transport simulations used in Fig. 7.6d. Moreover, the spectra presented in this work are corrected for the transmission characteristics of the optical setup based on measurements performed by Anna Kuzmina and Yesim Koyaz. I also want to mention the

rest of the 2D subgroup in the Photonics Lab for providing experimental help and support through meetings and discussions. This includes Antti Moilanen, Ronja Khelifa, Anna Kuzmina, Shengyu Shan, Markus Parzefall, Sebastian Busschaert, Patrick Back and Nikolaus Flöry. Also, Antti Moilanen proofread big part of the thesis and gave valuable comments. Finally, I am grateful to Ronja Khelifa for meeting with me daily and discussing issues related to the thesis writing process.

Contents

1

Introduction

The technological developments in communications, computation and memory platforms of the past century sparked a new era in humanity in which information is massively exchanged and rapidly analyzed. Such developments have had enormous impact at a scientific, societal and economical level that completely reformed our civilization. Under increasing needs, however, physical limitations, like energy consumption constraints [1] or Moore's law expiration [2], inhibit further progress. While emerging technologies, like neuromorphic computing [3] or photonic quantum information processing [4] suggest fundamentally new architectures for a new sustainable technological revolution, the need for novel miniaturized solutions in memory and light processing increases. During the last decades, the rise of a new class of materials that can be thinned down to one atomic layer, attracted the attention of the scientific community. Due to their reduced dimensionality are called "two-dimensional" (2D) materials. These materials have inspired extensive research with the promise of resolving the challenges towards a new technological era, currently at its dawn. In this chapter we give a brief introduction to the 2D materials relevant to this work.

1.1 The rise of 2D materials

In 2004 graphene, an atomically thin sheet of carbon atoms, was isolated for the first time in the lab [5]. Graphene, with its remarkable mechanical, thermal, electronic and optical properties, [6] quickly became the main research field for many academic and industrial laboratories. It was discovered that one can easily mechanically exfoliate graphene flakes on a substrate. Graphene has a hexagonal crystal structure with two carbon atoms in the unit cell (Fig. 1.1a) and exhibits a linear dispersion around the K point of the Brillouin zone as it is illustrated in Fig. 1.1b. This gives graphene good conducting properties while the atomic thickness allows low visible light absorption (2%) [7], making it a candidate for thin transparent electrodes, excellent for optoelectronic applications. A microscope image of a mechanically exfoliated graphene flake is shown in Fig. 1.1c.

A big breakthrough in graphene's experimental research came with the production of high quality, hexagonal boron nitride (hBN) [8, 9]. hBN has the same crystal structure as graphene with a boron and a nitrogen atom at the two sites of the unit cell (Fig. 1.1d). Unlike graphene though, it exhibits strong band-splitting at the K point which provides a bandgap of around 6 eV [10, 11] (Fig. 1.1e). hBN is commonly used as an encapsulating platform ensuring flat and clean interfaces enhancing that way the performance of other 2D materials [9, 12]. In addition, its high bandgap and dielectric constant allows its use as a tunneling barrier in 2D heterostructures [13] or as building block for photonic structures [14, 15]. A microscope image of few layers of hBN is shown in Fig. 1.1f.

The 2D material applications expanded rapidly in the field of optoelectronics with the discovery of a direct bandgap in transition metal dichalcogenide (TMD) semiconductors when thinned down to monolayer form [16]. TMDs have as well a hexagonal crystal structure with one transition metal (M = W, Mo) and two chalcogens ($X = S, Se$) in the two unit cell sites (see Fig. 1.1g). Their bandgap varies between 1-2 eV making them suitable for near-IR and visible spectrum photonic and optoelectronic applications (Fig. 1.1h). Their absorption in the visible makes them easy to spot under the microscope even at the monolayer limit as it is shown in Fig. 1.1i. Light emission from these materials

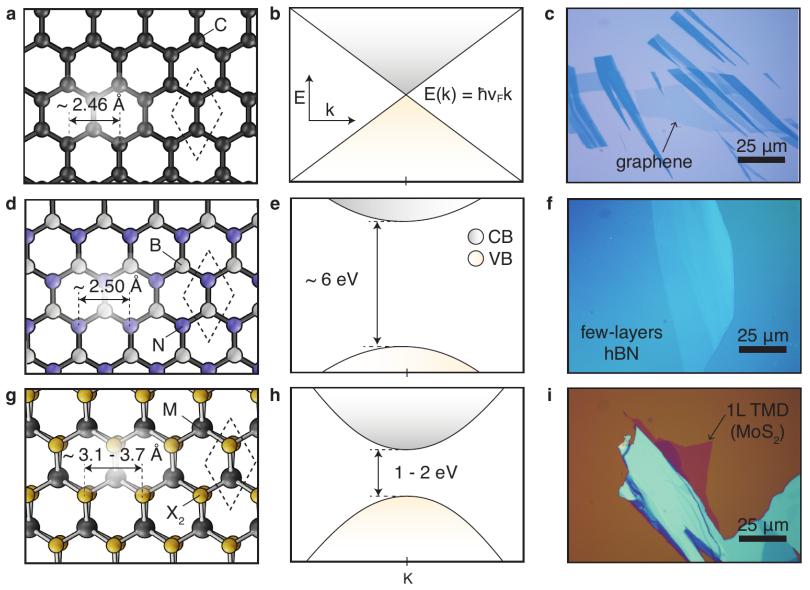

Figure 1.1: (a,d,g) Crystal structure of graphene, hBN and TMDs, respectively. The dashed lines outline the unit cell. (b,e,h) Bandstructures near K point and (c,f,i) microscope images of graphene, hBN and TMD, respectively. All flakes in (c,f,i) are sitting on a Si/SiO_2 substrate.

relies on the formation of electron-hole pair quasiparticles (excitons) with high binding energies [17]. By incorporating these direct-gap semiconductors in graphene and hBN heterostructures, rich electronic and optical phenomena can be investigated.

1.2 Van der Waals heterostructures

The 2D materials presented in the previous section fall into the category of the so-called van der Waals (vdW) materials. This name comes from the fact that in off-plane direction the different layers are held together only by weak vdW forces. For that reason exfoliation down to monolayer limit is possible and stacking of different materials is easily implemented irrespective of their lattice mismatch. This provides seemingly limitless degrees of freedom on building heterostructures that were not possible before with traditional fabrication means. Figure 1.2 shows an impression of the different stacking orders and twist angles that can be achieved with the two-dimensional (2D) platform of vdW materials.

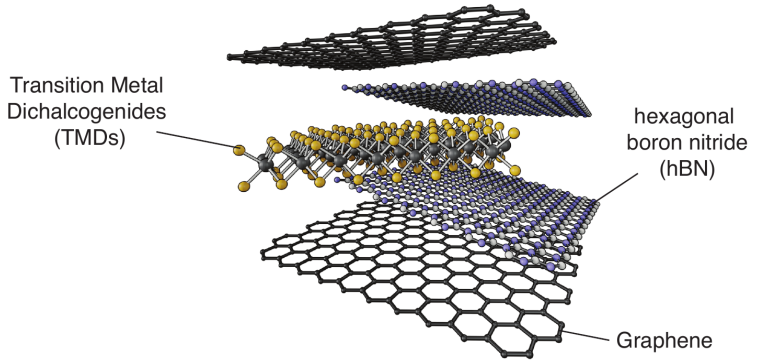

Figure 1.2: A pictorial representation of different 2D materials illustrating the various degrees of freedom in stacking. Angle or crystal lattice matching is not necessary to fabricate stable heterostructures.

1.3 Thesis outline

In this thesis we use the 2D platform to investigate different optoelectronic and ion migration phenomena in vdW vertical tunnel junctions. The devices presented throughout the text are all based on TMDs, hBN and graphene layers. By simply changing the material configuration and stacking, we are able to study various physical processes. Figure 1.3 presents schematics of various devices studied in this work associated with the processes they involve. Graphene is mainly used as a transparent electrode and hBN as a tunneling barrier or as a spacer for electrical decoupling. The TMD is used as the optically active material and in the case of ion migration studies is the receiver of Au ions in its defect sites. The numerous degrees of control in fabricating vdW heterostructures allows us to probe mechanisms or avoid others in order to shed light in new exciting observations. A brief description of the chapters follows.

In **Ch. 2** we make a brief introduction to TMDs with an emphasis on their optical properties. We present measurements of photoluminescence (PL) spectra and we study the impact of defects on PL efficiency. We expand this study to heterostructures where charge and energy transfer phenomena impact the PL efficiency of TMDs as well.

In **Ch. 3** we introduce some basics on electrically driven light emission from metal-insulator-metal tunnel junctions and we complement the theory

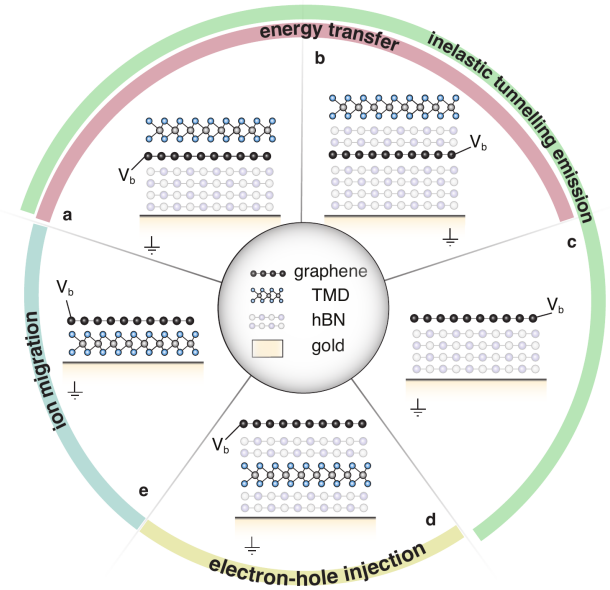

Figure 1.3: A summary of devices presented in this thesis with the associated mechanisms for every device. The 2D material platform enables us, with only four different materials (graphene, TMD, hBN and gold), to investigate charge and energy transfer, inelastic tunneling emission, electron-hole injection and ion migration effects.

with experimental results on Gr/hBN/gold tunnel junctions. Later, we introduce the concept of a double-barrier light emitting device where the light emission is facilitated by the use of monolayer TMDs. We demonstrate polarity dependent emission wavelength and below electronic bandgap threshold voltage.

In **Ch. 4** we study the local density of optical states (LDOS) in multilayer systems. We use the simple example of a dipole coupled to a gold surface to discuss the various optical modes that are present. Then we progress to LDOS calculations of TMDs and study the strong LDOS enhancement in nanometric distances.

In **Ch. 5** we study TMD-coupled tunnel junctions where the TMD is situated outside of the tunneling pathway. We experimentally investigate, in that way, the strong LDOS enhancement commented in the previous chapter in electrically driven tunnel junctions. We discover that light emission from the TMD is

possible through energy transfer and that exciton generation is an efficient process owing to the increased LDOS.

In **Ch. 6** we expand our study on TMD-coupled tunnel junctions by looking at electrical transport measurements. We observe conductance peaks at voltages that correspond to the exciton energies of the TMDs. We interpret this behavior as inelastic tunneling current enhancement due to optical coupling to TMD excitons. In that way, we demonstrate an all-electrical measurement of optical properties.

In **Ch. 7** we shift our attention from light emission to memory applications by studying the memristive characteristics of monolayer TMD tunnel junctions. We explore, experimentally and theoretically, the role of crystal defects in the performance of monolayer MoS_2 memristors based on ion migration.

In **Ch. 8** we make a summary of the main results presented in this thesis and we give an outlook for future investigations.

2

Transition Metal Dichalcogenides

In this chapter we focus on some fundamental properties of TMD monolayers. First, we briefly comment on their optical properties which are affected strongly by excitons with high binding energies. Later, we discuss the effect of defects in PL efficiency and how this can act as a relative measure for the TMDs defect density. Lastly, we discuss charge and energy transfer mechanisms in a TMD/graphene/hBN system.

2.1 Optical properties

In semiconductors excited electrons can bound with holes due to Coulomb attraction and form quasi-particles called excitons [18]. In TMD monolayers, excitons have very high binding energy due to reduced dielectric screening [17]. This allows us to distinguish excitonic peaks at the absorption spectra even in room temperature. The optical properties of TMDs are dominantly defined by the available excitonic states [19]. Figure 2.1a presents an optical absorption spectrum of a monolayer molybdenum disulfide flake (MoS_2). Multiple peaks appear in the spectrum suggesting the existence of excitonic states at different energies. Transition metals in TMDs (typically W or Mo) are heavy elements that lead to increased spin-orbit (SO) coupling [20]. This leads to significant

valence band (VB) splitting at the K point where the direct bandgap of the TMD monolayers is situated. A smaller splitting occurs in the conduction band (CB) that is an order of magnitude lower than the VB splitting [21]. The bandstructure is illustrated in Fig. 2.1b. The VB splitting by Δ_{SO} gives rise to the two peaks observed in Fig. 2.1a. The two excitonic states are referred to as A-exciton and B-exciton with B-exciton having the highest energy between the two. The C peak appears due to the nesting effect between CB and VB from K to Γ point where multiple absorption channels coincide in energy [19] as it is illustrated in Fig. 2.1b.

The direct bandgap of TMD monolayers allows us to study the different excitonic species through PL spectroscopy. Figure 2.1c illustrates the process of photon absorption and emission. When a photon of sufficient energy is absorbed by a TMD, it promotes an electron to the CB and creates a hole at the VB. The electron then thermally relaxes to the bottom of the CB where it recombines with the generated hole. Upon recombination and due to the direct bandgap of TMD monolayers, a photon of energy E_x is emitted. Excitons assume also excited states that can be described by a hydrogenic Rydberg series model with small deviations from it due to dielectric screening variations among the different states [17]. The 1s (ground state) exciton energy is considered the optical bandgap of the material (E_{og}) whereas the distance between CB and VB is the electronic bandgap (E_{eg}) which defines as well the binding energy of the exciton as $E_b = E_{eg} - E_{og}$. The PL spectrum of a MoS_2 monolayer flake is shown in Fig. 2.1d. Multiple peaks contribute to the spectrum. The A and B-exciton peaks are revealed by fitting the spectrum with Voigt functions. The third peak at an energy lower than the A-exciton peak is attributed to trion radiative decay. Trions are charged excitonic species that consist of either two electrons and a hole or two holes and an electron (see Fig. 2.1e).

2.2 Photoluminescence efficiency

In as-exfoliated monolayers the PL efficiency is commonly on the order of 0.01-1% at room temperature [23]. Defects, inhomogeneities and distributed strain can reduce the PL efficiency. However, even pristine crystals suffer from low PL efficiency. At low exciton generation rates (Γ_x) any background carriers favor the transition of excitons to trions which have a high non-radiative

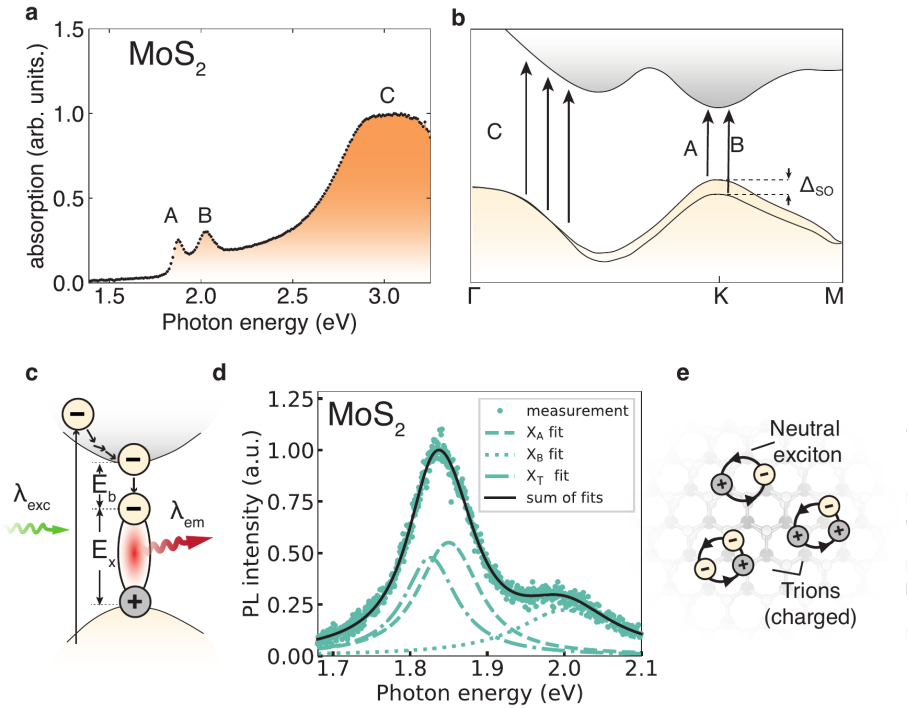

Figure 2.1: (a) Absorption spectrum of a monolayer MoS_2 flake (adapted from [22]) where three distinct peaks are observed. (b) Bandstructure schematic of a monolayer TMD where the main absorption channels are illustrated (A, B and C). Spin-orbit (SO) coupling splits the valence band (VB) at the K point creating two distinct excitonic resonances (A and B) differing by Δ_{SO}. A smaller splitting occurs in the conduction band (CB) that is not included in the illustration. (c) Bandstructure illustration of the photoluminescence (PL) mechanism where a photon of λ=λ_{exc} promotes an electron to the conduction band (CB). After relaxing to the bottom of the CB forms an exciton with energy E_x. When this exciton decays radiatively emits a photon of λ=λ_{em}>λ_{exc}. E_b is the exciton's binding energy. (d) Photoluminescence (PL) emission spectrum of a mechanically-exfoliated MoS_2 flake where the different excitonic contributions are fitted. X_A, X_B and X_T are the A, B-exciton and trion contributions, respectively (λ_{exc}=532 nm). (e) Pictorial representation of the two main excitonic species contributing in the PL spectra, namely neutral and charged excitons (trions).

recombination rate [24]. This limits the PL efficiency. However, reduction of background charges, by electrostatic or chemical doping, can limit trion formation and increase the PL efficiency near 100% [24]. At high Γ_x, exciton-exciton annihilation prevails and radiative recombination is inhibited. It has been shown however, that strain can reduce exciton-exciton interactions by lifting van Hove singularities in the joint density of states leading to increased PL efficiency [25].

2.2.1 Impact of defects in PL efficiency

As commented before, the existence of defects can alter the photoluminescent properties of TMDs. In this section we study how different treatments, namely argon (Ar) sputtering and vacuum annealing, impact the PL spectra of TMDs by introducing different types of defects. Both these methods have previously been shown to introduce defect sites in the MoS_2 crystal lattice [26–28]. The annealing process is illustrated in Fig. 2.2a during which S atoms escape the crystal leaving behind S vacancies (V_s). Fig. 2.2b shows the PL spectra of a monolayer MoS_2 flake before (as-exfoliated) and after two steps of vacuum annealing. Surprisingly, a strong enhancement in PL is observed with increasing annealing time. This enhancement originates from the introduction of V_s sites in MoS_2 upon annealing that act as sites for physisorption of N_2 and O_2 molecules present in air [29]. These molecules lead to an effective p-doping of MoS_2, thereby decreasing the free-electron density, and resulting in a stronger PL emission [24]. It must be noted that this strong PL enhancement cannot be explained by the release of built-in strain and elimination of polymer residues (if any) upon annealing, as these effects were previously shown to not result in any appreciable PL increase in MoS_2 [30]. Finally, the apparent blue-shift of the peak with annealing time relates to the fact that mainly the neutral A-exciton is enhanced by the doping and not the trion contribution, in agreement with previous studies [24]. In case of Ar sputtered MoS_2 flakes (Fig. 2.2c) more extended defects are generated, including MoS_6, Mo and S vacancies [31]. This is supported by the reduced PL emission observed after Ar sputtering as it is presented in Fig. 2.2d, which can be attributed to the formation of more extended defects, resulting in a decrease of the PL quantum yield.

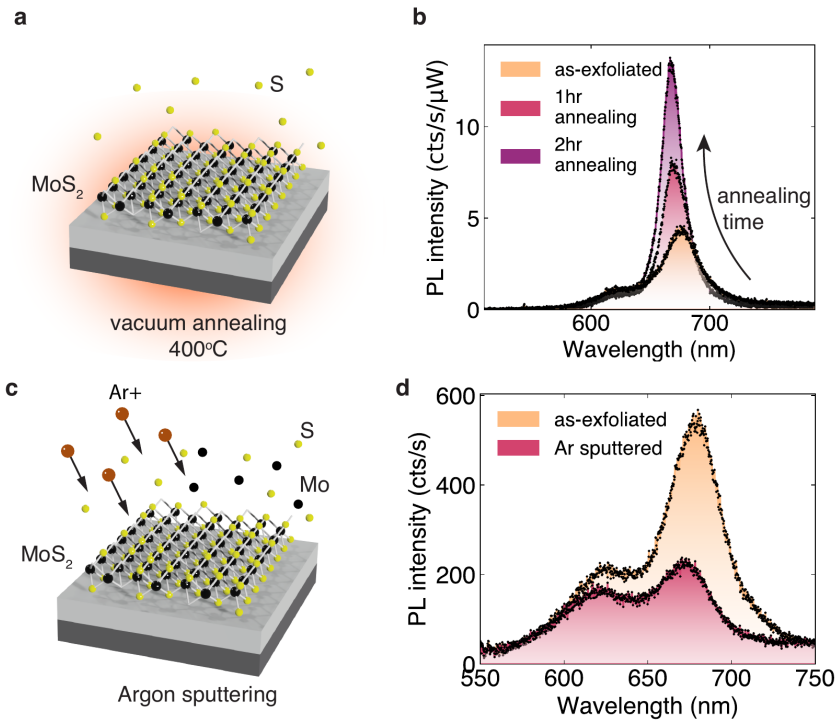

Figure 2.2: (a) A monolayer MoS_2 flake is annealed at 400 °C in vacuum. Under these conditions S atoms escape the crystal lattice leaving behind vacancy sites (V_s). (b) PL spectra of an as-exfoliated MoS_2 flake and after 1 hour and 2 hours of annealing measured in ambient conditions. There is a clear trend of increasing PL due to doping from physisorbed N_2 and O_2 molecules. This behavior indicates the creation of S vacancies. The shoulder close to 620 nm is attributed to B-exciton, which suggests that the emission yield of the A-exciton is low. (c) A monolayer MoS_2 flake is sputtered with Argon forcing S and Mo atoms leave the crystal lattice. This leads to formation of extended defects. (d) PL spectra of an as-exfoliated MoS_2 flake and after Ar sputtering. PL emission decreased after sputtering due to the creation of extended crystal defects.

2.2.2 Charge and energy transfer

In the previous section we discussed how PL is affected by intrinsic properties of the material (defects, doping etc.). However, the electronic and optical environment of a TMD monolayer plays, as well, a significant role in the PL efficiency since it can be inhibited by various effects such as charge or energy transfer mechanisms associated to the surrounding materials.

By providing alternative decay channels for the excited electrons and excitons in the TMD, the radiative electron-hole recombination is quenched. For example in the case of a TMD overlapping with graphene as illustrated in Fig. 2.3a, free electrons and excitons can transfer their energy to the available energetic states of graphene. Fig. 2.3b and c illustrates the processes in a bandstructure schematic. Free electrons (holes) in the the CB (VB) of the TMD find favorable decay channels in the available states of neighboring graphene. This charge transfer process is inhibiting exciton formation and consequently radiative exciton decay [32]. A second process that quenches radiative exciton decay is energy transfer (ET) where the already formed exciton deposits its energy in graphene [33]. Förster type ET * from a donor to an acceptor is mediated by Coulomb interactions via dipole-dipole coupling [34–36]. It is an electromagnetic effect that is dominant at the near-field region of an emitter and has been extensively studied in biological systems [37], molecular assemblies [38], solid-state quantum dots [39] and photosynthetic membranes [40]. It has been also used for color conversion and broadband source design as an energy exchange channel between different fluorophores [41, 42]. Figure 2.3d shows a PL map of the heterostructure illustrated in Fig. 2.3a. At the region where MoS_2 and graphene overlap the PL is much reduced.

Moreover, in the PL map at the hBN layer region, a point-like emission is observed. This emission originates from crystal defects on the hBN flake that provide electronic transitions in the visible spectrum [43, 44]. Interestingly, this defect-related PL emission is also quenched in the region of graphene. The hBN layer is about 10 nm thick. This excludes charge transfer as the quenching mechanism is limited to sub-nm distances [32]. This implies that ET, which can

*Throughout the thesis the term energy transfer (ET) refers to Förster type ET that is different from Dexter type which involves also transfer of charges along with the Coulomb interaction.

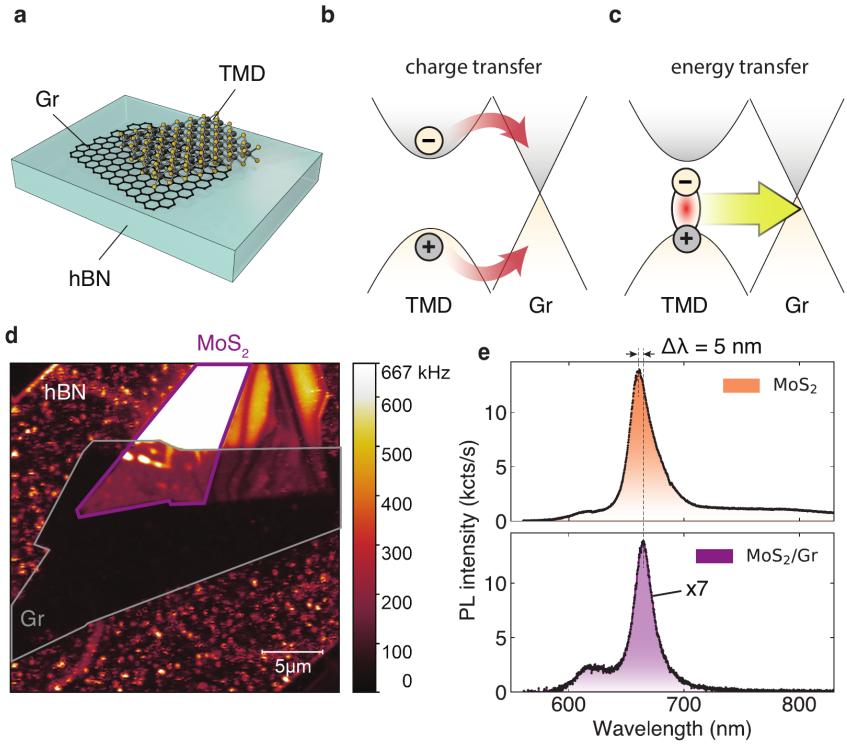

Figure 2.3: (a) A TMD/Gr/hBN heterostructure for studying PL quenching. (b,c) Bandstructure schematics illustrating the (b) charge transfer and (c) energy transfer mechanisms. Both mechanisms reduce radiative exciton decay. (d) PL map of the heterostructure presented in (a). The different flakes are outlined. The scale is saturated for clarity. Real maximum value on map is 1.8 MHz. (e) PL spectra from the area with MoS_2 (top) and MoS_2/graphene (bottom), in which PL is reduced by a factor of 7 and trion contributions have vanished.

span to several nanometers, is the dominating mechanism in the quenching of the hBN PL. In fact, it was shown that ET is the dominant factor of quenching in Gr/TMD systems exhibiting picosecond level response time [45]. Figure 2.3e presents PL spectra from the MoS_2 and MoS_2/Gr regions where a quenching factor of 7 is observed. Moreover, in the MoS_2/Gr case the trion contributions are reduced and the spectrum shows only contributions from neutral excitons, hence the narrower lineshape. Finally, a red-shift of $\Delta\lambda$=5 nm is observed when MoS_2 overlaps with graphene which is attributed to the different dielectric

environment, consistent with previous studies [33, 46].

2.3 Conclusions

In this chapter we discussed the optical properties of TMDs. We studied the impact of defects on the PL efficiency of MoS_2 flakes. By creating extended defects by Ar sputtering, we observed a reduction in PL. However, MoS_2 presented an increase in PL efficiency when treated by vacuum annealing, suggesting pure S vacancy creation. Finally, we discussed the mechanisms of charge and energy transfer in a MoS_2/Gr system and we demonstrated the quenching of PL. The content of this chapter acts as a foundation for various studies presented later in the text.

3

Light emission from van der Waals heterostructures

Electrically controlled photon generation in solid state devices is facilitated by structures that can provide occupied and empty states of electrons with the first ones having higher energy than the second ones. More specifically, an electron from an initial state i with energy E_i and momentum $\mathbf{k}_i$ can decay to an empty final state f with energy E_f and momentum $\mathbf{k}_f$ only if energy and momentum are conserved. When $E_i > E_f$ the electron can inelastically decay to that state assisted by a photon of energy $E_i - E_f$ that conserves the energy of the system. Since photons do not carry significant momentum it should also apply that $\mathbf{k}_i \simeq \mathbf{k}_f$. However, photons are not the only particles that can participate in the interactions but also phonons and/or various types of (quasi)particles such as virtual photons, plasmons or excitons. Light emission from such interactions is facilitated by ultimately coupling to radiative modes (photon modes) as long as the interaction conserves energy and momentum as expressed in the following equations

$$E_i = E_f + \sum_{n=1}^{N} E_n \tag{3.1}$$

$$\mathbf{k}_i = \mathbf{k}_f + \sum_{n=1}^{N} \mathbf{k}_n \tag{3.2}$$

where N is the number of (quasi)particles generated, E_n is the energy and $\mathbf{k}_n$ is the momentum of particle n. The energetic separation of the i and f states is either accomplished by introducing a tunneling barrier between two electrodes under bias (tunnel junction) or by employing semiconductors with direct bandgap in which carriers are injected by two electrodes. Both practices are investigated experimentally in this chapter, by employing the 2D materials platform.

3.1 Light emitting tunnel junctions

Metal-insulator-metal (MIM) tunnel junctions are a simple system where energetic separation of the electronic states is possible, in order to provoke photon emission through the energy conservation requirement. In this section we briefly describe the process of elastic and inelastic tunneling in such structures.

The band diagram of an MIM tunnel junction under bias is shown in Fig. 3.1a. The bias voltage V_b separates the Fermi levels in the two sides of

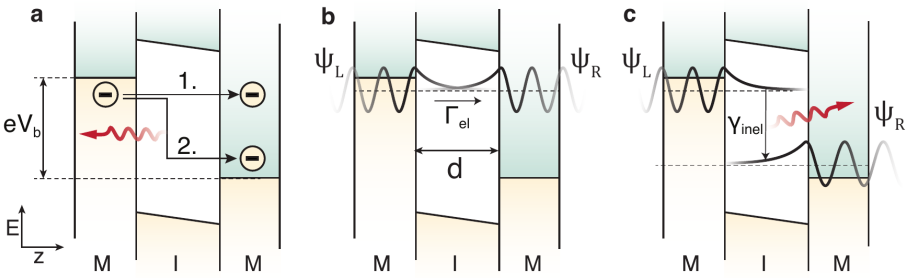

Figure 3.1: Band diagrams of a metal-insulator-metal (MIM) tunnel junction under bias V_b. (a) Electrons can tunnel elastically (1.) or inelastically (2.) by coupling their energy to optical modes. (b) Electron wavefunctions, during elastic tunneling, of an empty state at the left electrode ψ_L and an unoccupied state at the right electrode ψ_R of same energy. Both states define the transfer matrix element $\mathcal{T}$ in Eq. 3.4. (c) Electron wavefunctions, during inelastic tunneling, of an occupied state at the left electrode ψ_L and an empty state at the right electrode ψ_R of lower energy. Both states define the momentum matrix element $\mathcal{P}$ in Eq. 3.6. Γ_{el} is the elastic tunneling rate and γ_{inel} is the spectral inelastic tunneling rate density.

the junctions by eV_b. This applied field forms an energetic landscape in which occupied electron states on the left side have higher or equal energy compared to empty states on the right side. This allows electrons to tunnel from left to right. Electrons are tunneling elastically when they tunnel to a state of same energy (process 1. in Fig. 3.1a) or inelastically when they tunnel to a state of lower energy (process 2. in Fig. 3.1a). In the following sections we briefly mention the fundamentals of the two processes.

3.1.1 Elastic tunneling

Elastic tunneling from a state ψ_L to a state ψ_R of same energy as illustrated in Fig. 3.1b is possible if the two states agree in momentum which is fulfilled if the Fermi-surface of the two electrodes overlap in k-space. Following Eqs. 3.1 and 3.2 this yields $E_i = E_f$ and $\mathbf{k}_i = \mathbf{k}_f$. Such an elastic process does not couple to any other modes including photons. The tunneling rate of this process, in the weak-coupling regime, can be described by the following equation [47]

$$\Gamma_\mathrm{el} = \frac{2\pi}{\hbar} \int_0^{eV_\mathrm{b}} |\mathcal{T}(E)|^2 \rho_\mathrm{R}(E) \rho_\mathrm{L}(\mathrm{E}) dE \tag{3.3}$$

where ρ_R and ρ_L is the electronic density of states (DOS) at the right and left electrode, respectively and $\mathcal{T}(E)$ is the transfer matrix element which is calculated by [47, 48].

$$\mathcal{T}(E) = \frac{\hbar^2}{2m} \left[\psi_\mathrm{R} \frac{d\psi_\mathrm{L}^*}{dz} - \psi_\mathrm{L}^* \frac{\psi_\mathrm{R}}{dz} \right]_{\mathrm{z=z_0}} \tag{3.4}$$

where $\mathrm{z_0}$ is an arbitrary point between the two electrodes.

3.1.2 Inelastic tunneling

Inelastic tunneling from a state ψ_L to a state ψ_R of lower energy as illustrated in Fig. 3.1c occurs when the tunneling electron can couple to other available modes of the enviroment (photons, phonons, etc.). In our analysis we discuss the interaction with optical modes. In this case Eqs. 3.1 and 3.2 are written as $E_i = E_f + E_\mathrm{photon}$ and $\mathbf{k}_i = \mathbf{k}_f + \mathbf{k}_\mathrm{photon}$. Since $\mathbf{k}_\mathrm{photon}$ momentum is much lower than $\mathbf{k}_f$ we assume that momentum is conserved if the two electronic states agree in momentum ($\mathbf{k}_i \simeq \mathbf{k}_f$). Then we can simply write the spectral inelastic tunneling rate density, by only considering the difference in energy, as

[47]

$$\gamma_{\mathrm{inel}}(\hbar\omega) = \frac{\pi e^2}{3\hbar\omega m^2 \epsilon_0} \rho_{\mathrm{opt}}(\hbar\omega) \int_{\hbar\omega}^{eV_{\mathrm{b}}} |\mathcal{P}(E,\hbar\omega)|^2 \rho_{\mathrm{R}}(E-\hbar\omega)\rho_{\mathrm{L}}(E)dE \quad (3.5)$$

where $\hbar\omega$ is the photon energy, ρ_{opt} is the local density of optical states (LDOS), m is the electron mass, ϵ_0 is the vacuum permittivity, e is the elementary charge and $\mathcal{P}$ is the momentum matrix element given by [49]

$$\mathcal{P}(E,\hbar\omega) = -i\hbar \int_0^d \psi_{\mathrm{R}}^*(E-\hbar\omega) \frac{d\psi_{\mathrm{L}}(E)}{dz} dz \quad (3.6)$$

where d is the thickness of the tunneling barrier as noted in Fig.3.1b. The total inelastic tunneling rate is then given by integrating over all optical frequencies for a Fermi separation of eV_{b}

$$\Gamma_{\mathrm{inel}} = \int_0^{e\mathrm{V_b}} \gamma_{\mathrm{inel}}(\hbar\omega)\ \hbar d\omega \quad (3.7)$$

Equation 3.5 suggests that γ_{inel} is proportional to the LDOS, meaning that the optical environment of a tunnel junction is responsible for the inelastic part of the tunneling current. The LDOS in the vicinity of metals as in the case of a tunnel junction, is dominated by non-radiative modes like lossy waves or surface plasmon polaritons [50] which decreases the emission efficiency. The use of optical antennas for enhancing the LDOS and the coupling to radiative modes, has been a subject of intense research [51–53]. However, big part of the emission is absorbed due to losses into the metal and the design of optical antennas is limiting the area of emission to their dimensions which lies at the nanometer scale. The 2D material platform provides an alternative to bulk metal electrodes offering at the same time flat interfaces with big tunneling areas of low thickness disorder. With the use of graphene as the top electrode light emission is only lightly absorbed and can be detected in the far-field. In the next chapter we study the light emission from a Gr/hBN/gold tunnel junction.

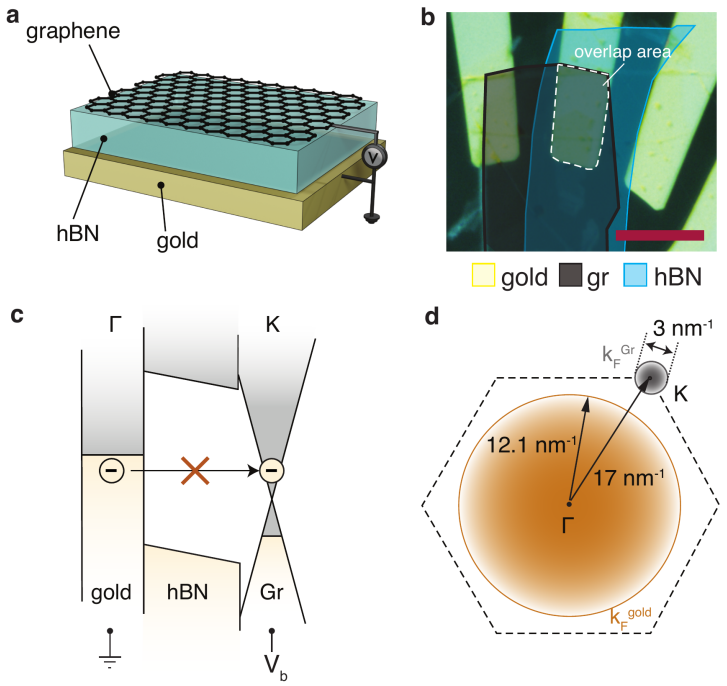

Figure 3.2: (a) Device schematic of a graphene/hBN/gold tunnel junction. (b) Microscope image of a fabricated device where the different flakes are outlined. The overlap area defines the area of transport and inelastic tunneling emission. The scale bar is 12.5 μm (c) Band diagram of the device described in (a). The momentum mismatch between the occupied states in gold and the unoccupied states in graphene doesn't allow elastic tunneling. (d) Projection of golds Fermi surface (orange) and graphene's Fermi surface (black) on the plane of graphene's k-space for a separation of 1 eV [54]. Dashed line outlines graphene's 1st Brillouin Zone (BZ).

3.1.3 Graphene/hBN/gold tunnel junctions

Let us consider the tunneling junction depicted in Fig. 3.2a. Graphene is used as a top electrode and hBN acts as a tunneling barrier. The heterostructure sits on top of a gold electrode. The device is fabricated with a dry pick-up and transfer method (see Appendix A.1). A microscope image of the device is shown in Fig. 3.2b where the different flakes are outlined. By applying bias voltage V_b between gold and graphene, as illustrated in Fig. 3.2c, we create occupied states in gold and empty states in graphene in an energy range of eV_b.

However, bandstructure schematics, as the one in Fig. 3.2c, lacks information in momentum space (k-space). In reality transport in gold happens at the Γ point whereas graphene's Dirac point is at the K point. Considering again Eqs. 3.1 and 3.2, in order to be able to conserve momentum we need an interaction that can shift the electron from Γ to K point. Even considering the projection of gold's Fermi surface on the k-space of graphene, as illustrated in Fig. 3.2d, we see that the lack of overlap between them does not allow momentum conserving electron transitions [54]. However, in the work of Zhang et al. [55] transport from gold to graphene, in a scanning tunneling microscope (STM) junction, is observed where they reveal a phonon-induced inelastic tunneling mechanism. Such a process can allow coupling to optical modes since the phonon takes care of the momentum mismatch. The simplified bandstructure in Fig. 3.2c provides limited information on k-space. For that reason we expand it in three dimensions where we can accommodate also the k-space in one additional axis.

The resulting graph is shown in Fig. 3.3a. We call such a graph that shows spatial, spectral and bandstructure information, a bandagram in analogy to a spectrogram that shows temporal and spectral characteristics. Following the red arrow which shows the electron position in this three dimensional space we see that the electron moves to the Γ point of graphene (virtual state) where it interacts with a phonon. This interaction provides momentum that brings the electron to the K point of graphene and reduces the energy of the electron by $\hbar\Omega$. Provided available lower energy states in graphene, due to the applied bias V_b, the electron can decay radiatively releasing a photon of energy $\hbar\omega$. Rewriting Eqs. 3.1 and 3.2 leads to

$$E_i = E_f + \hbar\Omega + \hbar\omega \tag{3.8}$$

$$\mathbf{k}_i = \mathbf{k}_f + \mathbf{k}_\mathrm{phonon} \tag{3.9}$$

where we neglect photon momentum. For $eV_b < \hbar\Omega \simeq 65$ meV the electron has no available state to tunnel that leads to a dip in the conductance measurements shown in Fig. 3.3b. The other two dips observed are related to graphene doping and the minimum of graphene's DOS at the Dirac point [55, 56]. The graphene layer allows the emitted light of such a tunnel junction to be collected from the top. Emitted spectra for various V_b values are shown in Fig. 3.3c. As

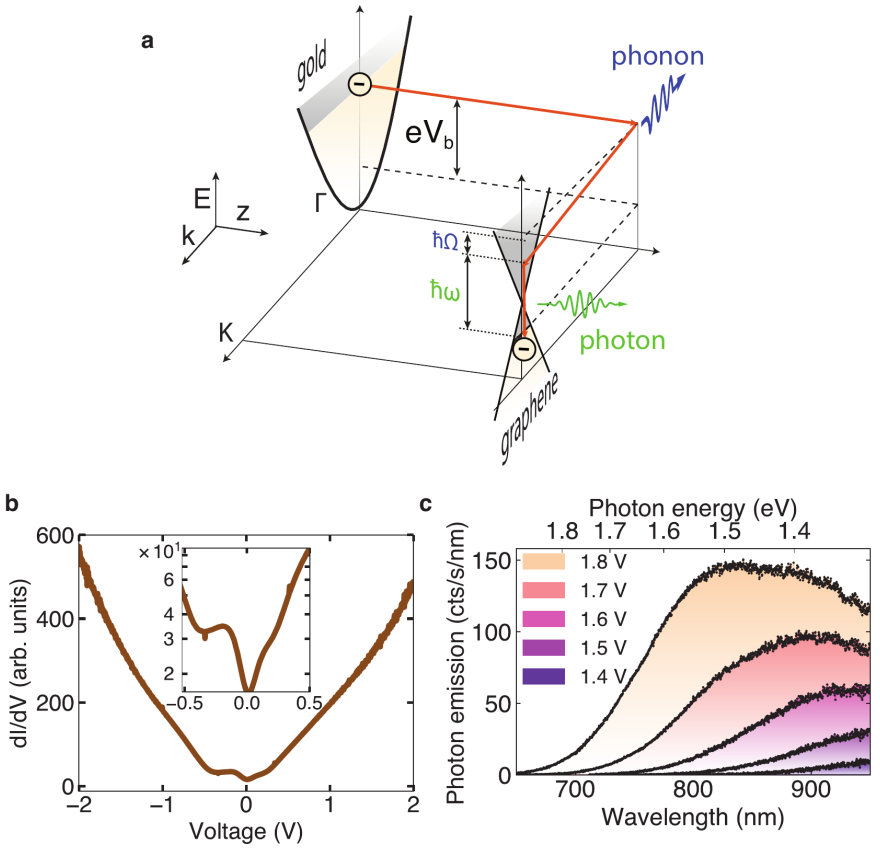

Figure 3.3: (a) A three-dimensional band diagram of a graphene/hBN/gold structure with momentum information (bandagram). The bandagram representation helps for a complete illustration of the phonon and photon interactions of tunneling electrons when transport happens in different k-space points. (b) Conductance (dI/dV) measurements of the device presented in Fig.3.2b. The inset shows the conductance curve in log-scale. The dip around 0 V is attributed to lack of tunneling below the phonon energy $\hbar\Omega \simeq 65$ meV. (c) Emission spectra in various V_b voltages. Inelastic tunneling occurs in the whole eV_b range leading to a broad spectrum of emission with an energy cut-off at eV_b.

described previously the electron can inelastically tunnel from any occupied state in gold in any empty state in graphene in the whole eV_b range. This leads to a broad spectrum of emission that presents a cut-off energy at eV_b. The real space image of emission presented in Fig. 3.4a reveals homogeneous emission through out the device area, demonstrating the advantage of using 2D materials which provide low thickness disorder and flat interfaces.

The transition dipole in tunnel junctions is parallel to the flow of electrons. In the vertical tunnel junction presented here this means an out-of-plane dipole orientation as illustrated in Fig. 3.4b. The angular radiation pattern of emission is revealed by imaging its Fourier space on a camera, as shown in Fig. 3.4c. A characteristic of out-of-plane emission is strong high angle emission and zero emission at the center. Although strong contribution of out-of-plane emission is observed, there is contribution by in-plane emission. This in-plane emission can originate from surface roughness and/or emission from the edges of the gold electrode as well as from chromatic aberration of the optical system due to the broad spectral emission. A big advantage of using graphene as an electrode is that the layer where the emission originates from (the hBN layer) is accesible up to nanometer distances making coupling of the tunnel junction with other components, such as optical antennas or other layered materials, easier. In

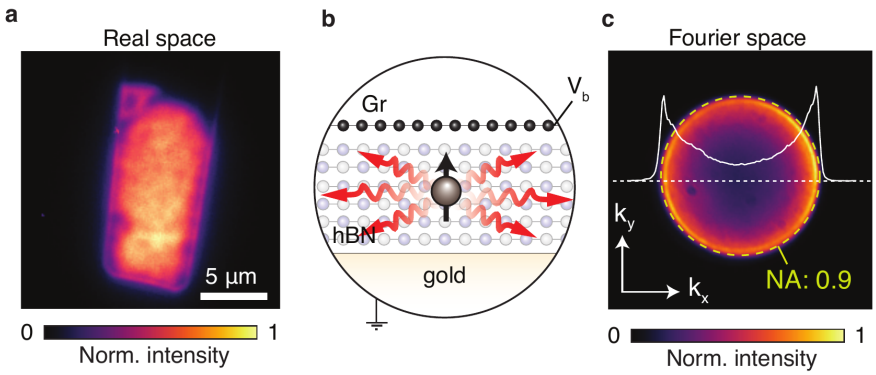

Figure 3.4: (a) Real space and (c) Fourier space image of emission of the device in Fig. 3.2b for V_b=2 V. The emission is homogeneous and presents contributions from out-of-plane dipole radiation, as expected in vertical transport tunnel junctions. (b) Schematic of the out-of-plane orientation of the dipole generated in the tunnel junction.

[56] such a structure is used as a basis for out-coupling radiation through cube antennas on metallic substrates. Moreover, inelastic tunneling emission exhibits ulrafast modulation capabilities to the GHz range [51] limited by the system capacitance. However, the light emission efficiency lies at the order of $10^{-9}/eV$ [56]. It has been shown that the use of optical antennas enhances the LDOS [51, 52, 56] leading to enhanced emission, however this emission is often localized and the maximum possible density of such sources is limited by the antenna size and design. On the other hand, light emission based on direct bandgap semiconductors relies on direct carrier injection and its efficiency is limited mainly by the quantum yield of radiative electron-hole recombination. In the next section we investigate electrically driven emission from TMD-based light emitting devices.

3.2 TMD-based light emitting devices

In contrast to tunnel junctions that rely on photon-assisted inelastic tunneling, TMD-based light emitting devices allow the use of direct carrier injection to generate light. Let us assume the device structure shown in Fig. 3.5a. The TMD is sandwiched between two electrodes (graphene and gold) from which the carriers are injected and is separated from the electrodes by hBN tunneling barriers which have double role. First, they allow electric field build up to separate the Fermi level of the two electrodes and second they reduce the probability of electron tunneling from the TMD to the electrode, increasing in that way the probability of radiative electron-hole recombination. A band diagram of such a double tunnel barrier light emitting device (DB-LED) is presented in Fig. 3.5b. The principle of operation is the following: Under applied bias $eV_b > E_{eg}$ electrons and holes are injected by tunneling to the CB and VB, while later relax to an excitonic state with binding energy E_b. The exciton generated can decay and emit a photon, owing to the direct bandgap of the monolayer TMD.

The TMD used in this study is $MoSe_2$ with an A-exciton energy of 1.55 eV and $E_{eg} \sim 1.8$ eV [57]. We first investigate the electroluminescence (EL) from a device driven at ± 2 V. A microscope image of the emission is shown in Fig. 3.5c, where the different flakes are outlined. The emission originates from the overlap of graphene, gold and $MoSe_2$. The EL intensity as a function of

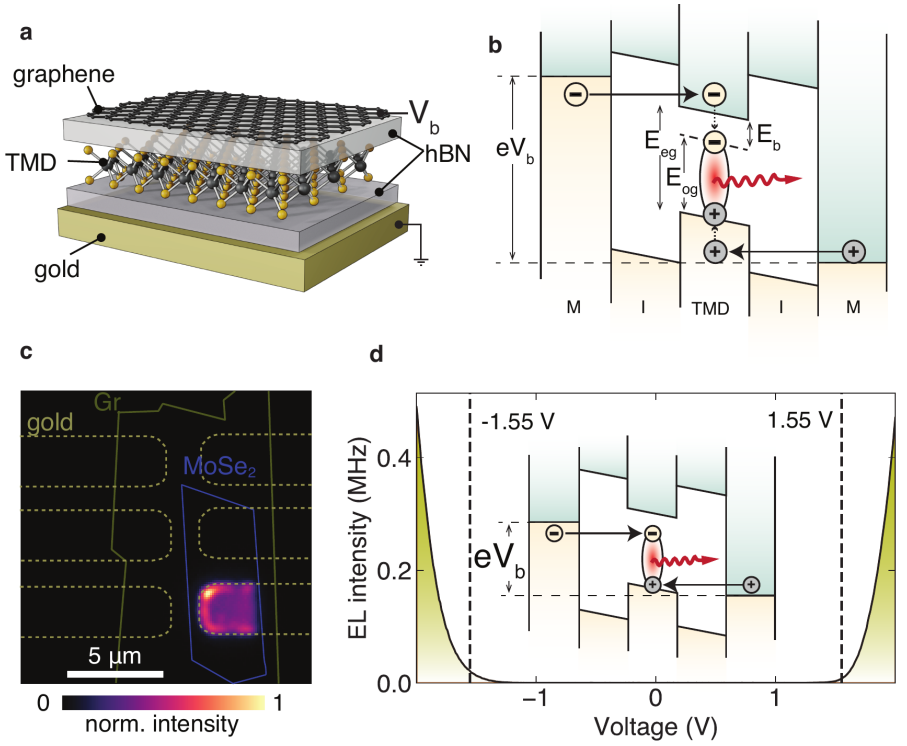

Figure 3.5: (a) A TMD-based double tunnel barrier light emitting device structure (DB-LED). (b) Band diagram of a DB-LED illustrating the charge injection mechanism that leads to exciton generation and subsequent light emission. (c) Microscope image of the electroluminesence (EL) emission from the overlap area of gold, graphene and $MoSe_2$ for $V_b = 2$ V. The tunnel barrier and the encapsulating hBN flakes are not outlined for clarity. (d) EL intensity as a function of V_b. The dashed lines at V_b= 1.55 V correspond to the exciton energy of $MoSe_2$. The inset illustrates in a band diagram the process of direct tunneling to the excitonic state without the need to populate both CB and VB.

voltage is shown in Fig. 3.5d. Interestingly, emission starts at $eV_b < E_{eg}$. In fact, the onset voltage corresponds to the optical bandgap of $MoSe_2$ (dashed lines in Fig. 3.5d), implying that electrons and holes directly form excitons upon tunneling at energies lower than E_{eg} [58, 59]. Such a process is illustrated in the inset of Fig. 3.5d.

The recorded spectra for $V_b = \pm$ 2 V are presented in Fig. 3.6a. Interestingly, the two spectra present differences. For V_b = 2 V the peak appears at λ= 815 nm (1.52 eV) implying a trion contribution to the luminescence whereas for V_b=-2 V the peak appears at λ= 795 nm that corresponds to the A-exciton. This surprising asymmetry can be explained by a potential intrinsic hole-doping of $MoSe_2$ and by taking into account the different DOS of the two electrodes. For $eV_b = +E_{og}$ gold's Fermi level aligns with the VB of $MoSe_2$ before graphene's Fermi level aligns with the CB (Fig. 3.6b). Gold populates strongly with holes the VB due to its high DOS. In that way, the electrons coming from graphene meet an excess of holes leading to a preferable positively charged trion formation (X^+). Investigating now the inverse case of $eV_b < -E_{og}$, as described in Fig. 3.6c, graphene's holes still populate the VB of $MoSe_2$ but not as strongly as gold, due to graphene's limited DOS. This leads to a preferable formation of A-excitons when V_b is negative. By looking at the emitted spectra as a function of voltage, as presented in Fig. 3.6d, we observe that for positive bias the emission slowly transforms from A-excitonic to trionic, demonstrating that with increasing hole population the formation of trions dominates the emitted spectrum. In negative voltages graphene provides DOS-limited holes and the few electrons that tunnel from gold inside the bandgap of $MoSe_2$ bind with them to form neutral excitons that contribute to the emission. Moreover, emission from the B-exciton with an energy of 1.7 eV starts being visible at higher voltages when the second spin-orbit split-band receives holes from gold. Effectively, such a device demonstrates an electrically controlled switch between trion and exciton emission by populating asymmetrically the VB. Three specific conditions apply for such an operation to be possible in a DB-LED: 1) The TMD needs to be p- or n-doped. 2) The DOS of the two electrodes needs to significantly differ. 3) The TMD needs to have higher DOS than one of the two electrodes. In this case, the electrode with lower than $MoSe_2$ DOS is graphene [60].

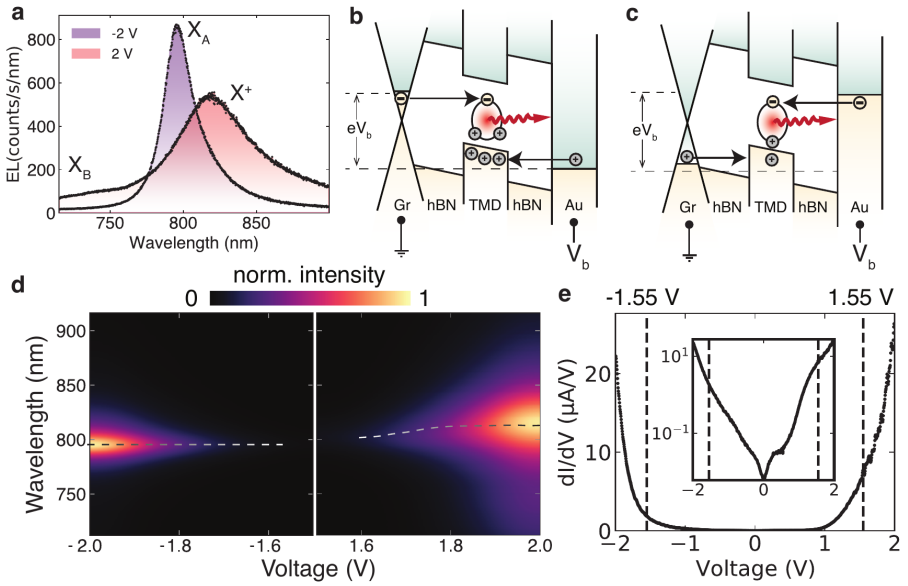

Figure 3.6: (a) Electroluminescence (EL) emission for both polarities. At V_b= 2 V mostly trions contribute to the emission. The spectrum appears broadened due to the overlap with the neutral A-exciton emission. At V_b= -2 V the emission originates mainly from neutral A-exciton decays. (b,c) Band diagrams describing the process of VB population and direct exciton creation for positive bias (b) and negative bias (c). Gold populates more strongly the TMD VB than graphene due to its high DOS leading to trionic emission. (d) EL spectra as a function of V_b. The dashed lines follow the peak value of the spectra in every voltage. The resolution of the spectral images was increased by bi-cubic interpolation. (e) dI/dV (conductance) curve with dashed lines indicating the corresponding V_b where eV_b matches the A-exciton energy. The inset shows the dI/dV curve in log-scale to show the gap-like feature measured due to phonon-assisted tunneling.

Finally, we study the conductance characteristics of the device as shown in Fig. 3.6e. First, the phonon-mediated tunneling signature is observed in low voltages (inset in Fig. 3.6e) as discussed for the case of Gr/hBN/gold tunnel junctions, implying that electrons tunnel from gold to graphene through the hBN and $MoSe_2$ bandgap. Moreover, the conductance for negative voltages, increase significantly after -1.55 V that corresponds to the exciton energy of $MoSe_2$ demonstrating that the excitonic state can assist tunneling by providing an intermediate state at the tunneling electrons. For positive voltages however

the conductance starts increasing already from V_b= 1 V. We attribute this early increase to the strong population of the VB from gold holes that facilitate an increased transport though the device.

3.3 Conclusions

In this chapter we studied two different types of light emitting devices made of van der Waals materials. First, we looked at Gr/hBN/gold heterostructures where light emission was observed by inelastic tunneling electrons coupling to photons. We discussed as well the particular case of the momentum mismatch between graphene and gold that is bridged by phonons of low energy, facilitating that way the transport in such structures. In the second part, we experimentally investigated a TMD based DB-LED. We observed emission below the electronic bandgap of the TMD and an asymmetric behavior in the spectrum of emission. Our observations can be understood as direct tunneling to excitonic states with strong hole population in the VB from gold. In our investigation we considered the electronic and excitonic states of the material. However, we should consider that the local density of optical states (LDOS) is enhanced by the presence of the TMD inside the DB-LED, making it possible in that way to enhance the inelastic tunneling rate and facilitate optical coupling between tunneling electrons and TMD excitons. In order to explore this potential effect and gain insight in the different available optical modes in such systems we theoretically study in the next chapter, the LDOS of a dipole in layered structures.

4

Density of optical states in 2D material systems

In the previous chapter we discussed how inelastic tunneling emission is affected by the optical density of states, as described by Eq. 3.5. Moreover, we also observed sub-electronic bandgap emission in TMD based-LEDs which can be understood as direct tunneling to excitonic states. However, contributions from tunneling electrons coupling optically to excitons cannot be excluded. To evaluate the role of LDOS in TMD-based light emitting devices it is instructive to study the coupling of a dipole source in 2D structures and investigate the various optical modes present in such interactions.

4.1 LDOS calculation in multilayer structures

Let us assume an electric point dipole situated inside a multilayer structure with out-of-plane orientation as illustrated in Fig. 4.1. The dipole inside the structure radiates. Due to the multiple transmitted and reflected fields at the interfaces of the structure, part of the radiation acts back to the dipole. The dipole's dissipated power P in this case is calculated by [36]

$$P = \frac{1}{2}\omega \, \mathrm{Im}\{\mathbf{p}^* \mathbf{E}(\mathbf{r_0})\} = \frac{1}{2}\omega \, \mathrm{p_z Im}\{E_z(\mathrm{r_0})\} \tag{4.1}$$

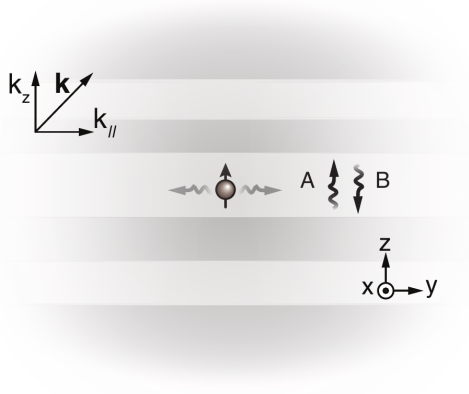

Figure 4.1: Illustration of a point electric dipole in a multilayer two-dimensional structure. The optical environment defines the available LDOS for the dipole to couple its electromagnetic energy. A and B are the amplitudes of the upward and downward propagating waves at the dipole's layer.

where ω is the angular frequency of the emission, $\mathbf{p} = p_z\,\hat{\mathbf{z}}$ is the dipole moment and $\mathbf{E}$ is the electric field at the dipole's origin $\mathbf{r}_0$. The electric field $\mathbf{E(r_0)}$ is calculated by solving the electromagnetic problem using the boundary conditions in every interface of the multilayer structure and is composed by a source field and an interaction field $\mathbf{E}(\mathbf{r_0}) = \mathbf{E}_S(\mathbf{r_0}) + \mathbf{E}_I(\mathbf{r_0})$. In a multilayer system with assumed infinity in x-y plane, the different optical modes are associated with specific in-plane wavevectors $\mathrm{k}_\parallel$ (see definition in Fig. 4.1). Hence, it is convenient to express $\mathbf{E(r_0)}$ in terms of its angular spectrum. By considering only the z-component of the field, which is relevant to the dissipated power of an out-of-plane dipole (see Eq. 4.1), the source field is written as [36]

$$E_{S,\mathrm{z}}(z) = \frac{i\omega^2 p_\mathrm{z}}{4\pi c^2 \epsilon_0 \epsilon_\mathrm{r}} \int_0^\infty \frac{k_\parallel^3}{k_\mathrm{z} k^2} e^{i k_\mathrm{z} |\mathrm{z}-\mathrm{z}_0|} d k_\parallel \tag{4.2}$$

where c is the speed of light in vacuum, ϵ_0 is the vacuum permittivity, ϵ_r is the relative permittivity of the medium where the dipole is situated, k is the absolute value of the wavevector $\mathbf{k}$ and along with its z-component k_z fulfill the relation $k^2 = k_\mathrm{z}^2 + {k_\parallel}^2$. The $\mathbf{E}_I(\mathbf{r_0})$ gives rise to fields with amplitudes A and B that propagate upwards and downwards in the system, as shown in Fig. 4.1. The optical density of states ρ_opt is then calculated through its relation to P as [36]

$$\frac{\rho_{\text{opt}}}{\rho_0} = \frac{P}{P_0} = \frac{3}{2} Re\left\{\int_0^\infty \frac{k_\parallel^3}{k_z k^2}(1 + A + B)\, dk_\parallel\right\} \tag{4.3}$$

where $\rho_0 = \pi^2\omega^2/c^3$ is the vacuum LDOS ands P_0 is the dissipated power for a point dipole in vacuum given by [36]

$$P_0 = \frac{\omega^4 p_z^2}{12\pi\epsilon_0 c^3} \tag{4.4}$$

For a detailed derivation of the LDOS in arbitrary complex 2D structures, please refer to Appendix A.2.

4.2 Dipole over a gold substrate

Let us use a simple example of a dipole near a metallic surface to illustrate the use of LDOS for analyzing layered systems. Figure 4.2a illustrates the system, where the dipole is situated in vacuum at a distance d away from a semi-infinitely thick and infinitely wide gold layer. The calculated LDOS for a photon energy $\hbar\omega$ =1.5 eV is shown in Fig. 4.2b where different optical modes are observed. The range $0 < k_\parallel/k_0 < 1$ corresponds to radiative modes in free

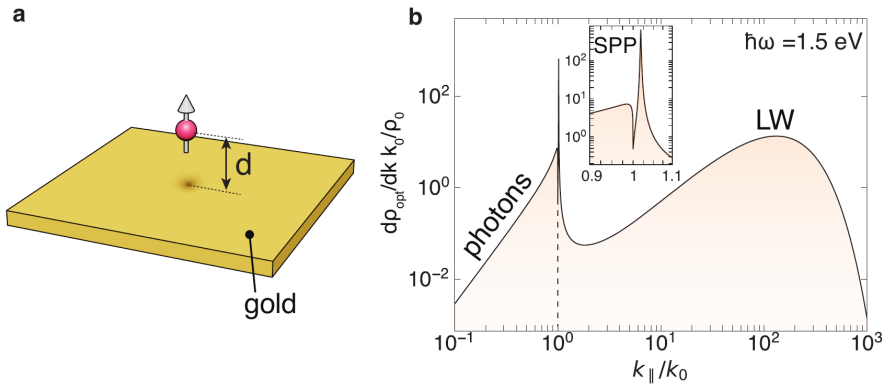

Figure 4.2: (a) An out-of-plane dipole situated at distance d from a gold substrate. (b) Angular spectrum representation of the LDOS for a dipole at d = 1 nm and for a photon energy $\hbar\omega$ = 1.5 eV. Three different optical modes can be distinguished. The inset shows a close-up of the region around $k_\parallel/k_0 = 1$ where the surface plasmon polariton (SPP) peak appears. Gold's optical properties taken from [61].

space (photons) and it qualitatively expresses the fact that an out-of-plane dipole emits mostly in-plane ($k_{\parallel}/k_0 = 1$). The narrow peak at slightly higher $k_{\parallel}$ values corresponds to the surface plasmon polariton (SPP) modes accessible at these photon energies. Finally, the biggest contribution to the LDOS comes from the third broad peak that corresponds to non-radiative and non-propagating lossy waves (LW) [50]. These modes are associated with the increased absorption close to lossy materials at nanometer distances. It is a near-field effect that can facilitate ET from a dipole to an absorptive material. The use of the term *"virtual photons"* has also been used in the context of ET, to describe the particle that is exchanged in this near-field interaction [62–64]. In this thesis we refer to the modes that facilitate ET as *non-radiative* or LW modes.

These three different optical modes (photons, SPPs and LWs) can be excited simultaneously. Photons by definition are radiative modes that can be detected in the far-field. For detecting any non-radiative modes we need to couple them to photons. SPPs propagate along the surface of the metal and coupling to photons is achieved by the use of gratings or optical antennas. LWs on the other hand do not propagate but decay fast inside the material, a process that is seen as quenching of the dipole when it is at the vicinity of a lossy material *. Figure 4.3a presents the dependence of the LDOS of every mode normalized by the total LDOS ($\rho_{\text{mode}}/\rho_{\text{opt}}$) as a function of distance d. Coupling to LW modes dominates the region below 10 nm, while it vanishes rapidly towards longer distances. Moreover, contributions to SPPs are higher compared to photons up to hundreds of nanometers.

Although the relative LDOS is useful for comparing contributions from different modes, the total LDOS is the one giving information on the total decay rate. Figure 4.3b shows the total LDOS as a function of distance. Below 10 nm, where LWs dominate, the LDOS is orders of magnitude higher compared to longer distances. The above highlights the significance of LWs in nanometer distances.

Finally, it is important to highlight that although the LDOS enhancement is usually used as a term for increased emission, in our case we discuss

*We remind the reader that quenching can also be caused by charge transfer, as discussed in Ch. 2, however the use of the term in the context of this thesis is mainly used for quenching due to ET.

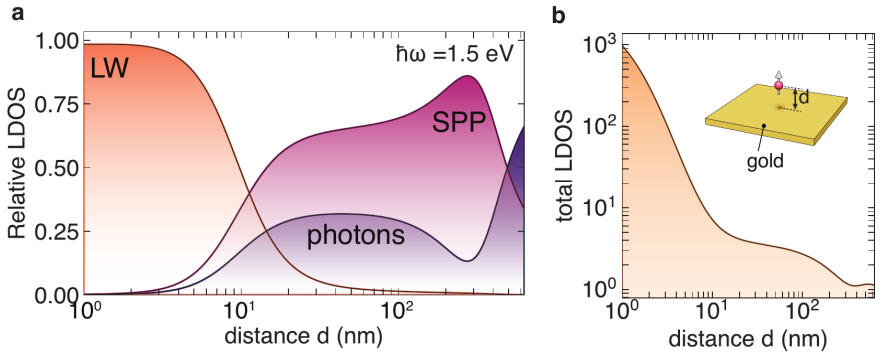

Figure 4.3: (a) Relative LDOS ($\rho_{\text{mode}}/\rho_{\text{opt}}$) of the different optical modes present at a gold-air system for $\hbar\omega$ = 1.5 eV. The LW modes dominate the LDOS below 10 nm. (b) Total LDOS a function of distance d as illustrated in the inset. The LDOS drops significantly above 10 nm highlighting that the LW contribution in these distances is order of magnitude higher than other optical modes.

enhancement that is associated to non-radiative modes and is not visible at the farfield. In fact, the lifetime of the emitter's excited state is shortened due to the increased non-radiative LDOS. In that way, the radiative emission rate is reduced (quenching) - a phenomenon that has been experimentally demonstrated as a function of distance in single molecule fluorescence systems in the proximity of gold nanoparticles [65].

4.3 Dipole over a TMD

In Ch. 3 we presented experimental results on light emitting devices based on TMDs where the possibility of near-field optical interactions as energy transfer was discussed. For gaining insight on that, let us assume the simple system of a dipole near a TMD monolayer. The optical properties of TMDs are dominantly defined by their excitonic resonances as shown in the absorption spectrum presented in Fig. 2.1. This spectrum was measured through optical excitation at the far-field [22]. However, the LW contribution, as presented in the previous section, spans to an angular spectrum range towards high momenta that is not accessible in optically excited electron transitions since these are limited close to $k_{\parallel} = 0$ as illustrated in Fig. 4.4a with purple. Electronic transitions of higher momenta lead to slightly different material optical response and since LW

contributions span to a broad angular spectral range it is important to include the momentum dependence in the calculations of LDOS.

Figure 4.4b shows the calculated LDOS angular spectrum for a dipole 1 nm above a MoS_2 monolayer as a function of energy. The exciton resonances lead to an increase of LDOS as it can be seen by the peaks that appear slightly above 2 eV. The two peaks correspond to the A- and B-exciton and they shift to higher energies with increasing $k_{\parallel}$ according to the curvature of the parabolic dispersion of the electron bands (see Fig. 4.4a). Moreover, it is again noticeable that the high-angle LW region dominates the angular spectrum in such distances. The peak-shifting effect due to the parabolic dispersion is noticeable in the total LDOS spectrum (Fig. 4.5a) where the various contributions of the exciton resonances overlap and the LDOS spectrum does not show distinct peaks rather a broadened enhancement above the exciton resonance (~ 2 eV).

The dependence of LDOS to distance d is presented in Fig. 4.5b where, as previously shown in the case of a dipole over a gold surface, the LDOS significantly drops after 10 nm revealing that the biggest contribution comes

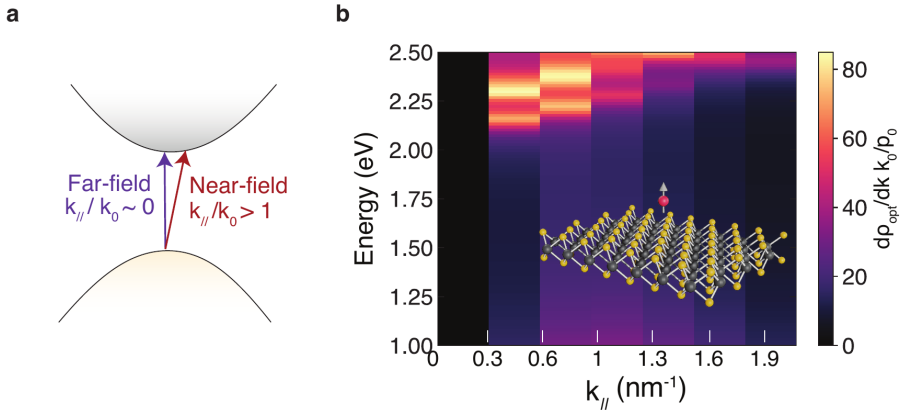

Figure 4.4: (a) Band diagram schematic of zero momentum (purple) and finite momentum (red) electronic transitions, associated with far-field and near-field interactions, respectively. (b) Angular spectrum representation of the LDOS for a dipole over a MoS_2 monolayer as a function of energy. Peaks appear above 2 eV due to the exciton resonances which shift to higher energies with increasing k (optical properties of MoS_2 provided by Fadil Iyikanat at ICFO, Barcelona, through first-principles calculations in the framework of many-body perturbation theory).

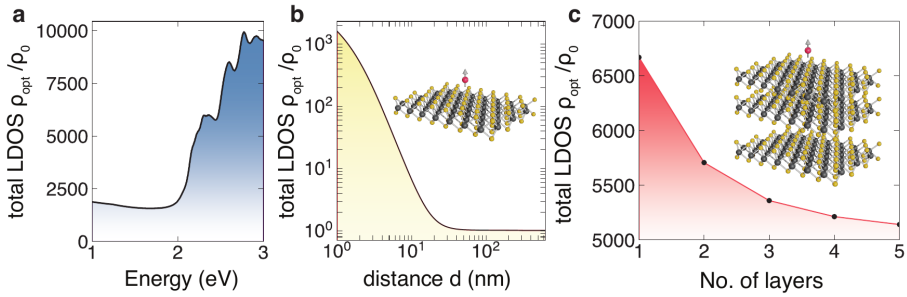

Figure 4.5: (a) Total LDOS spectra showing the increase of LDOS at energies above the A exciton resonance (2 eV) for a distance between dipole and TMD of d = 1 nm. (b) LDOS as a function of distance underlining the increase below 10 nm due to LW modes for a photon energy of $\hbar\omega = 2.5$ eV. (c) LDOS dependence on the thickness of the TMD for a distance d = 1 nm, using the assumption that the optical properties for different numbers of layers do not drastically change [66] for a photon energy of $\hbar\omega = 2.5$ eV

from LW modes that have a strong dependence to distance in few nanometers scale. Finally, we study the dependence of LDOS to the number of TMD layers. Due to lack of information on the angular spectrum of the optical properties of multilayer TMDs we complete the analysis at the basis of the assumption that the optical properties remain the same and only the thickness is changing. In fact, despite the transition of TMDs from direct to indirect bandgap semiconductors from monolayer to bilayer the optical properties do not differ significantly [66]. The result is shown in Fig. 4.5c. A non-intuitive effect is observed, the LDOS is dropping with the number of TMD layers. This can be explained qualitatively if we consider that in the monolayer case, the induced optical field distribution extents outside of the material more than in the multilayer case. This increases the interaction between the dipole and the optical modes of the material increasing the LDOS. With increasing TMD thickness this interaction decreases which causes the LDOS to drop. Indeed, in previous experimental studies, it has been observed that the decay rate of emitters close to TMDs decreases with thickness [67, 68].

4.4 Conclusions

In this chapter we discussed the different optical modes that are excited at layered structures when the emitter is situated at nanometric distances. We

found that the main contribution to the LDOS comes from LW modes commonly associated with emitter quenching. This study reveals the possibility to use these lossy channels in order to efficiently generate excitons by optically coupling to TMDs at nanometric distances through ET. In the next chapter we investigate such possibility by optically coupling TMDs to tunnel junctions.

5

Energy transfer from tunneling electrons to excitons

This chapter is based in part on the publication: S. Papadopoulos *, L. Wang *, T. Taniguchi, K. Watanabe and L. Novotny, *Energy transfer from tunneling electrons to excitons*, arXiv: 2209.11641 (2022). * These authors contributed equally.

In the previous chapter we analyzed the different optical modes that can be excited by a point dipole at layered structures. We revealed theoretically, in that way, the possibility of efficiently generating excitons in TMD-coupled LEDs in an unconventional way, by inelastic electron tunneling coupling to near field modes, that can contribute to the electrically driven luminescence. In this chapter we study this possibility experimentally and we present results that suggest strong coupling between tunneling electrons and TMD excitons.

5.1 Exciton generation in TMDs

In the past, exciton generation in optoelectronic devices has been studied through optical excitation [16, 19, 23–25, 69], external carrier injection [13, 58, 70–82], or employing pre-existing charges in the material [83]. Here we make use of atomically thin 2D materials and the flat interfaces between them

to preserve optical coupling in near-field distances between a TMD and a tunnel junction. To decouple charge injection effects, as presented in Ch. 3, the TMD is placed on top of a gold-hBN-graphene tunnel junction, i.e. outside of the tunneling pathway as shown in Fig. 5.1a. The emission spectrum presented in Fig. 5.1b features a distinct peak at the exciton energy of the TMD. We interpret this observation as exciton generation by energy transfer from tunneling electrons, which is further supported by a theoretical model based on inelastic electron tunneling.

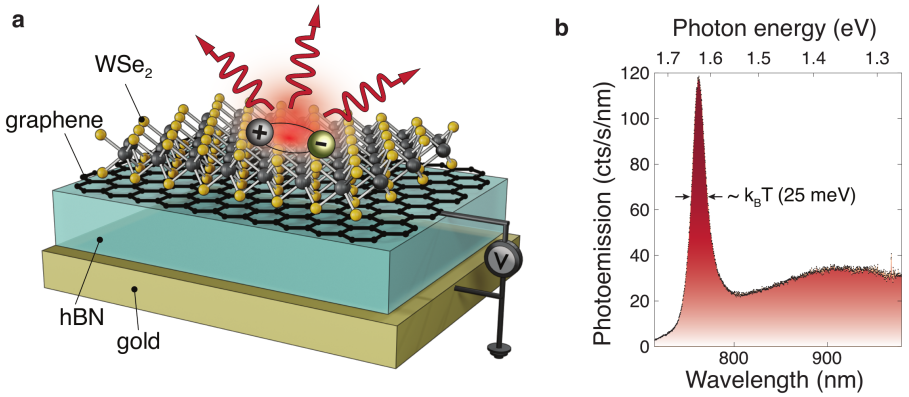

Figure 5.1: Exciton generation in TMD-coupled tunnel junctions. (a) Device composed of a WSe_2-coupled graphene-hexagonal boron nitride (hBN)-gold tunnel junction. The WSe_2 layer is stacked on top of the junction. When a bias voltage V_b is applied between graphene and gold, excitons are generated in WSe_2. (b) Measured spectrum at room temperature of the electrically generated emission for $V_b = 2\,V$. The peak position matches the WSe_2 exciton energy and the spectral width matches the thermal energy k_BT.

5.2 TMD-coupled tunnel junctions

The devices are fabricated by stacking mechanically exfoliated flakes of 2D materials with a dry pickup and transfer technique (see Appendix A.1). The resulting tunnel junctions consist of a graphene and a gold electrode separated by a 2.3 nm thick hBN acting as a tunneling barrier. The TMD is stacked on top of the junction and optionally separated from the graphene electrode by a second hBN layer.

Figure 5.2a shows a false-color microscope image of the device with an

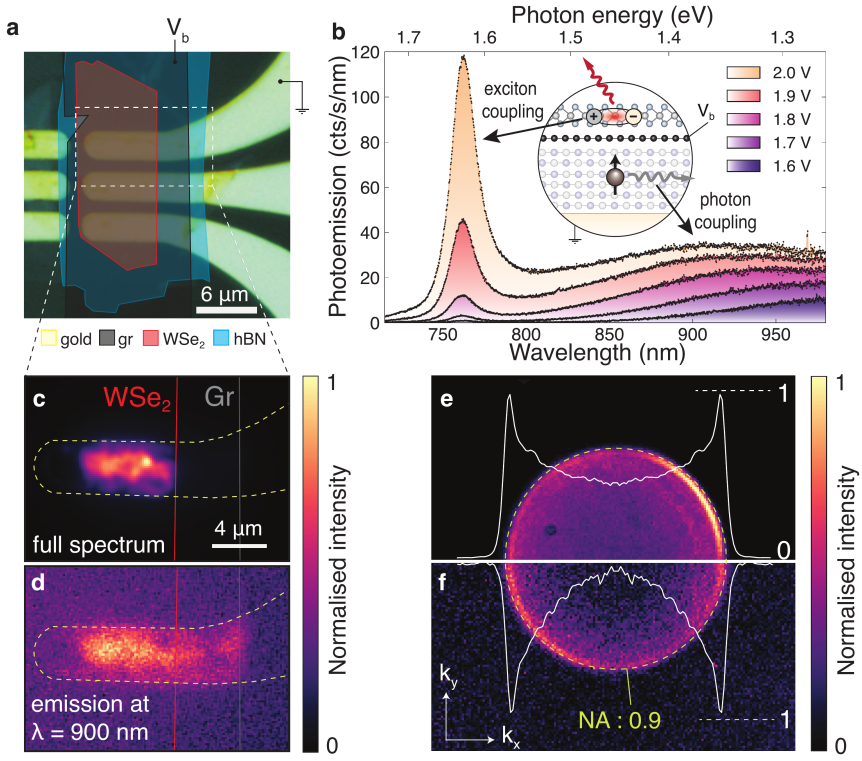

Figure 5.2: WSe_2-coupled tunnel junction. (a) Optical microscope image in false-color of a fabricated WSe_2-Graphene-hBN-gold device. The different flakes are outlined. The encapsulating hBN flake is not shown for clarity. The dashed frame indicates the device area depicted in (c) and (d). (b) Recorded emission spectra from the whole device area. Contributions from radiative mode coupling (*photon-coupling*) and non-radiative mode coupling (*exciton-coupling*) are observed. Real space (c,d) and Fourier space (e,f) images of the emission from the dashed box in (a) for $V_b = 2\,V$. The full emission spectrum is used in (c) and (e) whereas a bandpass filter with a center wavelength of 900 nm and 40 nm full-width-half-maximum (fwhm) is used in (d) and (f). Only half of every Fourier space is imaged for ease of comparison. The white solid lines are the rotational averages of the two Fourier spaces in (e) and (f).

outline of the different flakes. The device area is indicated by a white dashed box. The tunnel junction area is defined by the overlap of the gold electrode and the graphene flake. The WSe_2 flake is only partially covering the tunneling area. This creates two different tunneling regions, with and without WSe_2 on top. We electrically and optically characterize the device by applying a bias voltage (V_b) between the gold and graphene electrodes, as indicated in Fig. 5.2a, and we collect the emitted light with a high-numerical aperture objective (see Appendix A.3). The spectra emitted from the whole tunneling area for various V_b values are presented in Fig. 5.2b. There are two distinct contributions in the spectra. A broad emission at lower energies and a narrow emission peak at 1.63 eV (762 nm). The broad emission shifts to higher photon energies as V_b is increased. This behavior suggests that the emission originates from inelastic electron tunneling that couples to radiative modes of the free-space continuum (*photon-coupling*) with eV_b being the cut-off energy of emission as presented in Ch. 3 for a graphene/hBN/gold heterostructure. The narrow peak at 1.63 eV corresponds to the neutral 1s A-exciton of WSe_2 and its narrow width of around 25 meV can be attributed to graphene filtering as discussed in Ch. 2.

To further our understanding, we study the emission distribution for different spectral regions. Real space images of the photon emission are presented in Fig. 5.2c, where we observe that the area covered by WSe_2 dominates the emission and in Fig. 5.2d, where the emission is filtered by a bandpass filter at 900 nm. This is a spectral region where the excitonic contribution is much reduced and the emission extends over both device areas. This indicates that the broad low energy contribution indeed originates from *photon-coupling* and is not associated with the presence of WSe_2. To understand the angular emission of the device we record Fourier-space images. Fig. 5.2e shows the Fourier space image of the full emission spectrum whereas Fig. 5.2f depicts the Fourier space image of the bandpass filtered light around 900 nm. For the spectrally filtered measurement at 900 nm, the emission vanishes at the center of the Fourier space ($k_x = k_y = 0$) (Fig. 5.2f) indicative for an out-of-plane dipole orientation. This is characteristic of inelastic electron tunneling where the transition dipole is oriented along the electron path. On the other hand, when measuring the full spectrum, the Fourier space image (Fig. 5.2e) is not zero at $k_x = k_y = 0$, which indicates an in-plane contribution. This extra contribution is

associated with the excitonic emission of WSe_2, which is known to originate from in-plane transitions [84]. We emphasize that in our devices any exciton generation due to electron-hole injection is avoided due to the WSe_2 being outside of the tunneling pathway. This is further supported by the fact that very similar emission spectra are observed for negative V_b (see Appendix B). For these reasons we conclude that excitons are generated in the TMD by ET from tunneling electrons.

We continue to investigate this exciton generation process by considering the band diagram shown in Fig. 5.3a. Upon application of bias V_b, electrons tunnel from one electrode to the other, elastically or inelastically. In the latter case, the transition dipole associated with the energy loss ΔE couples to available optical modes of the environment. Some of these modes are radiative (photons) as in the case of the broad emission observed in Fig. 5.2b, or non-radiative, as in the case of ET. This ET mechanism generates excitons in WSe_2 and their spontaneous decay contributes to the narrow emission peak in the spectra of Fig. 5.2b. Thus, the excitonic emission observed in our device is a two step process, in which the transition energy is first transferred to the WSe_2 exciton and then spontaneously emitted (*exciton-coupling*). In Ch. 3 we discussed that tunneling from graphene to gold is facilitated by the interaction with phonons making in reality the exciton generation process described here a three step process. However, this discussion is omitted in this chapter by treating the tunneling process with no coupling to optical modes as quasi-elastic.

Next, we compare the ET efficiency to the *photon-coupling* efficiency. To do that we first break down the processes to the involved interactions (see pictorial representation in Fig. 5.3b) and we assign conversion efficiencies. Both *photon-* and *exciton-coupling* processes describe an electron-to-photon (e-γ) conversion. *Photon-coupling* is a first order process for which we define an e-γ conversion efficiency as $\eta_{e\text{-}\gamma}$. *Exciton-coupling* is a second order process in which we can assign a combined efficiency $\eta'_{e\text{-}\gamma} = \eta_{e\text{-}x} \cdot \eta_{x\text{-}\gamma}$, where $\eta_{e\text{-}x}$ is the ET efficiency and $\eta_{x\text{-}\gamma}$ is the exciton to photon conversion efficiency. From the spectra shown in Fig. 5.2b, we can infer a value of 4.3 for the ratio between the photon-coupled emission and the exciton-coupled emission. We calculate the ratio $\eta_{e\text{-}x}/\eta_{e\text{-}\gamma}$ using the following relationship,

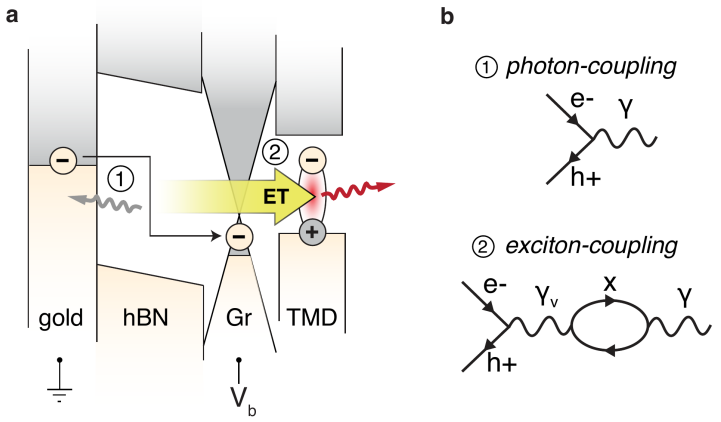

Figure 5.3: Photon and exciton coupling of inelastic tunneling electrons. (a) Band diagram of the TMD-coupled tunnel junction. A voltage V_b is applied across the hBN barrier between graphene and gold electrodes. Part of the electrons tunnel inelastically. They either couple to radiative modes (1) or couple non-radiatively to the TMD via ET (2). The generated excitons decay radiatively making the ET process detectable in the farfield. Band offsets not in scale. (b) Pictorial representation of the physical processes involved in the light emission. In (1) electron-hole recombination is followed by photon emission. In (2) ET is depicted as a virtual photon γ_ν that couples to the TMD and creates an electron-hole pair (x). The electron-phonon interaction that facilitates the tunneling between graphene and gold, as described in Ch. 3 is omitted in this description.

$$\frac{I_\mathrm{x}}{I_\gamma} = \frac{\eta_{\mathrm{e\text{-}x}} \cdot \eta_{\mathrm{x\text{-}\gamma}} \cdot \eta_\mathrm{col}^{\rightarrow}}{\eta_{\mathrm{e\text{-}\gamma}} \cdot \eta_\mathrm{col}^{\uparrow}} \tag{5.1}$$

where I_x is the exciton coupled emission, I_γ is the photon coupled emission, $\eta_\mathrm{col}^{\rightarrow}$ and $\eta_\mathrm{col}^{\uparrow}$ is the collection efficiency for an in-plane and an out-of-plane dipole, respectively. The $\eta_{\mathrm{x\text{-}\gamma}}$ expresses the PL efficiency of the WSe_2 flake which is measured to be around $1.5 \cdot 10^{-5}$. The low value results from graphene quenching [33]. We arrive at an estimation of the ratio $\frac{\eta_{e\text{-}x}}{\eta_{e\text{-}\gamma}} \cong 10^4$. This result indicates that ET is orders of magnitude more efficient than direct photon emission. In order to shed light on this surprising finding we analyze in the next section the density of optical states near a monolayer TMD.

5.3 Optical density of states near monolayer TMDs

In Ch. 4 we mentioned that when a dipole interacts with an absorbing material at a distance much smaller than the wavelength, the largest fraction of the dissipated power is associated with non-radiative energy transfer (ET) from the dipole to the material [50, 64]. The rate of this process is related to the local density of optical states (LDOS) ρ_{opt}. In Fig. 5.4 we show the calculated angular spectral density of the LDOS, $\frac{\mathrm{d}\rho_{\mathrm{opt}}}{\mathrm{d}k_{\parallel}}$, as a function of $k_{\parallel}$ for the simple case of a dipole at 2 nm distance from a TMD monolayer. Here, $k_{\parallel}$ is the wavevector component along the plane of the TMD monolayer (see inset in Fig. 5.4) and k_0 is the wavenumber for a photon energy equal to the exciton energy of WSe_2. The calculated ρ_{opt} for $k_{\parallel} < k_0$ includes radiative modes associated with photon emission (ρ_{r}) whereas the region $k_{\parallel} > k_0$ accounts for non-radiative modes (ρ_{nr}) associated with ET. ρ_{nr} is orders of magnitude higher than ρ_{r}. Moreover, the influence of the TMD on ρ_{r} enhancement is negligible. Hence, the TMD introduces mainly additional non-radiative decay channels that are associated with near-field ET ($\rho_{\mathrm{opt}} \cong \rho_{\mathrm{nr}}$), and is the reason for the

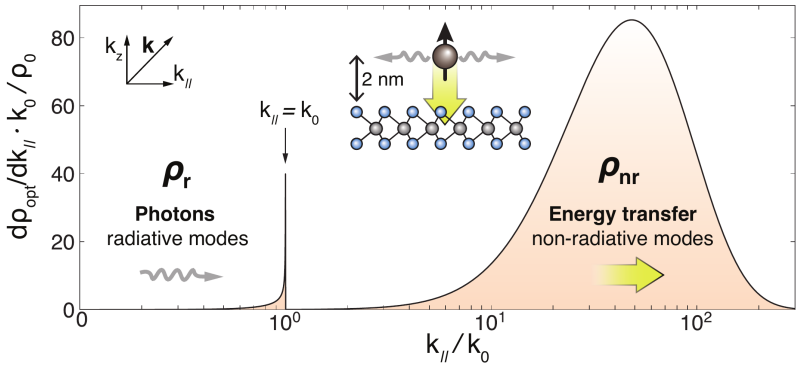

Figure 5.4: LDOS near a TMD. Angular spectral density of ρ_{opt} for the case of an out-of-plane dipole placed 2 nm away from a monolayer WSe_2. Optical properties are taken from [22]. The contribution of non-radiative modes (ρ_{nr}) is substantially higher than the contribution of radiative modes (ρ_{r}). The calculation assumes a photon energy of 1.68 eV, matching the exciton energy of [22]. The x-axis is normalized by the vacuum wavenumber k_0 and the y-axis is normalized by ρ_0/k_0, where ρ_0 is the vacuum LDOS. The inset illustrates the calculated system.

high $\frac{\eta_{\text{e-x}}}{\eta_{\text{e-}\gamma}}$ ratio. The ET process in our measurements is highly efficient and shows that near-field interactions at nanoscale distances are dominating the LDOS. Here, we probe this non-radiative interaction by using a direct-gap semiconductor whose luminescence is a direct measure for the ET efficiency. In essence, the TMD acts as a receiving optical antenna that enhances the LDOS and converts non-radiative modes to a measurable signal. We refer to this process as electron-photo-luminescence (ePL) since it is triggered by an electron that transfers energy through optical modes to WSe_2.

5.4 Dependence on TMD-Graphene separation

To further test our interpretation, we study the dependence of the excitonic emission on the distance between the TMD and the tunnel junction. A device schematic is shown in Fig. 5.5a where we vary the coupling to the TMD by changing the thickness d_{s} of a hBN spacer layer (s-hBN) in different device regions. Figure 5.5b shows the emitted light from a device where the s-hBN presents steps in thickness in the tunnel junction area. Four regions of emission are created. Three with different s-hBN thicknesses (6, 5 and 4 layers) and one without WSe_2 on top. We observe that the emission gets stronger the thinner the s-hBN is. As evidenced by the spectra shown in Fig. 5.5c the enhanced emission can be entirely attributed to the strength of the excitonic peak. We thus find that the excitonic contribution increases for thinner s-hBN in contrast to the broadband background that does not show any major change. A comparison of the excitonic emission intensity I_{x} for different d_{s} at $V_{\text{b}} = 2\,\text{V}$ is given in Fig. 5.5d. To be able to compare the rate of excitonic emission of different devices we normalize the measured emission intensity I_{x} by the area of emission and by the relative PL efficiency of the flake. Finally we normalize by the photon-coupled background emission I_{γ} in every device. This normalization is necessary because in every device the tunneling barrier thickness may vary by $\pm 0.33\,\text{nm}$. This has a minor effect on the optical coupling but it can drastically affect γ_{inel} through the momentum matrix element $\mathcal{P}$ (Eq. 3.6). This impacts the exciton generation rate Γ_{x} making the direct comparison between different devices difficult. However, since I_{γ} is directly proportional to $\mathcal{P}$ we use it to normalize the I_{x} emission and be able to compare devices with different TMD to tunnel junction distances (Fig. 5.5d). The data points in Fig. 5.5d

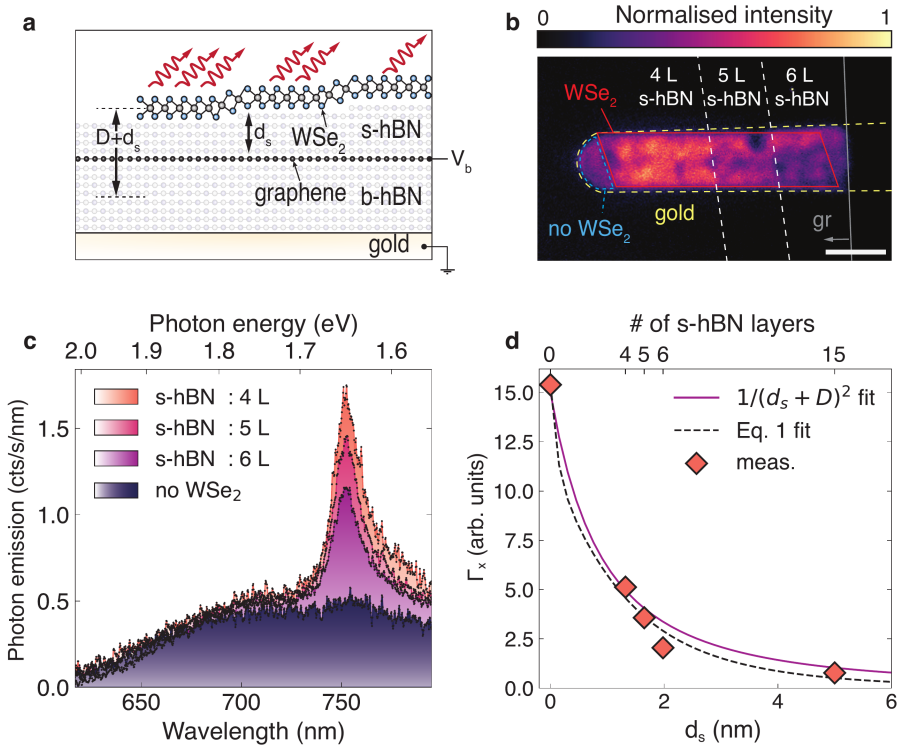

Figure 5.5: Energy transfer distance dependence. (a) Schematic of a TMD separated from the tunnel junction by a spacer-hBN (s-hBN). The coupling strength between TMD and the tunnel junction is varied using different s-hBN thicknesses d_s. (b) Real-space image of emission from the WSe_2/hBN/Gr/hBN/gold device. Strongest emission is observed from the thinnest s-hBN region. The emission is filtered with a bandpass filter (λ_{center} = 750 nm and fwhm = 40 nm). The scale bar is 4 µm. (c) Spectra measured on areas with different s-hBN thickness and for V_b = 2 V. The broad spectral background corresponds to direct photon coupling and is also observed in areas with no WSe_2. (d) Excitonic emission I_X as a function of d_s. The values are normalized with the PL efficiency, the emission area and the intensity of background emission. The measurement point at d_s = 0 nm refers to the device presented in Fig. 5.2. The three points between d_s = 1 nm and 2.5 nm refer to the device presented in Fig. 5.5b and the point at d_s = 5 nm refers to a third device that is presented in Appendix B. The dashed curve is the result of Eq. 5.2 for the material system illustrated in a. The dielectric functions for graphene, hBN and gold are taken from [61, 85, 86]. The solid curve is a fit with an inverse square distance function. $D + d_s$ is the distance between the TMD and the center of the b-hBN layer as illustrated in (a).

clearly show that the rate of exciton generation, and hence the ET rate, decay superlinearly with the separation d_s. I_x can be modeled by calculating the exciton generation rate Γ_x. By using inelastic tunneling theory [47] Γ_x assumes the following expression,

$$\Gamma_x(V_b, d_s) \propto \int_0^\infty \frac{\gamma^0_{inel}(\omega, V_b)}{\rho_0(\omega)} [\rho_{opt}(\omega, d_s) - \rho_{opt}(\omega, \infty)] d\omega \qquad (5.2)$$

where ω is the angular frequency, γ^0_{inel} is the inelastic tunneling spectral rate in vacuum and ρ_0 is the vacuum LDOS.

As shown pictorially in Fig. 5.6, in our model the exciton generation rate is defined by the overlap of the inelastic spectral rate in vacuum with the LDOS and the absorption spectrum. We approximate the LDOS responsible for exciton generation by $\rho_{opt}(\omega, d_s) - \rho_{opt}(\omega, \infty)$ which assumes that the states provided by the TMD, leading to exciton generation, vanish for $d_s \to \infty$.

The LDOS calculation process of multilayer structures is presented in Ch. 4. The calculated Γ_x as a function of distance d_s and for $V_b = 2\,V$ is plotted in Fig. 5.5d. It agrees well with the distance dependent measurement. Interestingly, both Γ_x and the measured data can be described by a simple inverse square law, as shown in Fig. 5.5d. Similar observations were reported for ET between optically excited TMDs [87]. There is good agreement between our theoretical model and our experimental measurements that supports further our interpretation.

5.5 Monolayer vs bilayer TMD

We continue our study by using a different TMD ($MoSe_2$) and by comparing ET for monolayers (1L) and bilayers (2L). Figure 5.7a shows a schematic of the device and the measured ePL spectra. The emission for 2L $MoSe_2$ (I^{ePL}_{2L}) is less intense than for 1L $MoSe_2$ (I^{ePL}_{1L}) owing to the indirect bandgap of 2L $MoSe_2$. To compare this ET-mediated photoluminescence (ePL) with optically excited photoluminescence (PL), we optically excite the two regions with a laser and measure the corresponding emission spectra I^{PL}_{1L} and I^{PL}_{2L}, respectively. The measurements are presented in Fig. 5.7b. The center wavelengths and the shapes of PL and ePL spectra match very well, which supports the interpretation that ePL corresponds to spontaneous exciton emission. We note however, that

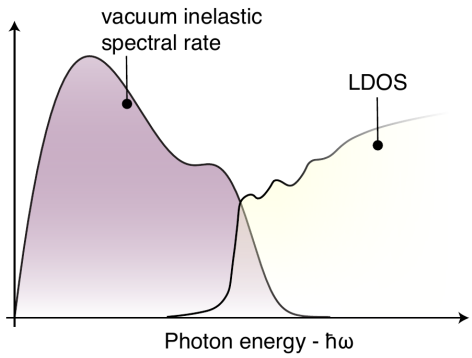

Figure 5.6: Spectral break-down of exciton generation rate Γ_x. Pictorial representation of Eq. 5.2 where the ovelap of the spectral components defines Γ_x.

the ratios I_{1L}^{PL}/I_{2L}^{PL} and $I_{1L}^{ePL}/I_{2L}^{ePL}$ are different. Interestingly, the $I_{1L}^{ePL}/I_{2L}^{ePL}$ ratio depends on V_b. In fact, I_{2L}^{ePL} is stronger than I_{1L}^{ePL} for low voltages and a crossing occurs near $V_b = 1.75\,V$, as shown in Fig. 5.7c, which depicts the integrated spectral intensity for different voltages. By employing the model in Eq. 5.2 we are able to reproduce this effect qualitatively. The result of this calculation is given in the inset of Fig. 5.7c. The reason for this voltage dependence are the different optical properties of 1L and 2L $MoSe_2$, i.e. the absorption spectrum of 2L MoSe2 features a cut-off energy at lower energies than the 1L $MoSe_2$. This explains the earlier onset-voltage for I_{2L}^{ePL} in Fig. 5.7c. Moreover, the two curves are also affected by the dependence of the LDOS on flake thickness. The rate of ET to a 2L TMD is lower compared to a 1L despite the fact that the 2L TMD is thicker, as discussed in Ch. 4.

5.6 Discussion

The exciton generation mechanism, discussed in this chapter, is an electromagnetic phenomenon that is usually neglected in the analysis of tunneling driven systems. The tunneling probability of an electron relies on the available electronic states but also optical states. In semiconducting materials, exciton resonances provide non-radiative optical states that couple strongly with inelastic electrons increasing the tunneling probability. This leads to near-field generation of excitons even for applied voltages below the electronic bandgap

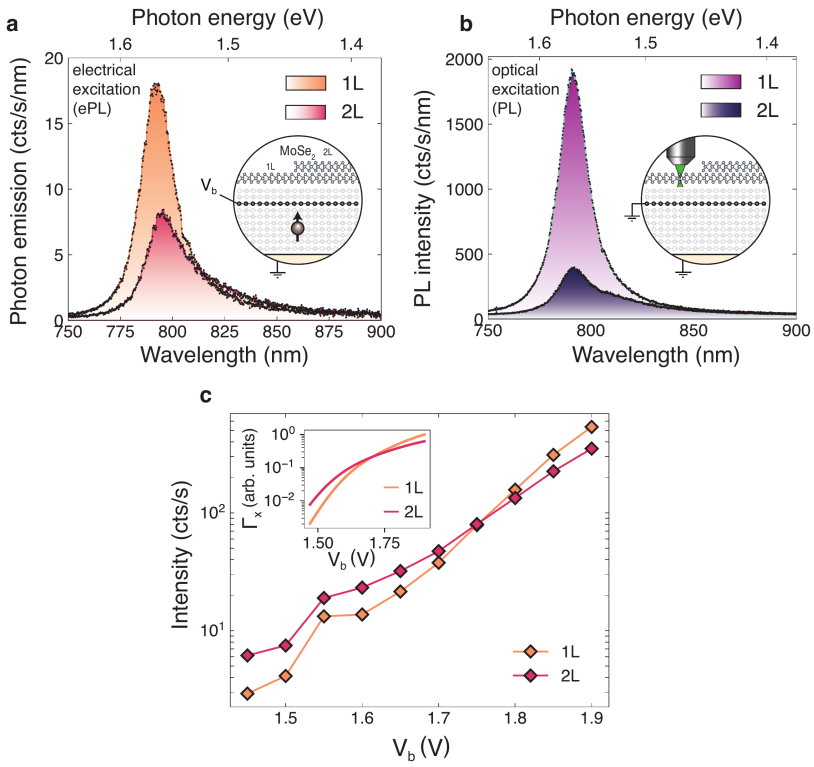

Figure 5.7: Tunnel junctions coupled to monolayer (1L) and bilayer (2L) $MoSe_2$. (a) ePL emission spectra from a device with 1L and 2L $MoSe_2$. Spectra taken at $V_b = 1.9\,V$. The inset shows the device schematic. (b) PL emission from 1L and 2L regions of the same device. (c) Integrated intensities of the ePL spectra in (a) as a function of V_b. The inset shows the corresponding theoretical curves based on Eq. 5.2.

of the material, thus contributing to sub-bandgap emission. Such low voltage emission has been previously studied with interpretations varying from direct exciton formation [58] to Auger scattering [79]. Here we show that ET from tunneling electrons can contribute to this sub-bandgap emission. Moreover, in terms of the efficiency of the process, in our measurements we observe electron-to-photon conversion efficiencies between $10^{-7}eV^{-1}$ and $10^{-6}eV^{-1}$ at excitonic energies. The main limitation comes from the low quantum yield of TMDs that is at the order of 10^{-4} in our devices. This value decreases even further due to gold and graphene quenching. A way to overcome this limitation

is by gating the structure and/or tuning the distance from the graphene electrode for optimized emission. More discussion on these possibilities is included in Ch. 8.

5.7 Dipole orientation

It is worth mentioning that the transition dipole orientation and the excitonic dipole are perpendicular to each other as illustrated in Fig. 5.8a. Such a disagreement in orientation decreases the coupling between them. In case the two dipoles are positioned on top of each other the coupling is zero. However, for slightly misaligned dipoles the coupling is not zero and is comparable to the optimum case where the two dipoles are parallel. To show that, we calculate the dipole orientation factor κ as [88]

$$\kappa = \hat{\boldsymbol{\mu}}_{\mathrm{t}} \cdot \hat{\boldsymbol{\mu}}_{\mathrm{ex}} - 3(\hat{\boldsymbol{\mu}}_{\mathrm{t}} \cdot \hat{\mathbf{r}})(\hat{\boldsymbol{\mu}}_{\mathrm{ex}} \cdot \hat{\mathbf{r}}) \tag{5.3}$$

where $\hat{\boldsymbol{\mu}}_{\mathrm{t}}$ and $\hat{\boldsymbol{\mu}}_{\mathrm{ex}}$ are the unit vectors of the tunneling electron and exciton dipoles, respectively and $\hat{\mathbf{r}}$ is the unit vector of vector $\mathbf{r}$ that connects the two dipoles (see Fig. 5.8b). For the coupling between two single dipoles (0D-0D) the rate of ET (k_{ET}) is proportional to κ^2/r^6. We calculate the normalized κ^2/r^6 quantity for different horizontal and vertical displacements between them (x,y) in Fig. 5.8b. We can see that around $x = 0$ nm the coupling is zero due to the fact that the two dipoles are on top of each other. However, for increasing distance x the k_{ET} increases since the radiation patterns of the two dipoles start overlapping. This increase in k_{ET} is comparable to the values achievable in the optimal case where the two dipoles are parallel as shown by the calculation in Fig. 5.8c. As an example, for $x = 0.15$ nm and $y = 0.5$ nm, the k_{ET} for the case of perpendicular dipoles (Fig. 5.8b) is only 30% weaker compared to the case of parallel dipoles for $x = 0$ nm and $y = 0.5$ nm (Fig. 5.8c). Of course, in the case of parallel dipoles a bigger part of the x, y parameter space shows increased k_{ET} making the parallel dipole configuration much more efficient. In practical terms though, a 2D vertical tunnel junction, as in our design, couples at a much bigger area to TMDs than in the case of a horizontal tunnel junction that necessarily has reduced dimensionality (OD or 1D) with that compensating for the lack of agreement in dipole orientation.

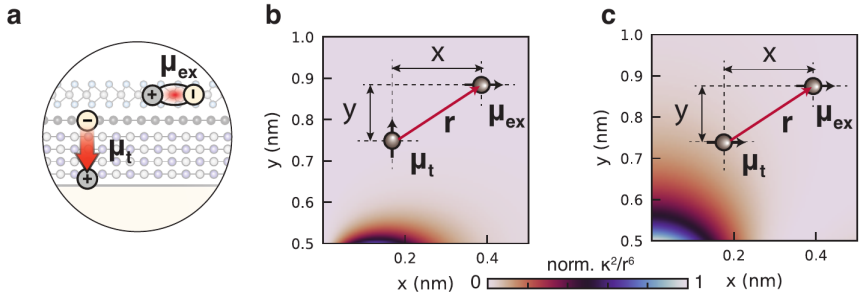

Figure 5.8: (a) The tunneling electron dipole and the excitonic dipole are perpendicular to each other. (b,c) Calculation of κ^2/r^6 (proportional to k_{ET}) for the case of (b) perpendicular and (c) parallel dipoles for different x and y values as presented in the inset of b and c. The colorbar is common between b and c.

5.8 Conclusions

We investigated ET from a tunnel junction to TMD excitons. Our studies are based on vdW tunnel devices in which the TMD is placed outside the electronic pathway, ensuring that there is no direct charge injection into the TMD. We studied emission spectra as well as real space and Fourier space emission patterns and we concluded that when the tunnel junction is under bias excitons are generated. This observation is understood by ET from tunneling electrons to excitons. Emission from excitons is observed even when the TMD is separated from the junction by a hBN spacer layer. Our calculations reveal that non-radiative modes of the LDOS are strongly increased at the exciton energy. These non-radiative modes are responsible for the efficient energy transfer from the tunnel junction to the TMD. Our theoretical model based on inelastic tunneling theory and near-field coupling is in agreement with our experimental results. Finally, we discuss that the lack of agreement in orientation between the tunneling electron dipole and the excitonic dipole reduces the coupling between them. However, this is compensated first by the interaction of horizontally misaligned dipoles which is still comparable to the case of parallel dipoles and second from the increased tunneling area of our vertical tunnel junctions as compared to horizontal ones.

6

Exciton-assisted electron tunneling

This chapter is based in part on the publication: L. Wang *, S. Papadopoulos *, F. Iyikanat *, J. Zhang, J. Huang, T. Taniguchi, K. Watanabe, M. Galame, M. L. Perrin, F. J. Garcia de Abajo and L. Novotny, *Exciton assisted electron tunneling in van der Waals heterostructures*, just accepted in Nature Materials (2023). * These authors contributed equally.

In the previous chapter we investigated light emission from tunnel junctions which were optically coupled to TMDs. We observed excitonic emission which we attributed to ET from tunneling electrons to excitons. The ET mechanism appeared to be orders of magnitude more efficient than direct coupling to radiative modes. We also showed theoretically that this increase in efficiency is related to LDOS enhancement that affects the inelastic electron tunneling rate Γ_{inel} (Eqs. 3.5 and 3.7) . As a consequence, an increase in the total current is expected. Although LDOS enhancement in optical antennas driven by tunneling has been observed optically in the past [51–53], the signature of Γ_{inel} in the current has not been yet observed. This happens due to the small size of the antennas compared to the overall tunnel junctions or due to elastic current masking the inelastic contribution. Moreover, in cases where the tunnel junction is the antenna itself [52] the electronic states are not sufficiently defined to allow discrimination between Γ_{el} and Γ_{inel}. Reference measurements without

the optical effects are not possible, in that case, since the tunnel junction is the optical antenna itself. In the case of TMD-coupled tunnel junctions as presented in this work, the TMD covers a big area of the overall tunnel junction and the 2D material platform allows us to design reference tunnel junctions without a TMD, on the same chip. In this chapter we present results on electron transport in TMD-coupled tunnel junctions where an increase in current is observed that can be associated with inelastic tunneling enhancement.

6.1 Transport measurements of TMD-coupled and uncoupled tunnel junctions

In this section we compare two tunnel junctions, one uncoupled and one TMD-coupled, as shown in Fig. 6.1a and b, respectively. The tunneling barrier of the two junctions is 2.3 nm thick hBN. We source the voltage and we measure the current for each. The I-V measurements are presented in Figs. 6.1c, d for the uncoupled and TMD-coupled device, respectively. The two curves look identical with a small scaling factor difference due to the different tunnel junction area. We look at the transport characteristics in more detail by calculating the current derivative (dI/dV). In that way we evaluate the conductance of the device as a function of V_{b} as shown in Figs. 6.1e, f. The gap-like effect of the phonon-assisted tunneling is observed in both devices for V_{b} around 0 V as described in section 3.1.3, indicating that the TMD does not affect the low voltage tunneling regime. A small increase in conductance is observed around V_{b}=-1.6 V, however the effect is not clearly discernible and evaluating higher voltages is not possible without damaging the device due to the breakdown voltage of hBN being around 1 V/nm [89]. Although the transport characteristics between the two devices do not present significant differences, we showed in Ch. 5 that efficient optical coupling occurs between tunneling electrons and TMDs that could lead to an increase in inelastic tunneling current. However, such an increase is challenging to spot due to excess of elastic tunneling current in our measurements*.

As a next step we study again uncoupled and coupled devices but with

*We remind the reader that references to elastic current in Gr/hBN/gold devices refer to quasi-elastic phonon-mediated current as discussed in Ch. 3.

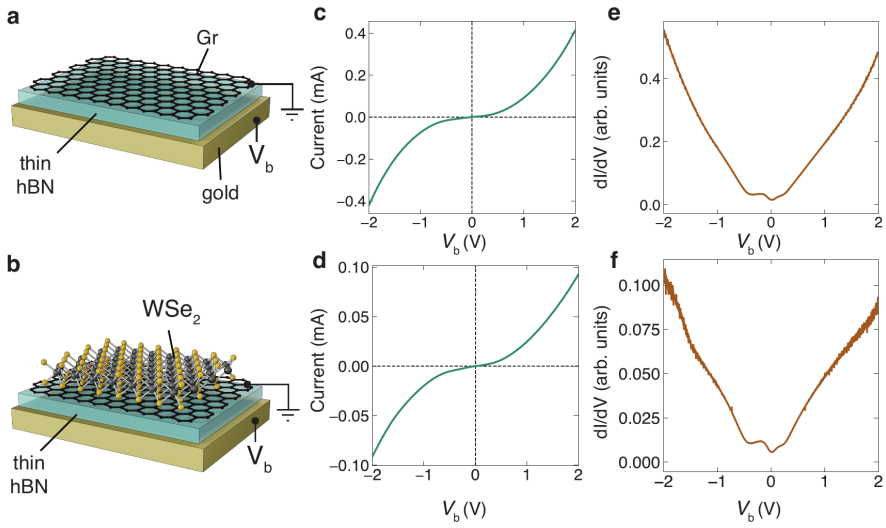

Figure 6.1: (a) A Gr/hBN/gold and (b) a WSe_2/Gr/hBN/gold tunnel junction, both with a thin hBN tunnel barrier of around 2.3 nm. (b) I-V and (c) dI/dV curve of a Gr/hBN/gold device. (e) I-V and (f) dI/dV curve of a WSe_2/Gr/hBN/gold device.

a thicker hBN layer as tunneling barrier. We fabricate two tunnel junctions without and with WSe_2 (see Fig. 6.2a, b) and with a thick hBN barrier of around 3-4 nm. We measure the current while sourcing the voltage in both. The I-V curves are presented in Figs. 6.2c, d. We first observe that the current has dropped around 5-6 orders of magnitude compared to the devices presented in Fig. 6.1 due to the exponential decrease of the total current with the barrier thickness. Moreover, the curve becomes more asymmetric. We attribute this increase to gold's DOS increase at negative voltages [56]. The two I-V curves do not differ substantially. We move on by comparing the respective conductance curves presented in Figs. 6.2e, f. Remarkably, we observe a clear difference between the two curves. In contrast to the reference device, however, we now observe a pronounced resonance peak at ~1.69 V. The energy of 1.69 eV matches well that of excitonic excitations in monolayer WS_2 [90, 91], which provides strong support in favor of the exciton-assisted tunneling mechanism.

The WSe_2-coupled device presents a peak around V_b=1.69 V which can be attributed to the 1s A-exciton with energy 1.65 eV. The small shift in energy is

possibly related to the background conductance slope. Such a feature does not appear at the conductance curve of the uncoupled device. This lets us conclude that the observed peak is related to the WSe_2 A-exciton and since the TMD is situated outside of the tunneling pathway lets us interpret such a signature as exciton-assisted tunneling by ET from electrons to excitons.

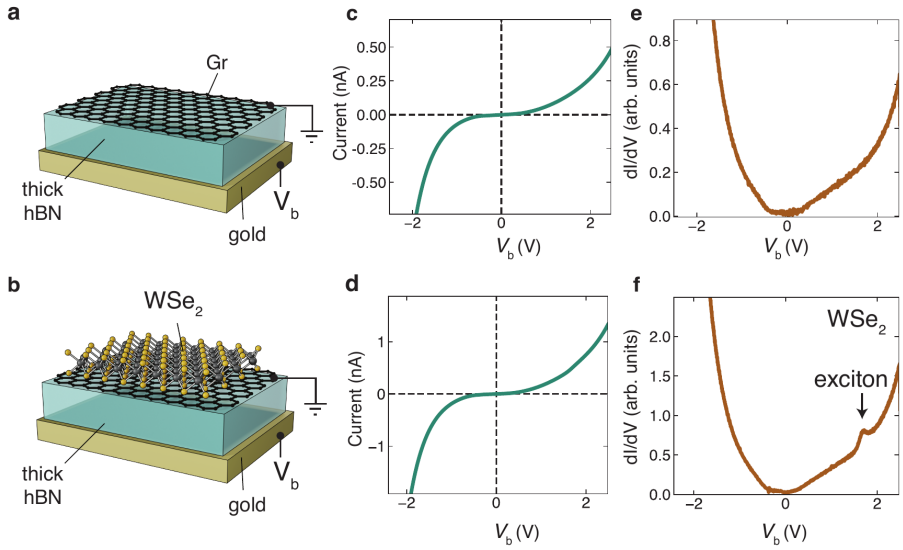

Figure 6.2: A Gr/hBN/gold and (b) a WSe_2/Gr/hBN/gold tunnel junction, both with a thick hBN tunnel barrier of around 3-4 nm. (b) I-V and (c) dI/dV curve of a Gr/hBN/gold device. (e) I-V and (f) dI/dV curve of a WSe_2/Gr/hBN/gold device.

In order to provide further evidence of the excitonic nature of the peak appearing in the conductance curve in Fig. 6.2f we expand our study by looking at different TMD devices, measured at various temperatures down to 10 K. The results for WS_2, WSe_2, MoS_2 and $MoSe_2$ devices are shown in Fig. 6.3.

In all four devices we observe the same temperature trend: the peaks become sharper due to the decreased thermal broadening and shift towards higher energies. For the WS_2 device, we observe a shift in peak position to larger bias voltages, from ~2.05 V (290 K) to ~2.07 V (10 K), consistent with the temperature-dependent measurements of excitonic resonances in WS_2 [92, 93]. Upon closer inspection, we find another resonance near 2.26 V, which becomes visible at low temperatures for the WS_2 device (Fig. 6.3a) suggesting coupling

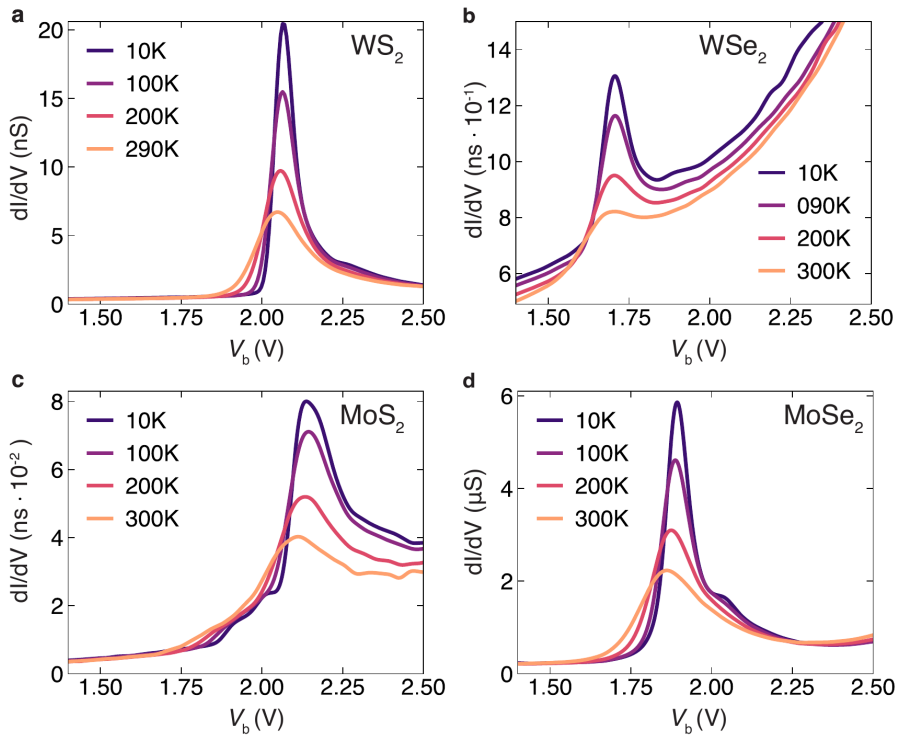

Figure 6.3: Temperature dependent differential conductance (dI/dV) measurements for (a) WS_2, (b) MoS_2, (c) WSe_2 and (d) $MoSe_2$ devices. The devices presented in this figure were fabricated by Lujun Wang with support from Jing Huang and Sotirios Papadopoulos and measured by Jian Zhang in EMPA, Dübendorf.

to excitons of higher energy. Measurements for a MoS_2 device are plotted in Fig. 6.3b, where a main peak at $V_b = 2.1\,V$ is observed, exhibiting a similar temperature dependence as the WS_2 device. A weak feature appears at slightly lower V_b and develops into two distinct shoulders at lower temperatures, one at ~1.92 V and another one at ~2.02 V. The irregular features at bias voltages beyond 2.2 V, especially at high temperatures, are attributed to measurement instabilities. For the WSe_2 device shown in Fig. 6.3c, we observe a main resonance at $V_b = 1.69\,V$ and the temperature dependence is similar to the previous two devices. The wiggles appearing at higher bias voltages are assigned to measurement instabilities. The $MoSe_2$ device plotted in Fig. 6.3d

presents the same temperature behaviour. The resonance in this case appears at $V_b = 1.9\,V$. The smaller feature at ~2.04 V, which becomes more pronounced at low temperatures, is likely arising from higher energy excitons. The resonances appear at different bias voltages for every TMD, an observation that hints to exciton coupling.

By using PL spectroscopy, as described in Ch. 2, we can measure the energies for the TMD direct excitons in our devices. Table 6.1 presents the measured A and B exciton energies (E_{X_A}, E_{X_B}) as compared to the bias voltage in which the dI/dV peaks appear for all studied TMDs (column 2 and 3). The two energy values do not agree. The difference in energy between the two (eV_{peak}-E_{X_A}) is calculated in column 4 of Table 6.1. All dI/dV peaks appear at higher energies than the corresponding A excitons. It appears that the interaction that manifests itself through the increased current, is not in agreement with direct exciton transitions.

In Ch. 3 we introduced a Gr/hBN/gold light emitting tunnel junction where we discussed that the tunneling between graphene and gold is facilitated with an electron-phonon interaction that bridges the momentum mismatch between the K-point and Γ-point. Following this interaction an electron can decay into a photon through a direct transition. In Ch. 5 we introduced the concept of such a decaying electron coupling to direct excitons that can radiatively decay, as described also by the bandagram presented in Fig. 6.4a. The lack of agreement however between the dI/dV peak energy values and the direct exciton energies measured through PL spectroscopy leads us to investigate other

material	E_{X_A}, E_{X_B} PL (eV)	dI/dV peak (eV)	eV_{peak}-E_{X_A} (meV)	ΔE_{KQ} spectroscopy [94, 95] (meV)	ΔE_{KQ} $\mathbf{k}\cdot\mathbf{p}$ theory [96] (meV)
WS_2	1.98, -	2.07	90	120	58
MoS_2	1.87, 2.0	2.1	230	150	256
WSe_2	1.64, -	1.675	35	-150 / -80	32
$MoSe_2$	1.57, 1.72	1.9	330	130 / 190	163

Table 6.1

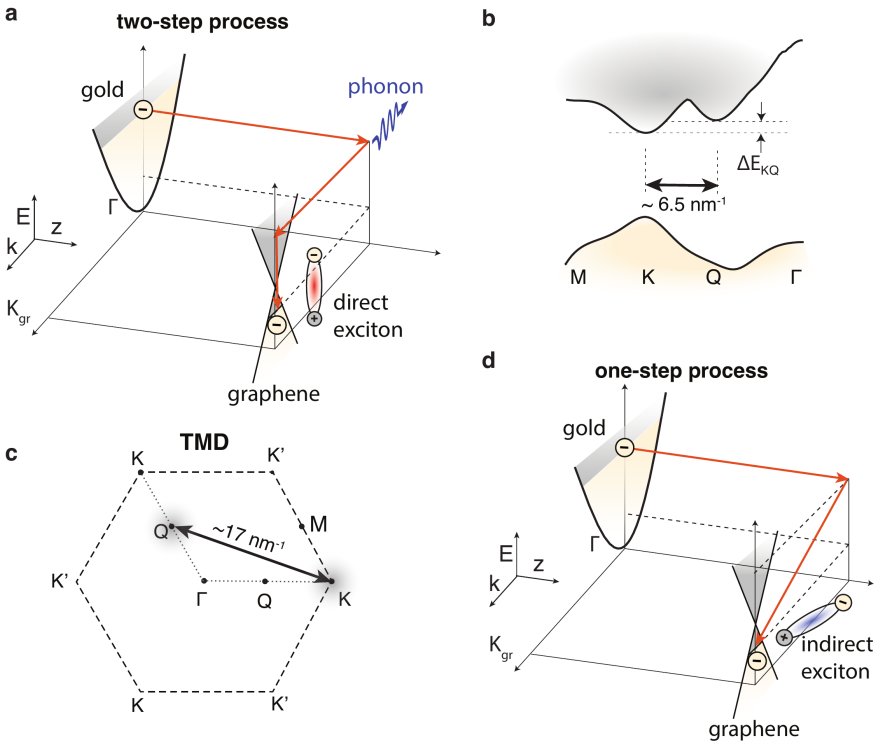

Figure 6.4: (a) Bandagram of a two-step tunneling process where the momentum is conserved by an interaction with a phonon and the energy is conserved by creating a direct exciton. The phonon energy is much smaller than the exciton energy thus it is neglected from the picture for simplicity. (b) Band structure of a TMD including the K-point and Q-point. (c) TMD 1st BZ. The distance between some of the K-Q combinations (black-arrow) in momentum space has values around $17nm^{-1}$ coinciding with the momentum mismatch between graphene and gold. The precise K-Q momentum difference for various TMDs is WS_2: $17.65nm^{-1}$, MoS_2: $17.28nm^{-1}$, WSe_2: $17.05nm^{-1}$ and $MoSe_2$: $16.92nm^{-1}$. (d) Bandagram of the proposed one-step tunneling process in which both momentum and energy is conserved by the creation of an indirect exciton.

possible mechanisms.

Indirect excitons formed between neighboring K-points and Q-points have slightly different energies than the direct ones. However, as far as momentum conservation is taken into account, for neighboring K-points and Q-points, as illustrated in Fig. 6.4b, indirect excitons cannot provide the necessary momentum (~6.5 nm^{-1}). However, by investigating the 1st BZ of the TMD (Fig. 6.4c) we find that there are combinations of K-points and Q-points (marked with a double black arrow) that provide coincidentally a momentum value around the missing momentum of 17 nm^{-1}. This enables us to imagine a one-step process, as presented in the bandgram of Fig. 6.4d, where energy and momentum conservation are both fulfilled by a single indirect exciton. Reported measured and calculated values of the ΔE_{KQ} quantity (Fig. 6.4b) are given in column 5 and 6 in Table 6.1. These values appear to be close to our measured eV$_{peak}$-E$_{X_A}$ values. Especially in comparison with the $\mathbf{k}\cdot\mathbf{p}$ theory results the values agree to a great extent. The agreement is not as high for the measured values of ΔE_{KQ} however any discrepancy of this kind might be coming from the fact that the exciton binding energies are not taken into account in the measurement of electron energies between K and Q bands [94, 95]. The aforementioned allows us to interpret the observed dI/dV peaks as an increase of inelastic tunneling current due to coupling to excitonic species in a one-step process where K-Q indirect excitons contribute to the overall momentum and bridge the gap between gold and graphene. However, a two-step process at which the excitonic species do not carry sufficient momentum (direct excitons) and the momentum is provided by phonons is still possible since the excitonic light emission observed in these devices and presented in Ch. 5 suggest creation of direct excitons.

6.2 Tunneling barrier thickness dependence

Towards understanding the reason for which the conductance peaks are only discernible in devices with 3-4 nm hBN barrier, it is instructive to study the relation between Γ_{el} and γ_{inel} in a simplified model. Let us consider an MIM tunneling system as described by its band diagram in Fig. 6.5a, similar to the one presented in Ch. 3.

To form an intuitive analytical model we proceed to some simplifications.

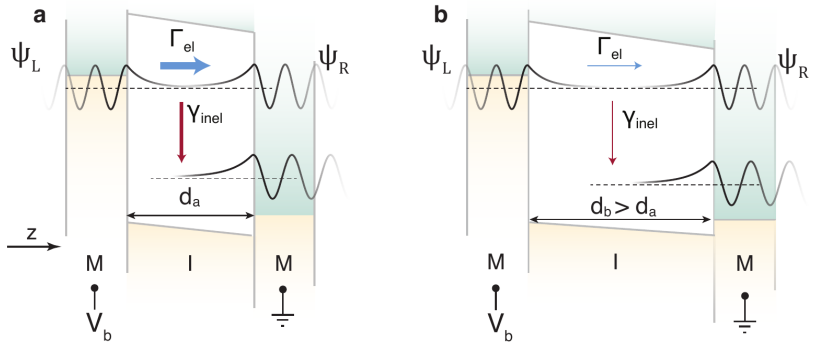

Figure 6.5: (a) Band diagrams of a metal-insulator-metal (MIM) tunnel junction under bias where electron can tunnel either elastically or inelastically with rate Γ_{el} and spectral rate density γ_{inel}, respectively, for a tunnel barrier thickness d_a. (b) When the barrier thickness increases ($d_b > d_a$) both rates drop but the ratio $\gamma_{\text{inel}}/\Gamma_{\text{el}}$ increases.

First, we assume that the insulator barrier potential is high enough to be approximated as flat and that the two electrodes are only weakly coupled meaning that the insulator thickness is assumed infinite for the description of the wavefunctions on the left and right electrodes. This allows us to write the wavefunctions of the states ψ_{R} and ψ_{L}, inside the tunneling barrier, as single decaying exponential functions [97],

$$\psi_{\text{L}} = \psi_{\text{L},0} e^{-\kappa z} \tag{6.1}$$

$$\psi_{\text{R}} = \psi_{\text{R},0} e^{-\kappa(\text{d}-\text{z})} \tag{6.2}$$

where $\psi_{\text{R},0}$ and $\psi_{\text{L},0}$ are the amplitudes ψ_{R} and ψ_{L} wavefunctions, respectively and κ is the decay constant of the wave function inside the tunneling barrier. This allows us to write the transfer and momentum matrix elements through Eqs. 3.4 and 3.6 as [97]

$$\mathcal{T} = \frac{\hbar^2 \kappa}{m} \psi_{\text{L},0} \psi_{\text{R},0} e^{-\kappa \text{d}} \tag{6.3}$$

$$\mathcal{P} = -i\hbar\kappa d \psi_{\text{L},0} \psi_{\text{R},0} e^{-\kappa \text{d}} \tag{6.4}$$

Finally, by further assuming that the decay factor and amplitudes of states, as well as the electronic density of states, do not change significantly within the range of energies provided by the eV_b separation we use Eqs. 3.3 and 3.5 to calculate Γ_{el} and γ_{inel} as

$$\Gamma_{el} = 2\pi\hbar^3\kappa^2\psi_{L,0}^2\psi_{R,0}^2 e^{-2\kappa d}\rho_L\rho_R eV_b \tag{6.5}$$

$$\gamma_{inel} = \frac{\pi e^2\hbar^2\kappa^2 d^2}{3m^2\epsilon_0}\psi_{L,0}^2\psi_{R,0}^2 e^{-2\kappa d}\rho_L\rho_R\frac{\rho_{opt}(\hbar\omega)}{\hbar\omega}(eV_b - \hbar\omega) \tag{6.6}$$

The ratio between the two rates is then given by

$$\frac{\gamma_{inel}}{\Gamma_{el}} = \frac{ed^2}{6m^2\epsilon_0\hbar V_b}\frac{\rho_{opt}(\hbar\omega)}{\hbar\omega}(eV_b - \hbar\omega) \tag{6.7}$$

As expected this spectral ratio depends linearly on the LDOS. Most interestingly though, it presents a quadratic dependence to distance d which is the separation of the two electrodes. Both Γ_{el} and γ_{inel} components drop exponentially with distance, due to the exponential decay of the wavefunctions in the barrier, as illustrated in Fig.6.5a, b. However, as Eq. 6.7 suggests, $\gamma_{inel} \propto d^2\ \Gamma_{el}$ which means that by increasing the tunneling distance, current signatures of inelastic processes increase compared to elastic ones. This relation fits qualitatively with our observation that devices with thicker barriers exhibit a measurable contribution of inelastic tunneling due to exciton coupling.

6.3 Conclusions

In this chapter we explored the transport characteristics of TMD-coupled tunnel junctions. We performed a comparison between TMD-coupled and uncoupled devices and we observed that for the cases where the tunneling barrier is thick enough (around 3-4 nm) resonant peaks appear in the conductance curves. These peaks appear in energies that do not exactly match the direct exciton energies of the corresponding TMD which leads us to investigate other excitonic species. We find that there are indirect excitons with reported energies closer to the ones observed in the dI/dV peaks. In addition, these excitons formed between the

K-point and a Q-point from another K-point neighborhood can carry enough momentum to bridge the momentum gap between graphene and gold. This makes electron tunneling a one-step process rendering it surprisingly efficient as it is suggested by the strong peaks at the dI/dV curves. However, this increase in efficiency does not lead to high emission efficiency due to the generation of mostly indirect excitons. Summing up, we interpret the dI/dV peaks as exciton-assisted inelastic electron tunneling due to optical coupling between electrons and excitons demonstrating in that way an all-electrical measurement of optical properties of TMD monolayers. Indirect excitons appear as possible candidates since they match the momentum difference between graphene and gold tunneling electrons. However, the excitonic light emission observed suggests additionally the existence of a two-step process at which the excitonic species do not carry sufficient momentum (direct excitons) and the momentum is provided by phonons.

7

Ion migration in monolayer MoS_2 memristors

This chapter is based on the publication: S. Papadopoulos, T. Agarwal, A. Jain, T. Taniguchi, K. Watanabe, M. Luisier, A. Emboras and L. Novotny, *Ion Migration in Monolayer MoS_2 Memristors*, Phys. Rev. Applied 18, 01401 (2022).

In this chapter we shift our attention to an alternative application of 2D heterostructures namely the realisation of TMD-based memristors. In a period where Moore's law is highly challenged [2] and the demand of modern society for high-density memories is constantly increasing [98], fundamentally new electrically switchable structures are needed to further push technological limits. Memristive devices (or memristors) have shown great potential as alternative building blocks for non-volatile memories and computing applications beyond the von Neumann architecture [99]. Memristors with multiple resistive switching states enable the realization of neuromorphic computing on a hardware level, making it important to investigate such structures further [100].

A memristor is a resistor with memory. Under applied bias V_b, it switches from a high-resistance state (HRS) to a low resistance state (LRS) as shown in Fig. 7.1a, with the change in resistance being non-volatile. The initial conception of a memristor by Chua in 1971 [101] and its first experimental

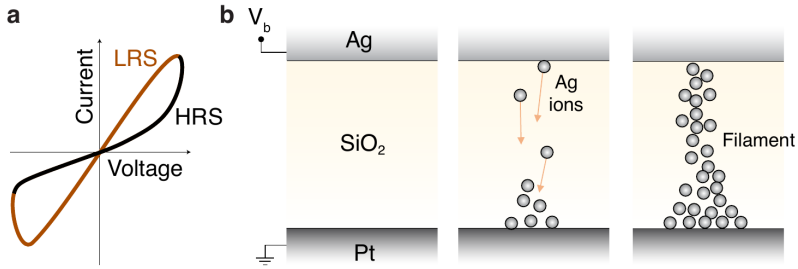

Figure 7.1: (a) Typical hysteretic I-V characteristics of a memristor where with increasing voltage the resistive state switches from high (HRS) to low resistance (LRS). In the case of a bipolar device, resetting is accomplished with an opposite applied voltage. (b) Illustration of an ion migration memristor. Ag ions directionally diffuse to the Pt electrode, when the device is under bias V_b. A filament is formed that changes the resistive characteristic of the device from HRS to LRS.

demonstration in 2008 [102] were followed by substantial research efforts to investigate the mechanisms involved in memristive switching and optimize their characteristics. Since then, several memristive mechanisms have been observed, such as electrochemical metallization [103], valence-change [104] and phase-change effect [105]. As an example, Fig 7.1b illustrates the process of operation of a memristor based on ion migration. When voltage is applied across the Ag/SiO_2/Pt tunnel junction Ag ions migrate from Ag to Pt [106, 107]. Their gradual accumulation leads to a formation of a filament (electrochemical metallization) that when it bridges the tunneling barrier the device switches to the LRS phase exhibiting memristive behavior in that way. Current state-of-the-art memristor cross-bar arrays feature ~ 10 nm-sized active regions, at par with today's silicon CMOS integrated circuitry [108]. Further scaling down the dimensions of memristors brings more challenges than benefits especially in terms of stability, reproducibility and robustness.

The rise of two-dimensional (2D) materials has attracted attention to them as an alternative platform for potentially miniaturizing memristive devices [109–116]. Recent reports have shown very low leakage currents in 1L MoS_2 based memristors compared to traditionally used oxides, allowing thickness scaling down to less than 1 nm [115, 117, 118]. However, the underlying mechanisms behind the memristive effects observed in 2D materials are not

yet completely understood, especially in devices employing monolayers for switching [115, 116, 118]. While in monolayer TMDs, a recent STM study has shown that point defects like sulfur vacancies can give rise to memristive effects through Au ion migration [28], in multilayer TMDs independent studies have revealed contrasting findings, attributing the underlying mechanism to either phase-transition or defect mediated atomic migration [110, 119]. However, a detailed investigation into the influence of varying defect densities and fabrication process parameters on the memristive characteristics in 2D TMDs is still lacking.

Here we perform a comparative study of memristors built by intentionally introducing defects in 1L-MoS_2 together with pristine ones fabricated by defect-free contact techniques. Our experimental findings reveal that memristors comprised of defective TMDs switch at lower voltages as well as exhibit a stronger change in resistance compared to pristine ones. We support our observations with *ab initio* quantum transport simulations and develop a model that suggests the existence of an optimum range of defect densities at which the resistive switching difference is maximum.

7.1 Device Preparation

Our memristors were built by sandwiching 1L-MoS_2 between 1L-graphene and 50 nm of gold (Au) top and bottom electrodes, respectively, in a vertical charge transport configuration. MoS_2 crystals synthesized by chemical vapor transport (CVT) with 99.9999% purity were purchased from 2D Semiconductors®. MoS_2, graphene and hexagonal boron-nitride (hBN) flakes were mechanically exfoliated from bulk crystals on Si/SiO_2 substrates. A poly-dimethylsiloxane (PDMS) stamp covered by a thin polycarbonate (PC) film [120] was used to sequentially pick-up top hBN, graphene and MoS_2 flakes in air. The resulting stack was then transferred on top of Au electrodes pre-patterned by photolithography on a glass substrate (see Appendix A.1). It is known that evaporation of contact metals, including Au can introduce a significant amount of defects in MoS_2 and lead to metal-MoS_2 chemical bonding [121]. The use of graphene as a top electrode in our devices allows for evaporation-free fabrication, thereby preventing any inadvertent defect generation in MoS_2 due to metal evaporation and decoupling the influence of contact metallization

on the memristive behavior, something that has been overlooked in previous studies [117]. The dry pick-up and assembly avoids polymer and solvent contamination at any stage, resulting in pristine interfaces. Moreover, the asymmetric electrode configuration allows for material oriented analysis of the results connecting the memristive effect to Au ion migration as it is discussed later in this manuscript. Furthermore, the top hBN encapsulation avoids material degradation during measurements under ambient conditions. Thus, the above fabrication methodology preserves the purity and high crystal quality of our MoS_2 flakes at every step, allowing us to study MoS_2 in its pristine state, in strong contrast to previous studies [115]. In order to compare the memristive performance between pristine MoS_2 and those with increased defect densities, we also built devices by intentionally introducing defects in MoS_2 flakes after exfoliation.

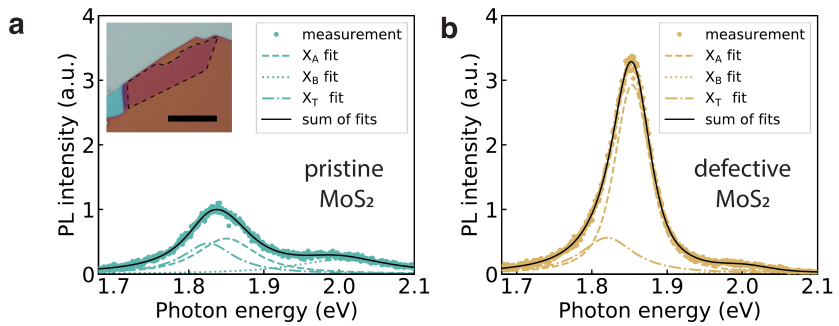

Figure 7.2: (a,b) Photoluminescence spectra of (a) an as-exfoliated (pristine) MoS_2 flake on Si/SiO_2 substrate and (b) after HV annealing at 400 °C (defective). X_A, X_B and X_T refer respectively to the A-exciton, B-exciton and trion spectral contributions, fitted with Voigt distribution functions. Both spectra were measured from the same MoS_2 region with 532 nm laser excitation at 24 µW power under ambient conditions and were normalized to the peak intensity of the spectrum in (a) for ease of comparison. Inset in (a) shows an optical microscope image of the MoS_2 flake before annealing (monolayer outlined by black dashed line). The scale bar is 12.5 µm.

In Ch. 2 we discussed defect generating processes and the impact of them in the PL emission. We use these two methods, i.e. vacuum annealing and

Ar sputtering in order to controllably generate defects in the MoS_2 crystal. Figures. 7.2a and b show the PL spectra of a monolayer MoS_2 flake before (pristine) and after HV annealing (defective) is presented. A strong enhancement of the A-exciton (X_A) PL contribution is observed after annealing that serves as evidence for creation of S vacancies, as discussed in Ch. 2. Lastly, in order to study the impact of defects introduced during evaporation of metal electrodes on the memristive behavior of MoS_2 devices, we also fabricated devices with graphene as the bottom electrode and evaporated Au as the top electrode, following an inverse stacking sequence. It has been shown that during Au-evaporation, Mo and S atoms can be substituted by Au atoms leading to defects in the MoS_2 layer [121] that can favor the formation of conductive channels and thereby enhance the memristive effect.

7.2 Electrical Characterization

The memristive performance of the devices prepared with different defect densities and fabrication procedures was electrically characterized by applying a voltage pulse sequence and measuring the current with a low noise source-meter. A periodic triangular bipolar pulsed sweep was performed with an offset voltage V_{read} to allow for low voltage estimation of the resistance after every applied pulse (see Fig. 7.3a). Pulsed electrical measurements have a dual benefit. Firstly, continuous electrostatic stress for long periods of time is avoided, which was found to increase the lifetime of our devices and allowed us to study their behavior at voltages as high as 7.5 V without any apparent degradation. Secondly, this procedure prevents any inadvertent parasitic hysteresis due to charge accumulation from influencing our measurements. This ensures that the hysteresis we observe arises solely from a non-volatile resistance change, indicative of memristive behavior. Pulsed I-V measurements of devices with pristine and vacuum annealed MoS_2 are plotted in Figs. 7.3b and c respectively for comparison. Every point in the plot corresponds to the average value of the current flow during an applied voltage pulse versus the magnitude of that pulse. In the pristine device, we only observe a weak hysteresis even after applying significantly high voltages ($V_{\text{peak}} = \pm 7$V). In the case of vacuum annealed MoS_2, the hysteresis gets enhanced and appears at lower applied

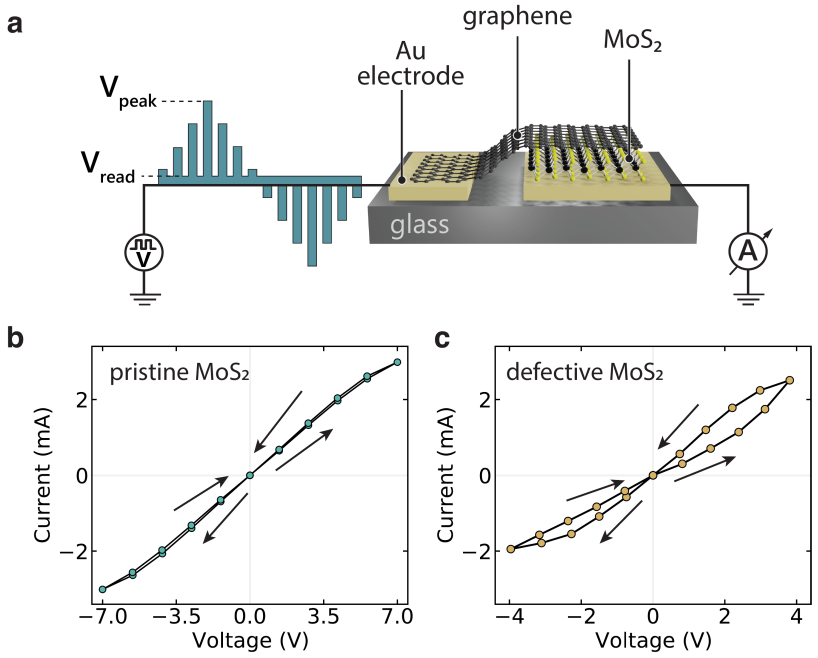

Figure 7.3: (a) Schematic illustration of a memristor built by sandwiching 1L-MoS_2 between graphene and Au electrodes. The top hBN flake used for encapsulation has been omitted from the illustration for clarity. Electrical measurements were performed using pulsed voltage sweeps to eliminate hysteresis. After each write pulse, the device resistance was probed with a much lower read voltage (V_{read} = 100 mV). Pulse duration and period is 10 ms and 30 ms respectively. (b,c) Pulsed I-V measurements of memristors with pristine and defective 1L-MoS_2 flakes showing an enhanced switching behavior after high temperature annealing. The black arrows indicate the voltage sweep directions in both plots. All measurements were carried out at room temperature.

voltages compared to the pristine MoS_2 device. We attribute this effect to the increased defect density of the MoS_2 flake caused by high temperature annealing. This is the first indication that an increase in defect density can provide the means for a stronger memristive performance. Moreover, the devices switch from a high resistance state to a low resistance state only with a positive voltage applied at the Au electrode while graphene is grounded. This polarity dependent switching behavior is a strong indication that this effect

relies on material specific properties. More specifically, we attribute this effect to the migration of Au ions from the Au electrode to the defect sites of the MoS_2 flake. It is well known that Au atoms can ionize and migrate under the influence of an applied electric field. Defect sites offer an energetically favorable state for Au ions to bond with the MoS_2 crystal. This process can be reversed by flipping the direction of the applied electric field. Since bound Au atoms at the MoS_2 flake lower the resistance of the Au-MoS_2 interface this can lead to resistive switching effects when excited with a bipolar voltage sweep [28]. We also observed an increased hysteresis in devices with Ar sputtered MoS_2 as well as in those with evaporated Au as a top electrode , which further corroborates our hypothesis. A comparison of I-V measurements from differently treated devices can be found in Appendix C.

Although hysteresis in the I-V characteristics is a strong indicator of the occurrence of resistive switching in our devices, to gain further insight we also characterized their resistance at low voltages during the pulsed sweep. After every applied pulse, the device resistance is measured at $V_{\text{read}} = 100\,\text{mV}$ as it is indicated in Fig. 7.4a, which shows a timetrace of the applied sweep. Fig. 7.4b presents the change in resistance $\Delta R = R_0 - R_{\text{read}}$ during the pulsed voltage sweep, where R_0 is the resistance measured before starting the sweep and R_{read} is the resistance measured after each pulse. Results from different devices have been shown for comparison. Pristine MoS_2 #1 and #2 refer to two devices fabricated with the non-invasive fabrication procedure discussed earlier without doing any treatment of the MoS_2 flake. Au evaporated #1 and #2 refer to two devices with evaporated Au top electrode and graphene bottom electrode and using otherwise untreated MoS_2. Ar sputtered and vacuum annealed refer to devices with MoS_2 flakes treated with the corresponding methods. In all devices the same voltage sweep range was used with ($V_{\text{peak}} = \pm 4\,\text{V}$). We define the ON region as the region after the application of the highest voltage pulse and before the application of the lowest one. The region before and after the ON region is referred to as the OFF region. A clear difference in the magnitude of ΔR between pristine and defective devices can be seen, with the latter exhibiting a stronger change in ΔR.

We use ΔR to compare different devices since it cancels out any other series resistances such as contact and graphene sheet resistance. However, resistance

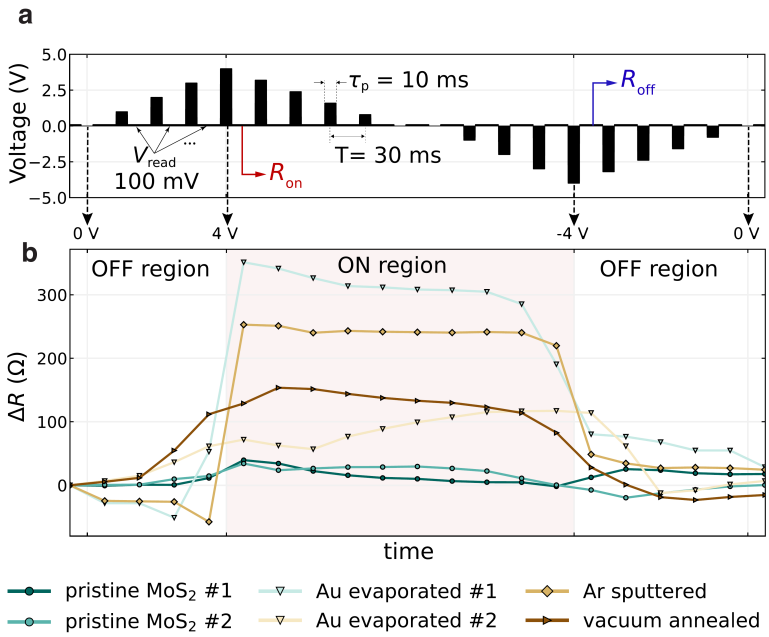

Figure 7.4: (a) Time-trace of the applied voltage sweep. Black solid arrows indicate the low-voltage regions where the resistance is measured. Black dashed arrows indicate the voltage level positions for 0, 4 and -4 V. Pulse duration τ_p = 10 ms and pulse period T = 30 ms. Red and blue arrows indicate the time instances where the R_{on} and R_{off} values are measured respectively. (b) Time-trace of the low voltage resistance difference ΔR for different devices measured during the pulsed voltage sweep presented in (a). The resistance is measured with V_{read} = 100 mV after every applied pulse. An increase in ΔR in the ON region can be observed for all devices. However, the defective devices show a much stronger increase in ΔR compared to the pristine ones.

also scales with the vertical junction area in every device, which is difficult to estimate accurately from optical microscope images due to edge effects at the graphene/MoS_2/Au junction interface. Therefore, the switching ratio, which is an experimental quantity that is immune to the variations in junction areas among different devices was also investigated. The switching ratio is given by R_{off} /R_{on} where R_{off} and R_{on} are the resistances of the device after the application of the largest and the smallest voltage pulses as indicated in Fig. 7.4a with blue and red arrows, respectively. The total resistance measured also includes the series graphene sheet resistance which can vary between

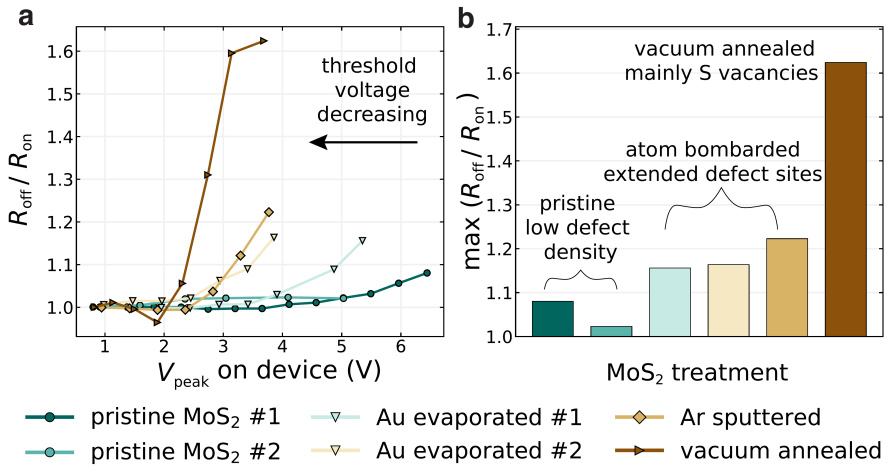

Figure 7.5: (a) Switching ratio R_{off}/R_{on} as a function of V_{peak} for all reported devices. (b) A comparison of the maximum switching ratio achieved for the different MoS_2 treatments associated with different defect types and densities. Colors in the plot correspond to the legend shown at the bottom.

devices. To estimate its contribution to the overall resistance and subtract it from R_{off} and R_{on} values we estimated the graphene sheet resistance per unit of length by fabricating a multi-electrode device where Au electrodes with different spacings were connected by one graphene flake and performing transmission line measurements. The estimated graphene resistance was then subtracted from the total device resistance according to the graphene electrode length used in each device.

Taking the aforementioned under consideration, in Fig. 7.5a we plot the switching ratios R_{off}/R_{on} for sweeps performed with different V_{peak} values for all devices. Here the values of V_{peak} have been adjusted to account for the voltage drop across the graphene sheet. Again we observe that in the case of pristine devices, the ratio reaches a value of 1.1 only at high V_{peak} voltages around 6.5 V whereas for the cases of devices with higher MoS_2 defect density, the ratio reaches values as high as 1.6 at much lower V_{peak} values. This clearly indicates that higher defect densities can lead to memristive switching enhancement, demonstrating at the same time the ability to control the memristive performance by controlling the defect density of the active material, monolayer MoS_2 in our case. In Fig. 7.5b, we plot the maximum ratio achieved experimentally for

the different MoS_2 treatment procedures. Interestingly, we find that vacuum annealing leads to the highest switching ratio at low V_{peak} voltages. Our PL spectroscopic analysis reveals that in this case mainly S vacancies are created in the crystal whereas in the cases of Ar sputtering and evaporation of Au as a top electrode, more extended defect sites are expected to be created. The existence of extended defect states lowers the R_{off} and hence when Au atoms diffuse into the vacancy sites, a smaller change in R_{on} is observed leading to a lower switching ratio.

Although increasing the defect density showed an enhanced memristive behavior, our results are in contrast with recent reports of vertical graphene/MoS_2/Au structures using CVD grown 1L-MoS_2 vacuum annealed at 600 K [115, 118] where switching ratios up to 10^4 were observed owing mostly to its high R_{off} value. However, the fabrication process reported included invasive steps like direct contact with polymers and solvents like PDMS and DI water among others which compromises the interface quality and introduces contaminants. In addition to that, CVD grown MoS_2 crystals are expected to exhibit high defect densities. The role of high defect densities is explored here theoretically.

7.3 Quantum Transport Modeling

In order to better understand the expected resistance of such a structure and explore the theoretical limits of operation we utilize an *ab-initio* quantum transport simulation framework [123]. An illustration of the simulation models considered are presented in Figs. 7.6a, b and c, where different configurations of the MoS_2 crystal are taken into account: pristine, with one V_S and with a migrated Au atom at the V_S site. The cell area of the simulation is A = 2.14×3.79 nm^2. The resistances are calculated for an interlayer distance d = 4.7 Å (Fig. 7.6c). The interlayer distance has been chosen as the one where $R_{V_S} - R_{Au}$ is maximum. This resistance difference diminishes at smaller and larger interlayer distances due to the metal induced gap states, and high tunneling resistances, respectively.

By increasing the number of defects in the cell area of the simulation we can evaluate the resistance as a function of defect density (colored dots in figure 7.6d). Due to limits on the cell area size posed by computation time, the region

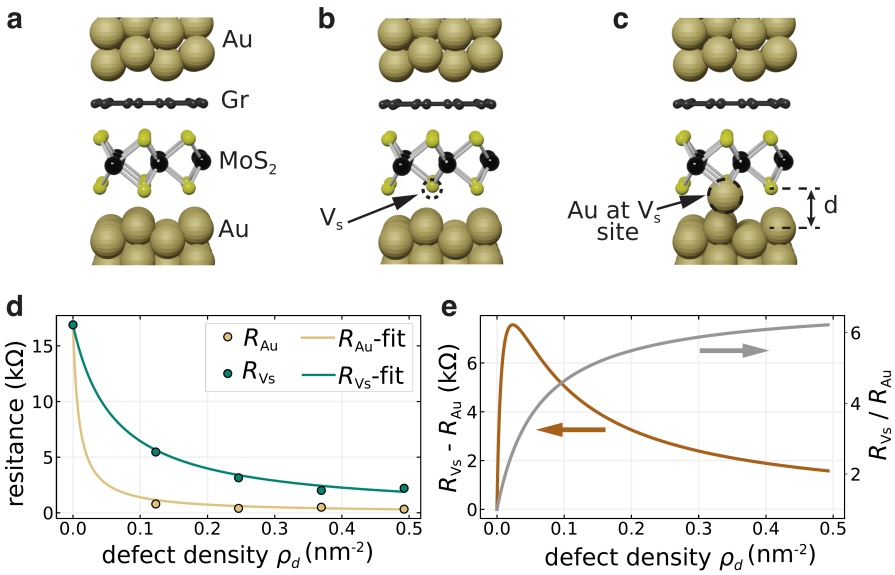

Figure 7.6: (a-c) Illustration of the atomic models simulated with (a) pristine MoS_2, (b) one sulfur vacancy V_S and (c) with one Au atom at the V_S site. (d) Resistance as a function of defect density ρ_d. Dots are simulation results (provided by Tarun Agarwal [122]) evaluated in the device models presented at a,b and c, for different defect densities and lines are fits of the classical resistance model. R_{Au} is the resistance evaluated in model in c, R_{V_S} is the resistance evaluated in model b and the resistance for defect density $\rho_d = 0$ (pristine) is the resistance of the model in a. The fit function is given in equation 7.1. (e) Calculated values of resistance difference R_{V_S} -R_{Au} and resistive ratio R_{V_S} /R_{Au} using the fitted values in d.

of low defect densities cannot be easily explored thus we employ a classical model of prediction of the resistance as a function of defect density ρ_d. We define the estimated resistance for the pristine, one V_S and Au at V_S site case as R_{pr} , R_{V_S} and R_{Au} respectively. The estimated overall resistance is then written as:

$$R(\rho_d) = \frac{R_{pr} \cdot R_d}{R_d + (R_{pr} - R_d)\,\rho_d \cdot A} \tag{7.1}$$

where R_d refers to either R_{V_S} or R_{Au} for one defect, depending on the type of the defect that is calculated. Details on the formation of the model can be found in Appendix C. We use the simulation results to fit the function in equation

7.1 and the result is shown in Fig. 7.6d. Both R_{V_S} and R_{Au} are dropping with increasing ρ_d owing to the defect states appearing inside the MoS_2 bandgap with R_{Au} taking lower values than R_{V_S} indicating the ability of Au migration to cause resistive switching. The difference in resistance $R_{V_S} - R_{Au}$ as well the switching ratio R_{V_S}/R_{Au} is plotted as a function of ρ_d in Fig. 7.6e. Interestingly $R_{V_S} - R_{Au}$ is not monotonic presenting a maximum in low ρ_d regions. On the other hand the switching ratio R_{V_S}/R_{Au} is increasing constantly with ρ_d and with a tendency to saturate. Although the ratio is increasing for high ρ_d, the resistances R_{V_S} and R_{Au} are dropping significantly making the performance dependent on any other possible series resistances of the system. However, at the region where $R_{V_S} - R_{Au}$ is maximum, the ratio R_{V_S}/R_{Au} is already at half of its maximum value making this region preferable for memristive operation. These results reveal the need for defect engineering of such memristive devices for optimized performance. Furthermore, for $\rho_d \to \infty$, $R_{V_S}/R_{Au} = 6.8$. Although the case of infinite ρ_d seems non-physical it can be translated to the case of a Au STM tip over a V_S site exchanging a Au atom. Recent studies have experimentally demonstrated this, reporting a very similar switching ratio for the same interlayer distance range [28]. This increases the validity of our simulations and predictive model. Furthermore, our experimental observations confirm qualitatively the theoretical prediction that increasing the defect density of the material is increasing the ΔR and the R_{off}/R_{on} ratio.

7.4 Discussion

We have limited knowledge on the actual defect densities in the fabricated devices as well as on other possible sources of resistance such as bubbles, residues and unaccounted contact resistances, hence a precise quantitative comparison between theory and experiment is difficult. However, the switching ratio observed experimentally and predicted theoretically lie in the same order of magnitude. An important result is that the R_{V_S} (the R_{off} value) drops significantly with increasing ρ_d due to defect states in the bandgap when at the same time the switching ratio saturates. By comparing this with previous results [115] we can assume that the CVD-grown MoS_2 defect density is not the intrinsic reason for which high switching ratios have been observed [115, 118] underlying the role of the fabrication process in introducing contaminants which are not necessarily

specific to the active material itself. However, in the case of multiple multilayer domains at the CVD crystals higher R_{off} values can be possible making the thorough analysis of the material quality before fabrication an important step towards understanding. Finally, taking into account the experimental results presented in this text through non-invasive means of fabrication that guarantees a flat interface, the switching ratio remains low in accordance to theoretical predictions that can be validated by STM studies previously reported [28] which further supports the previous argument.

7.5 Conclusions

To conclude, we fabricated different monolayer MoS_2 memristive devices by employing non-invasive fabrication methods with pristine, Ar sputtered and vacuum annealed MoS_2 as well as devices with evaporated Au as a top electrode. We compared their memristive performance and showed that with increased defect density, both ΔR and R_{off} /R_{on} ratio get enhanced. We attribute this effect to Au ion migration to MoS_2 defect sites. Our experimental observations are in good agreement with numerical and theoretical models. Moreover, we explored the relation between defect density and memristive performance and we revealed the existence of an optimum range of defect densities for designing efficient memristors based on Au ion migration.

8

Conclusions & Outlook

In this thesis we explored the optoelectronic characteristics of 2D material tunnel junctions with the focus on understanding light emission and memory mechanisms in such heterostructures. By using a combination of only four materials (graphene, hBN, TMDs and gold) in different configurations it was possible to investigate different physical mechanisms like inelastic tunneling emission, electroluminescence, charge injection, energy transfer and ion migration. Effectively, the work presented can be put in two big categories: 1) Light emission from van der Waals heterostructures and 2) Ion migration in monolayer MoS_2 memristors. For each category a summary of the main results along with an outlook are presented in the following sections.

8.1 Light emission from van der Waals heterostructures

8.1.1 Double tunnel barrier light emitting devices

In Ch. 3 we experimentally demonstrated polarity-dependent electroluminescence with an asymmetric Gr/hBN/TMD/hBN/gold LED. We also observed

excitonic emission at voltages below the electronic bandgap. The polarity-dependent emission spectrum is related to the fact that gold has higher DOS than graphene and TMD's DOS is in between the two. The emission is understood as direct tunneling to excitonic states due to an already hole-occupied VB. As a next step, gate-dependent studies in asymmetric (Fig.8.1a) and symmetric (Fig.8.1b) devices would shed more light in the mechanisms of direct exciton creation and interplay between trionic and excitonic emission below electronic bandgap. In addition, gating has been shown to modulate the luminescence efficiency of the TMD [24] allowing in that way to evaluate the efficiency limits of direct exciton creation.

8.1.2 TMD-coupled tunnel junctions

Other possible mechanisms contributing to the emission in TMD-based LEDs, namely tunneling electrons optically coupling to the excitonic states, were explored in Ch. 5. There, in order to decouple charge injection effects from the light emission process, we studied an unconventional and novel design of light emitting devices where the TMD is sitting on top of a tunnel junction. We observed excitonic emission that we interpret as ET from tunneling electrons to excitons, demonstrating in that way that optical coupling between electrons and TMDs can be efficient in such heterostructures. We showed as well that exciton generation rate in the TMD is increasing with decreasing distance. However, ET

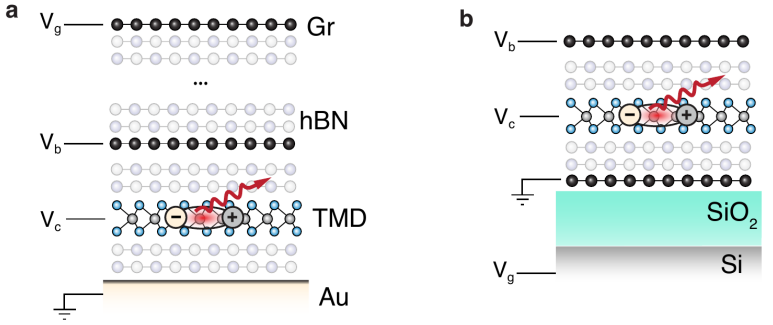

Figure 8.1: Alternative LED structures, with (a) assymetric and (b) symmetric electrodes in a gated configuration that allows light collection through the graphene layers at the top. V_g and V_c are the gating and the TMD control voltage, respectively.

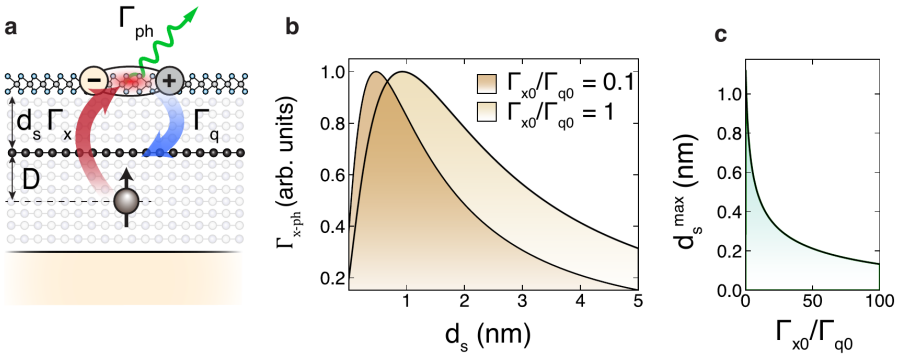

Figure 8.2: (a) Device schematic showing the corresponding rates that define Γ_{x-ph}. (b) Γ_{x-ph} as a function of distance d_s for various Γ_{x0}/Γ_{q0} ratios. (c) The distance d_s at which Γ_{x-ph} is maximum (d_s^{max}) as function of the ratio Γ_x/Γ_q.

from the TMD to graphene quenches part of the emission. Towards optimizing the design for efficient light emission we calculate the rate with which the transition dipole is generating excitons that radiatively decay as

$$\Gamma_{x\text{-}ph} = \frac{\Gamma_x \Gamma_{ph}}{\Gamma_x + \Gamma_{ph}} = \Gamma_x - \frac{\Gamma_x \Gamma_q}{\Gamma_x + \Gamma_q} \tag{8.1}$$

where Γ_x is the decay rate of the transition dipole to excitons, Γ_{ph} is the radiative decay rate of excitons and Γ_q is the non-radiative decay rate of excitons to graphene (quenching rate) as presented in Fig. 8.2a. Here we used the relation between the lifetimes ($\tau_{x\text{-}ph} = \tau_x + \tau_{ph}$) and the rates ($\Gamma_x = \Gamma_{x\text{-}ph} + \Gamma_{x\text{-}q}$). Our experimental results and model, as presented in Fig. 5.5d, suggested a $1/d^2$ dependence for Γ_x. By assuming the same dependence for Γ_q we can define them as

$$\Gamma_x = \frac{\Gamma_{x0}}{(d_s + D)^2}\ , \quad \Gamma_q = \frac{\Gamma_{q0}}{d_s^2} \tag{8.2}$$

where Γ_{x0} and Γ_{q0} are proportionality factors for the exciton generation and quenching rate, respectively, D is the distance between the dipole and graphene and d_s is the distance between the TMD and graphene as presented in Fig. 8.2a. We calculate $\Gamma_{x\text{-}ph}$ as a function of d_s for different Γ_{x0}/Γ_{q0} ratios. The result is

shown in Fig. 8.2b where we observe the existence of an optimum thickness d_s for a maximum Γ_{x-ph} depending on the Γ_{x0}/Γ_{q0} ratio. Figure 8.2c shows the optimum distance d_s^{max} as a function of the ratio. The little knowledge we have on that ratio prevents us from defining the optimum distance in an absolute way. However, d_s values around 1-2 nm seem to offer a good $\Gamma_{x\text{-}ph}$ for a big range of Γ_{x0}/Γ_{q0}. The model presented in Fig. 8.2 is a simplification of a more complicated system and there is room for optimizing more parameters. There are various non-radiative mechanisms that play a significant role in the efficiency, like gold quenching or other non-radiative decay mechanisms intrinsic to the TMD (trion formation, non-direct transitions etc.). There are different ways to tackle such issues. First, the gold electrode can be replaced by graphene for reducing the quenching and also making use of resonant electron tunneling as demonstrated in Gr/hBN/Gr tunnel junctions [124]. For reducing non-radiative pathways in the TMD itself it has been shown that chemical treatment, gating or strain can enhance radiative decay [23–25], as commented in Ch. 2, making this techniques worthy of investigation in TMD-coupled tunnel junctions.

Moreover, the electrical generation of excitons via ET, presented in this thesis, provides new perspectives for the development of optical sources, detectors or TMD-based sensors [125]. For example, such structures can enable all-electrical sensing without relying on external optical sources as in applications where illumination is necessary. Photocurrent or PL measurements are commonly used for sensing when at the same time the TMD layer should be exposed to the environment as demonstrated in NO_2, O_2 or N_2 sensing [29, 126]. Such a concept but all-electrically driven, employing TMD-coupled tunnel junctions, is illustrated in Fig. 8.3a making use of the fact that the TMD can be exposed while driven electrically. In terms of source applications, and under the view of ET being an efficient process, electrical pumping schemes can also be investigated towards vdW heterostructure lasers [127, 128] where the optically active material is separated by the driving electrodes. Finally, the same principle of ET in tunneling junctions can be used between different TMDs [129] for photodetection enhancement as illustrated in Fig.8.3b. Upon illumination the TMD that sits outside of the tunnel junction (WS_2) can generate excitons in the TMD inside the junction ($MoSe_2$) through energy transfer. In

that way the photo-response can be increased while the time response is limited by the thickness of only one flake ($MoSe_2$) [130] and by the speed of the energy transfer process that has been shown to occur within picoseconds [129].

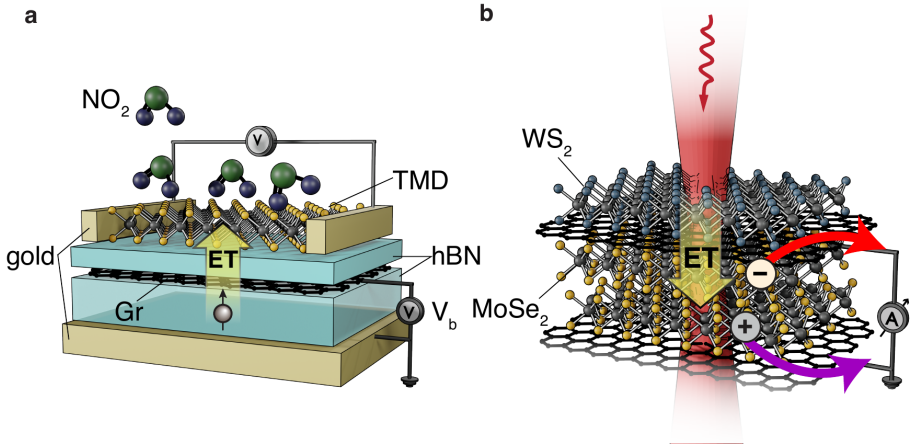

Figure 8.3: (a) Proposed device schematic on all-electrical gas sensing. Illumination was shown to increase the sensitivity [126]. Here electron-hole pairs are generated by ET through a tunnel junction with the TMD being able to come in direct contact with the surrounding gas. (b) Photodetection scheme with $MoSe_2$ in a tunnel junction optically coupled to a WS_2 monolayer. Photocurrent is generated from electron and hole separation due to light absorption from $MoSe_2$. Additional response is expected due to photon absorption and exciton generation in WS_2 and subsequent ET to $MoSe_2$.

Finally, in Ch. 6 we explored the transport characteristics of TMD-coupled tunnel junctions and we observed resonant features at excitonic energies. Our results are understood as exciton-assisted tunneling by optical coupling to indirect excitonic modes that can bridge the momentum mismatch between graphene and gold. Our work not only demonstrates an all-electrical method for measuring optical properties of 2D materials, but also reveals the high efficiency of the exciton-assisted tunneling process, especially for the cases where hBN is thick enough to amplify the inelastic tunneling effect. However, the increased exciton generation efficiency cannot be translated to increased emission efficiency due to coupling to indirect excitons. An investigation of different electrode configurations (e.g. graphene-graphene electrodes) might allow coupling to direct excitons that can lead to an increase in emission

efficiency. Finally, a more detailed description of the interactions between excitons and electrons as well as a thorough investigation of the different exciton characteristics between different TMDs and how these can be related to the resonant features, might shed light on the mismatch between the energy values observed in our dI/dV measurements and the reported values for indirect excitons.

8.2 Ion migration in monolayer MoS_2 memristors

In Ch. 7 we investigated the role of defects in monolayer MoS_2 memristors based on ion migration. We fabricated memristors with different defect generating techniques and we investigated their memristive characteristics. Moreover, we theoretically explored the relation between defect density and memristive performance and we revealed the existence of an optimum range of defect densities for designing efficient memristors. Our experimental observations are in good agreement with numerical and theoretical models. Additionally, we compared our results with previous studies on monolayer MoS_2 and concluded that Au-ion migration cannot be the sole reason for the reported results in [115]. Our analysis establishes a clear understanding of the origin of resistive switching in MoS_2 monolayers and provide guidelines for controlling their memristive performance. The monolayer MoS_2 memristor performance is limited by the leakage currents. The defect-generating processes introduced in Ch. 2 and analysed in Ch. 7 can potentially allow the usage of thicker flakes for stronger

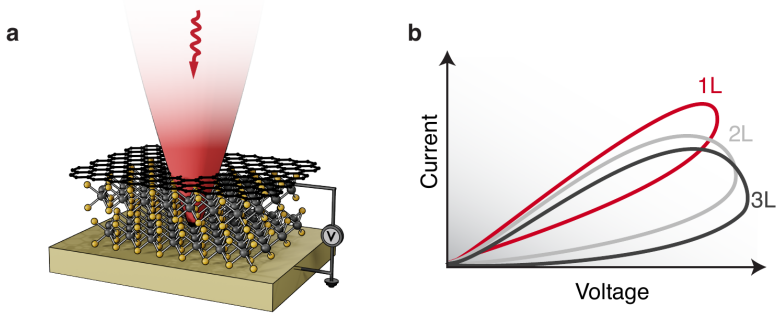

Figure 8.4: (a) Treated multilayer MoS_2 memristors for stronger memristive effects. Control of memristive behavior with illumination. (b) Illustration of the memristive effect progression with increasing TMD thickness.

memristive effects (see Fig. 8.4a and b). The use of graphene as a top electrode allows the investigation of optical addressing and control of the memristive effect (see Fig. 8.4a). Along with the high refractive index of TMDs this might be a promising platform towards photonic based neuromorphic computing that goes beyond the von Neumann logic and avoids the power consumption of dense electronics. Such studies have been reported for bulk material devices in the past [106, 131] and the usage of 2D material stacks can enable their miniaturization.

A

Methods

A.1 Fabrication of van der Waals heterostructures

The fabrication process of all the 2D heterostructures presented in this thesis is done by a dry pick-up method [120] in three steps: 1) Exfoliation, 2) stacking and 3) transfer. The 2D material flakes used are mechanically exfoliated on Si/SiO_2 chips with the scotch-tape method [5]. Part of the bulk crystal (Fig. A.1a) is removed by the tape (Fig. A.1b,c) and is further exfoliated down through out the tape area (Fig. A.1d) with repetitive movements as in Fig. A.1b. Then with a smaller tape we take a part of the exfoliated crystal from the first tape (Fig. A.1e) and we press it against a Si/SiO_2 chip that was previously cleaned for 5-10 mins in an O_2 plasma asher (Fig. A.1f). We then pull gently the tape in a high angle (almost 180°) as in Fig. A.1g. It is useful to have the chip on a sticky surface (blue area in Fig. A.1g) to remain stable during this process. Then the chip is put under an optical microscope and by close inspection we locate the flakes of interest as presented in Fig. 1.1. Different SiO_2 thicknesses are used for exfoliating different flakes. The contrast of graphene and hBN flakes is higher at 100 nm SiO_2 whereas the TMDs are better visible at 285 nm SiO_2. After locating all the needed flakes for the design of the heterostructure

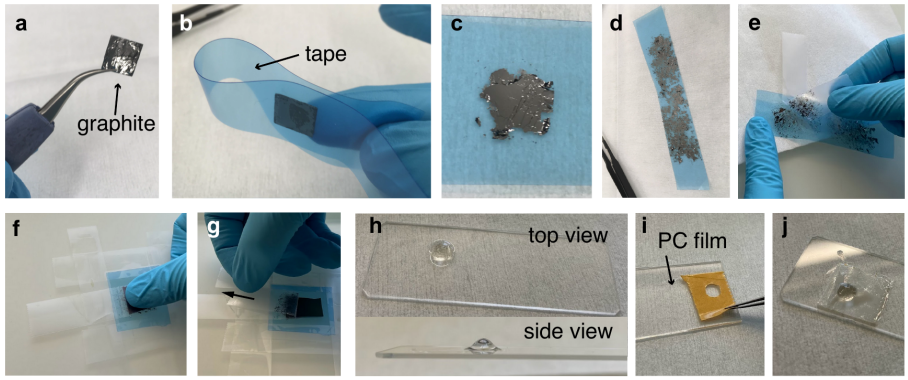

Figure A.1: (a) A piece of graphite is put on sticky tape (b) where a part of it remains after removal (c). By repetitive motions as in (b) the graphite is exfoliated and shared on a big surface (d). With a smaller tape we take part of the graphite (e) and press it against the substrate (f). We pull the tape at a high angle for exfoliating the flakes on the substrate (g). Top and side view of the PDMS droplet on a glass coverslip. (i) Double-sided tape on PC film. (j) A finalized PDMS/PC stamp.

we start stacking them together. The stacking is done with the help of a miniscus-shaped Polydimethylsiloxane (PDMS) droplet (Fig. A.1h). The droplet sits on a glass coverslip and is prepared by letting liquid phase PDMS dry with the droplet facing down over a hotplate at 80°C for several hours. The PDMS droplet is then covered by a thin polycarbonate (PC) film. The film is made by pouring PC dissolved in chloroform on a glass coverslip and later pressing and sliding a second coverslip on it. After chloroform evaporates, part of the PC film is removed with a double sided sticky tape 2x2 cm with a hole in the middle, made by a hole-puncher (Fig. A.1i). This creates a surface with a PC membrane at the hole. We stick the tape with the second sticky surface on top of the droplet in a way that the hole with the PC membrane aligns with the top of the PDMS droplet (Fig. A.1j).

This PDMS/PC stamp is now used for stacking the heterostructure. As shown in Fig. A.2 the stamp is positioned on top of the flake with a motorized stage and the help of a microscope. Then the PC film comes in contact with the flake, with the substrate being at 80°C. All flakes are picked-up one-by-one until the stack is complete. Then the stack is placed on top of the target substrate (usually glass) and the substrate is heat up to 176°C. The PC film melts at that

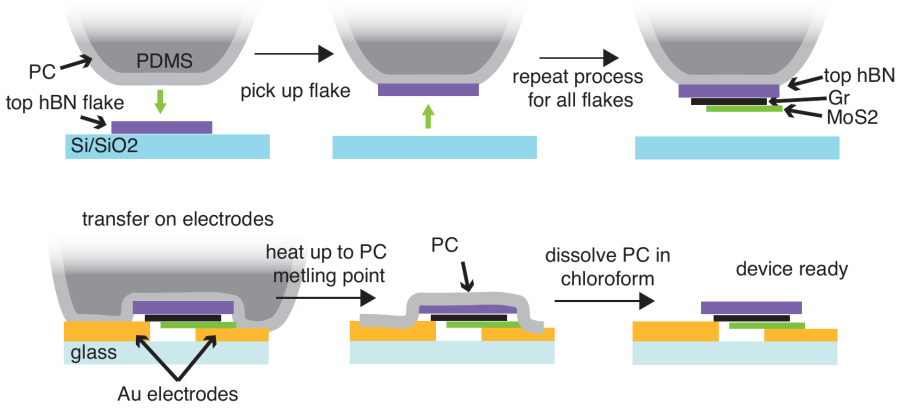

Figure A.2: Illustration of the stacking process of a hBN/Gr/MoS_2/gold heterostructure.

temperature and is transferred on top of the substrate along with the stack. The PC film is then dissolved by putting the whole chip in a chloroform bath. We transfer the stack directly on top of pre-patterned gold electrodes to make the electrical connection with the flake of interest. The fabrication is done in Ar atmosphere in a glovebox or in ambient conditions for the devices presented in Ch. 7. In all devices we use pre-patterned electrodes as part of the stack (bottom gold electrode) or to contact to the graphene electrode (top electrode). The pre-patterning is done by photolithography.

A.2 LDOS calculation in multilayer structures

In Ch. 4 and Ch. 5 we calculate the LDOS for complex multilayer structures. Here we outline the calculation process. Let us start from the simple case of an s-polarized electromagnetic field impinging on the interface between two material layers, layer 0 and layer 1, as shown in Fig. A.3. The electric field $\mathbf{E}$ for each side of the interface can be written as

$$\mathbf{E}_0 = \mathbf{E}_{A0} + \mathbf{E}_{B0} = \frac{A_0}{k_0}(-k_{y0}\hat{\mathbf{y}} - k_{z0}\hat{\mathbf{z}})e^{j\mathbf{k}_{A0}\mathbf{r}} + \frac{B_0}{k_0}(-k_{y0}\hat{\mathbf{y}} + k_{z0}\hat{\mathbf{z}})e^{j\mathbf{k}_{B0}\mathbf{r}} \quad \text{(A.1)}$$

$$\mathbf{E}_1 = \mathbf{E}_{A1} + \mathbf{E}_{B1} = \frac{A_1}{k_1}(-k_{y1}\hat{\mathbf{y}} - k_{z1}\hat{\mathbf{z}})e^{j\mathbf{k}_{A1}\mathbf{r}} + \frac{B_1}{k_1}(-k_{y1}\hat{\mathbf{y}} + k_{z1}\hat{\mathbf{z}})e^{j\mathbf{k}_{B1}\mathbf{r}} \quad \text{(A.2)}$$

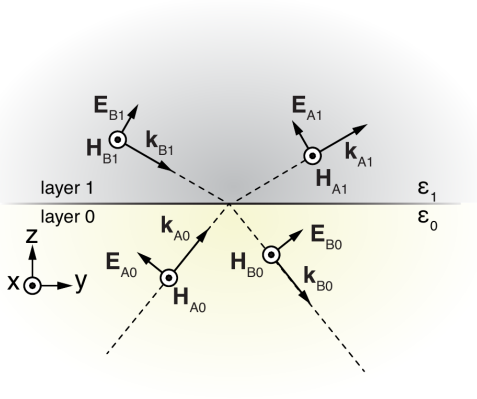

Figure A.3: An s-polarized electromagnetic field impinges on the interface of two different materials.

If i defines the layer number ($i = 0, 1$) then $\mathbf{k}_{Ai}$ and $\mathbf{k}_{Bi}$ are the wavectors for downward and upward propagating fields, respectively, with $k_i^2 = k_{zi}^2 + k_{yi}^2$. Finally, $\mathbf{r}$ is the spatial coordinate vector and A_i, B_i are the amplitudes for upward and downward propagating fields, respectively. After defining the fields in each layer we use the following boundary conditions

$$\hat{\mathbf{n}} \times \mathbf{E}_0 = \hat{\mathbf{n}} \times \mathbf{E}_1 \tag{A.3}$$

$$\hat{\mathbf{n}} \times \mathbf{H}_0 = \hat{\mathbf{n}} \times \mathbf{H}_1 \tag{A.4}$$

where $\mathbf{H} = \nabla \times \mathbf{E} / j\omega\mu$ is the magnetic field with ω being the angular frequency and μ being the magnetic permeability. These boundary conditions form an equation system that can be solved algebraically in order to define the amplitudes A and B.

This two-layer example can be expanded to systems with arbitrary numbers of layers (N), as illustrated in Fig. A.4. We can additionaly assume a dipole source sitting at layer n. The equation system is then written in a matrix format as

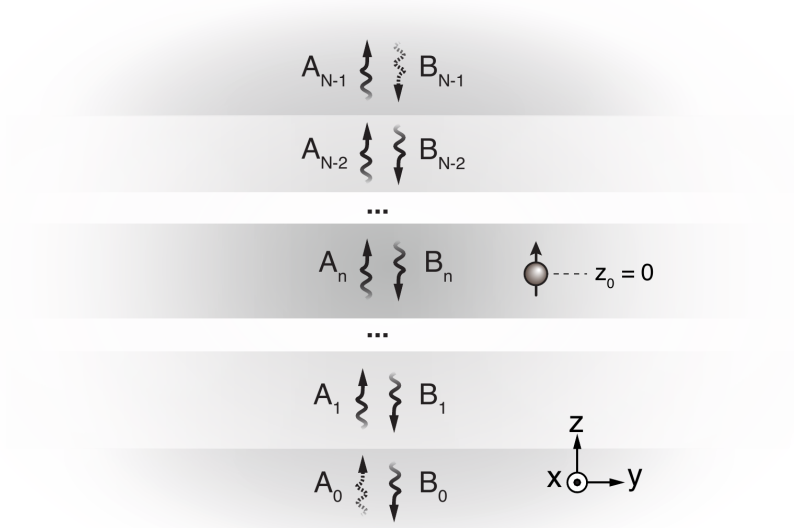

Figure A.4: A multilayer structure with N layers and a dipole situated at layer n. The upward and downward propagating fields in every layer are noted as A_i and B_i, respectively, where $i = 0, ..., N-1$.

$$\begin{bmatrix} a_{0,0} & a_{0,1} & \dots & a_{0,2N-1} \\ a_{1,0} & a_{1,1} & \dots & a_{1,2N-1} \\ \vdots & \vdots & \ddots & \vdots \\ a_{2N-3,0} & a_{2N-3,1} & \dots & a_{2N-3,2N-1} \end{bmatrix} \cdot \begin{bmatrix} A_0 \\ B_0 \\ A_1 \\ B_1 \\ \vdots \\ A_{2N-1} \\ B_{2N-1} \end{bmatrix} = - \begin{bmatrix} 0 \\ \vdots \\ a_{2n-2,2n} \\ a_{2n-1,2n} \\ a_{2n,2n+1} \\ a_{2n+1,2n+1} \\ \vdots \\ 0 \end{bmatrix}$$

where $n = 0, 1, ...N-1$ is the index of the layer where the dipole is situated and the first non-zero term in the signle-column matrix on the right hand side of the matrix system appears at position $2n-2$. In case the dipole is sitting at the first or last layer then the indices $2n-2$, $2n-1$ and $2n+1$ might exceed the range

$[0, N-1]$. In this case they can just be discarded as they are not involved in the calculation. In order to solve this equation system we need the matrix on the left hand side to be square. This is accomplished by incorporating the condition that $A_0 = B_{N-1} = 0$ since we assume semi-infinite first and last layer and no other sources than the dipole in layer n. The condition for the case of a dipole in the first or last layer is $A_0 = 1,\ B_{N-1} = 0$ and $A_0 = 0,\ B_{N-1} = 1$ respectively. The solutions of this system give us the amplitudes of upward and downward propagating fields for a given $k_y = k_\parallel$. The LDOS is then calculated by using Eq. 4.3.

A.3 Electrical and optical measurements

Figure A.5 describes the optoelectronics measurement setup used for all measurements presented in this thesis, except of the measurements in Fig. 6.3 whose methods are presented later. The connections to the devices prepared with the previous method are done by wire bonding the pre-patterned gold electrodes with adhesive copper pads which are put on top of the chip (sample holder view in Fig. A.5). Then the chip is connected to a sample holder that connects the copper pads to coaxial cable inputs. The sample holder is placed on top of a piezo stage on top of an inverted microscope. An ionizing fan is operating on top of the sample area while connecting it electrically. A similar fan is used also during the wire-bonding process.

PL measurements are performed by using an excitation laser of 532 nm. An objective with NA=0.9 is used for excitation and collection. The sample is put, facing down, on a Nikon TE300 inverted microscope in ambient conditions. The collected emission is then filtered by a long-pass (LP) filter. The PL map presented in Ch. 2 is measured by raster scanning the sample area with a piezostage and collecting the emitted PL with an avalanche photodetector (APD) with 70% quantum efficiency.

In electrically driven light emission measurements, the sample is connected to a Keithley Source Meter 2602B, that is used as a voltage source and current meter. The light emitted by the device under bias voltage is collected by the objective. All spectra are measured by imaging the real space of emission at the entrance of a Princeton Instruments Acton SpectraPro 300i spectrometer. The real and Fourier space (back-focal plane) of emission is imaged at the entrance

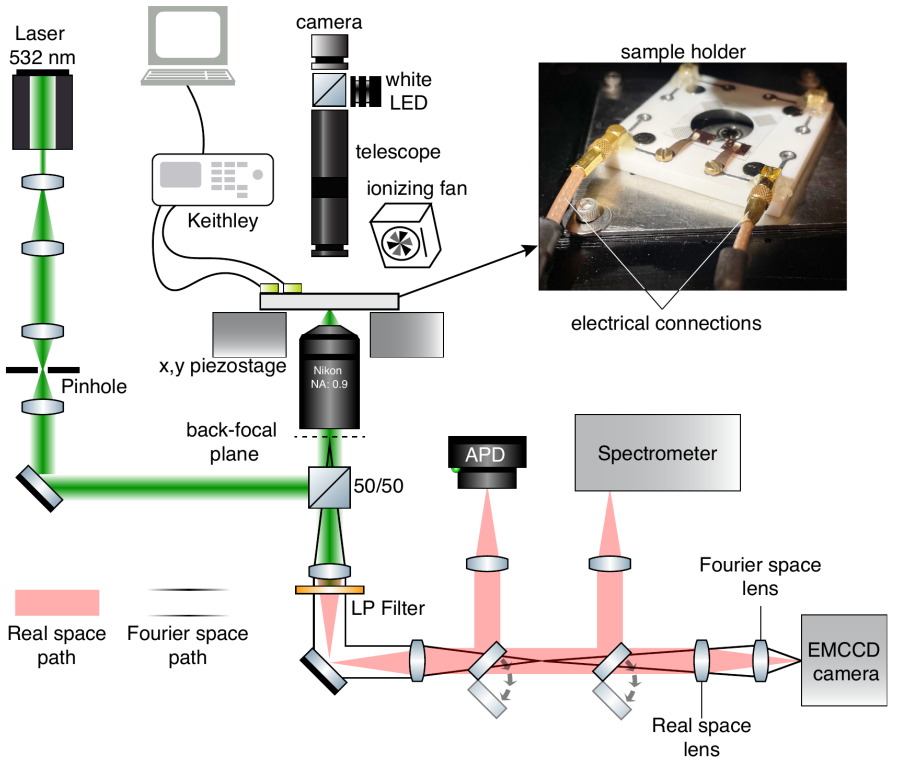

Figure A.5: Illustration of the optoelectronics measurement setup.

of an Andor iXon Ultra EMCCD camera. Changing between imaging real and Fourier space is done by switching the corresponding lenses in Fig. A.5.

The low-temperature measurements are performed in a variable temperature probe station. Currents are measured using a Femto DDPCA- 300 current amplifier. An ADwin Pro II DAC is used to apply the bias voltage and read the output voltage of the current amplifier.

B

SI: TMD-coupled tunnel junctions

Exciton generation in both polarities

As discussed in Ch. 5 the exciton generation process occurs for both bias polarities. Figure B.1 shows spectra for both polarities where the narrow emission at exciton wavelengths is observed in both. This observation further supports the argument that excitons are not created by charge injection as such a process would be polarity dependent.

TMD coupled device with 5 nm spacer hBN

In Fig. 5.5 we presented the excitonic emission normalized by the PL efficiency as a function of the thickness of the hBN layer between TMD and graphene (s-hBN). We use results from different devices with different s-hBN thicknesses (d_s). Here we present results for a device with d_s=5 nm as illustrated in Fig. B.2. On that device there are two regions, with and without WSe_2. In Figs. B.2b,c we display emitted spectra for both regions where we can observe that even with a thick 5 nm s-hBN we observe an increase in emission at excitonic wavelengths.

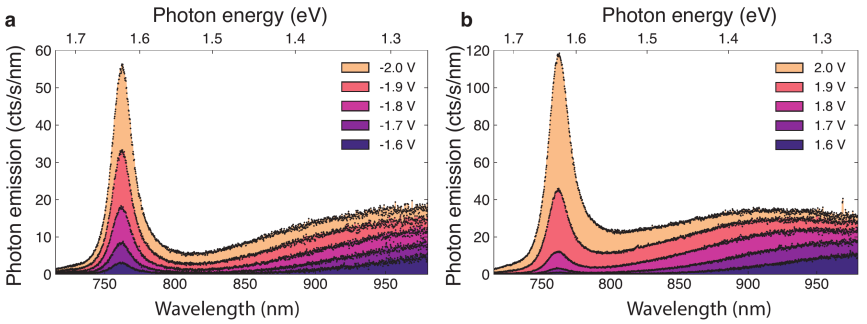

Figure B.1: Spectral symmetry with bias voltage. (a,b) Photon emission spectra from the WSe_2-coupled tunnel junction presented in Fig. 5.2 for (a) positive bias voltage and (b) negative bias voltage. Similar spectral characteristics are observed.

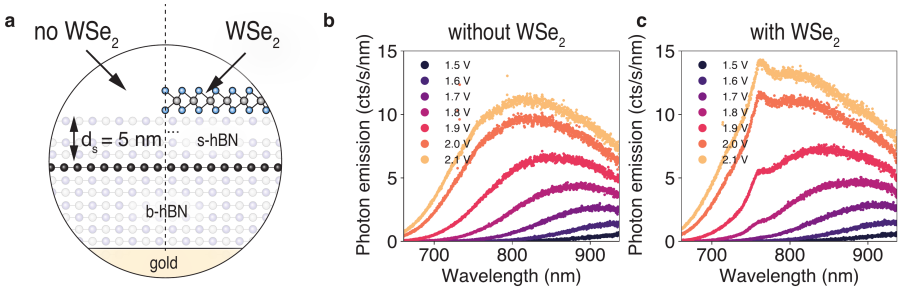

Figure B.2: TMD-coupled device with 5 nm spacer hBN. (a) Device schematic. The WSe_2 is separated from the tunneling junction by a spacer hBN with 5 nm thickness. The WSe_2 flake is stacked on top in a way that two areas are formed: with and without WSe_2. (b,c) Photon emission spectra from the two areas (b) without WSe_2 and (c) with WSe_2. A small contribution in excitonic wavelengths is still observed even though the WSe_2 flake is 5 nm away from the tunnel junction.

C

SI: Monolayer MoS_2 memristors

C.1 I-V measurements

In Ch. 7 all fabricated devices were electrically characterized by applying pulsed voltage sweeps. The hysteretic effect observed in the I-V characteristics is attributed to a non-volatile memory behavior. The devices with increased defect density in MoS_2 show a more pronounced hysteretic behavior in I-V measurements as it is shown in Fig. C.1 where all the presented measurements have been acquired with the same electrical excitation with a $V_{\text{peak}} = 4\,\text{V}$. In the case of pristine MoS_2 there is no hysteresis observed in such low voltages.

C.2 Resistance model as a function of defect density

The electron transport simulations can only provide values of resistance for a limited defect density range due to the increasing size of the cell in the case of low defect densities below $0.1\,\text{nm}^{-2}$. For that reason we form a classical model of resistance evaluation as a function of defect density in order to be able to extrapolate values for a bigger range of defect densities using the estimations of the numerical simulations. Let us assume a crystal area with pristine and defective domains as it is illustrated in Fig. C.2a. The sub-domains indicated by

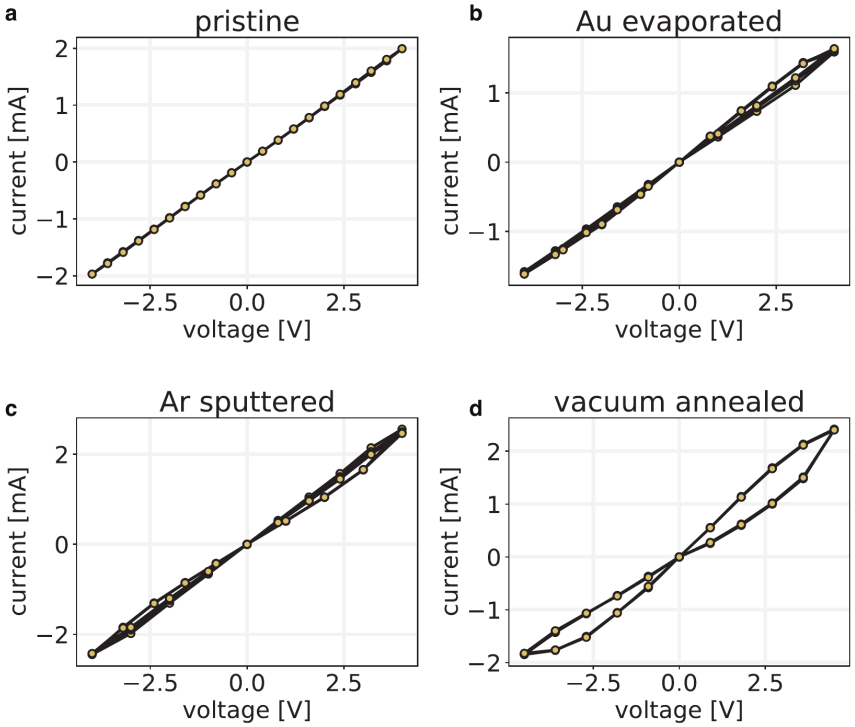

Figure C.1: (a-d) I-V measurements recorded for the same peak voltage (4V) for memristive devices with differently treated 1L MoS_2 flakes.

dashed lines refer to a cell area A equal to the one used in the simulations. We assume a number of total cells N and a number of defective cells n. Assuming a parallel conductance model the total overall conductance of such a crystal area is given by:

$$G_N = G_{pr}(N - n) + G_d \cdot n \tag{C.1}$$

where G_N is the total conductance for all the N cells, G_{pr} is the cell conductance of a pristine cell and G_d is the cell conductance of a defective cell. G_d can either refer to the conductance of the case of one V_s or a V_s substituted by an Au atom as illustrated in Fig. 7.6. By defining the defect density as

$$\rho_d = \frac{n}{N \cdot A} \tag{C.2}$$

we can arrive to an expression that describes the conductance for arbitrary defect densities of a cell with area A.

$$G(\rho_d) = G_{pr} + \left(G_d - G_{pr}\right)\rho_d \cdot A \tag{C.3}$$

This equation is then fitted to the simulation results for obtaining the values of G_{pr} and G_d. The result for both cases, V_s and Au-substituted V_s and their corresponding conductance G_{V_s} and G_{Au} as a function of defect density ρ_d is shown in Fig. C.2b. Written in resistances equation C.3 can be written as

$$R\left(\rho_d\right) = \frac{R_{pr} \cdot R_d}{R_d + \left(R_{pr} - R_d\right)\rho_d \cdot A} \tag{C.4}$$

where $R_d = 1/G_d$ and $R_{pr} = 1/G_{pr}$.

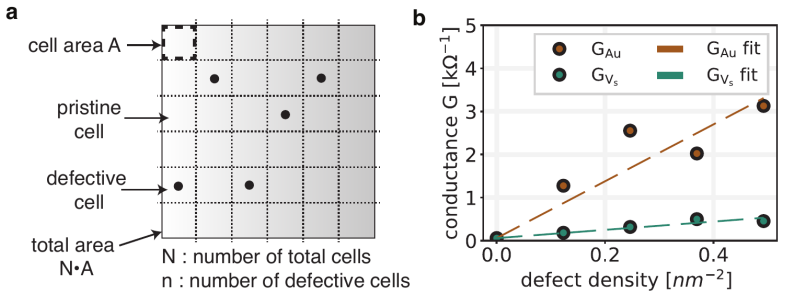

Figure C.2: (a) Illustration of the model assumed for calculating the total resistance of a crystal area $N \cdot A$ divided in N cells of area A with n number of cells having one defect. (b) Simulation results (dots) and fit of the presented model (dashed lines) of the conductance for different defect densities.

References

[1] H. Ritchie, M. Roser, and P. Rosado, *Energy*, Our World in Data (2022), https://ourworldindata.org/energy.

[2] M. M. Waldrop, *The chips are down for Moore's law*, Nature **530**, 144 (2016).

[3] C. D. Schuman, S. R. Kulkarni, M. Parsa, J. P. Mitchell, P. Date, and B. Kay, *Opportunities for neuromorphic computing algorithms and applications*, Nature Computational Science **2**, 10 (2022).

[4] N. L. Kazanskiy, M. A. Butt, and S. N. Khonina, *Optical Computing: Status and Perspectives*, Nanomaterials **12** (2022).

[5] K. S. Novoselov, A. K. Geim, S. V. Morozov, D. Jiang, Y. Zhang, S. V. Dubonos, I. V. Grigorieva, and A. A. Firsov, *Electric Field Effect in Atomically Thin Carbon Films*, Science **306**, 666 (2004).

[6] A. R. Urade, I. Lahiri, and K. S. Suresh, *Graphene Properties, Synthesis and Applications: A Review*, Jom (2022).

[7] R. R. Nair, P. Blake, A. N. Grigorenko, K. S. Novoselov, T. J. Booth, T. Stauber, N. M. Peres, and A. K. Geim, *Fine structure constant defines visual transparency of graphene*, Science **320**, 1308 (2008).

[8] K. Watanabe, T. Taniguchi, and H. Kanda, *Direct-bandgap properties and evidence for ultraviolet lasing of hexagonal boron nitride single crystal*, Nature Materials **3**, 404 (2004).

[9] C. R. Dean, A. F. Young, I. Meric, C. Lee, L. Wang, S. Sorgenfrei, K. Watanabe, T. Taniguchi, P. Kim, K. L. Shepard, and J. Hone, *Boron nitride substrates for high-quality graphene electronics*, Nature Nanotechnology **5**, 722 (2010).

[10] G. Cassabois, P. Valvin, and B. Gil, *Hexagonal boron nitride is an indirect bandgap semiconductor*, Nature Photonics **10**, 262 (2016).

[11] C. Elias, P. Valvin, T. Pelini, A. Summerfield, C. J. Mellor, T. S. Cheng, L. Eaves, C. T. Foxon, P. H. Beton, S. V. Novikov, B. Gil, and G. Cassabois, *Direct band-gap crossover in epitaxial monolayer boron nitride*, Nature Communications **10**, 1 (2019).

[12] L. Wang, I. Meric, P. Y. Huang, Q. Gao, Y. Gao, H. Tran, T. Taniguchi, K. Watanabe, L. M. Campos, D. A. Muller, J. Guo, P. Kim, J. Hone, K. L. Shepard, and C. R. Dean, *One-Dimensional Electrical Contact to a Two-Dimensional Material*, Science **342**, 614 (2013).

[13] F. Withers, O. Del Pozo-Zamudio, A. Mishchenko, A. P. Rooney, A. Gholinia, K. Watanabe, T. Taniguchi, S. J. Haigh, A. K. Geim, A. I. Tartakovskii, and K. S. Novoselov, *Light-emitting diodes by band-structure engineering in van der Waals heterostructures*, Nature Materials **14**, 301 (2015).

[14] S. Kim, J. E. Fröch, J. Christian, M. Straw, J. Bishop, D. Totonjian, K. Watanabe, T. Taniguchi, M. Toth, and I. Aharonovich, *Photonic crystal cavities from hexagonal boron nitride*, Nature Communications **9**, 1 (2018).

[15] R. Khelifa, P. Back, N. Flöry, S. Nashashibi, K. Malchow, T. Taniguchi, K. Watanabe, A. Jain, and L. Novotny, *Coupling Interlayer Excitons to Whispering Gallery Modes in van der Waals Heterostructures*, Nano Letters **20**, 6155 (2020).

[16] K. F. Mak, C. Lee, J. Hone, J. Shan, and T. F. Heinz, *Atomically thin MoS2: A new direct-gap semiconductor*, Physical Review Letters **105**, 2 (2010).

[17] A. Chernikov, T. C. Berkelbach, H. M. Hill, A. Rigosi, Y. Li, O. B. Aslan, D. R. Reichman, M. S. Hybertsen, and T. F. Heinz, *Exciton binding energy and nonhydrogenic Rydberg series in monolayer WS2*, Physical Review Letters **113** (2014).

[18] T. Mueller and E. Malic, *Exciton physics and device application of two-dimensional transition metal dichalcogenide semiconductors*, npj 2D Materials and Applications **2**, 1 (2018).

[19] D. Kozawa, R. Kumar, A. Carvalho, K. Kumar Amara, W. Zhao, S. Wang, M. Toh, R. M. Ribeiro, A. H. Castro Neto, K. Matsuda, and G. Eda, *Photocarrier relaxation pathway in two-dimensional semiconducting transition metal dichalcogenides*, Nature Communications **5**, 1 (2014).

[20] N. Alidoust, G. Bian, S. Y. Xu, R. Sankar, M. Neupane, C. Liu, I. Belopolski, D. X. Qu, J. D. Denlinger, F. C. Chou, and M. Z. Hasan, *Observation of monolayer valence band spin-orbit effect and induced quantum well states in MOX2*, Nature Communications **5** (2014).

[21] Y. C. Cheng, Z. Y. Zhu, M. Tahir, and U. Schwingenschlögl, *Spin-orbit-induced spin splittings in polar transition metal dichalcogenide monolayers*, Epl **102**

(2013).

[22] G. H. Jung, S. J. Yoo, and Q. H. Park, *Measuring the optical permittivity of twodimensional materials without a priori knowledge of electronic transitions*, Nanophotonics **8**, 263 (2018).

[23] M. Amani, D. H. Lien, D. Kiriya, J. Xiao, A. Azcatl, J. Noh, S. R. Madhvapathy, R. Addou, K. C. Santosh, M. Dubey, K. Cho, R. M. Wallace, S. C. Lee, J. H. He, J. W. Ager, X. Zhang, E. Yablonovitch, and A. Javey, *Near-unity photoluminescence quantum yield in MoS2*, Science **350**, 1065 (2015).

[24] D. H. Lien, S. Z. Uddin, M. Yeh, M. Amani, H. Kim, J. W. Ager, E. Yablonovitch, and A. Javey, *Electrical suppression of all nonradiative recombination pathways in monolayer semiconductors*, Science **471**, 468 (2019).

[25] H. Kim, S. Z. Uddin, N. Higashitarumizu, E. Rabani, and A. Javey, *Inhibited nonradiative decay at all exciton densities in monolayer semiconductors*, Science **373**, 448 (2021).

[26] F. Bussolotti, J. Yang, H. Kawai, C. P. Y. Wong, and K. E. J. Goh, *Impact of S-Vacancies on the Charge Injection Barrier at the Electrical Contact with the MoS 2 Monolayer* , ACS Nano **15**, 2686 (2021).

[27] Q. Ma, P. M. Odenthal, J. Mann, D. Le, C. S. Wang, Y. Zhu, T. Chen, D. Sun, K. Yamaguchi, T. Tran, M. Wurch, J. L. McKinley, J. Wyrick, K. Magnone, T. F. Heinz, T. S. Rahman, R. Kawakami, and L. Bartels, *Controlled argon beam-induced desulfurization of monolayer molybdenum disulfide*, Journal of Physics: Condensed Matter **25**, 252201 (2013).

[28] S. M. Hus, R. Ge, P. A. Chen, L. Liang, G. E. Donnelly, W. Ko, F. Huang, M. H. Chiang, A. P. Li, and D. Akinwande, *Observation of single-defect memristor in an MoS2 atomic sheet*, Nature Nanotechnology (2020).

[29] S. Tongay, J. Suh, C. Ataca, W. Fan, A. Luce, J. S. Kang, J. Liu, C. Ko, R. Raghunathanan, J. Zhou, F. Ogletree, J. Li, J. C. Grossman, and J. Wu, *Defects activated photoluminescence in two-dimensional semiconductors: interplay between bound, charged, and free excitons*, Scientific Reports **3**, 2657 (2013).

[30] A. Jain, P. Bharadwaj, S. Heeg, M. Parzefall, T. Taniguchi, K. Watanabe, and L. Novotny, *Minimizing residues and strain in 2D materials transferred from PDMS*, Nanotechnology **29**, 265203 (2018).

[31] S. Bae, N. Sugiyama, T. Matsuo, H. Raebiger, K. I. Shudo, and K. Ohno, *Defect-Induced Vibration Modes of Ar+ -Irradiated MoS2*, Physical Review Applied **7**, 1 (2017).

[32] G. Froehlicher, E. Lorchat, and S. Berciaud, *Charge Versus Energy Transfer in Atomically Thin Graphene-Transition Metal Dichalcogenide van der Waals Heterostructures*, Physical Review X **8**, 1 (2018).

[33] E. Lorchat, L. E. P. López, C. Robert, D. Lagarde, G. Froehlicher, T. Taniguchi, K. Watanabe, X. Marie, and S. Berciaud, *Filtering the photoluminescence spectra of atomically thin semiconductors with graphene*, Nature Nanotechnology **15**, 283 (2020).

[34] T. Förster, *Zwischenmolekulare Energiewanderung und Fluoreszenz*, Annalen der Physik **437**, 55 (1948).

[35] T. Förster, *Delocalized Excitation and Excitation Transfer. Bulletin No. 18*, Technical report, Florida State Univ., Tallahassee. Dept. of Chemistry, 1964.

[36] L. Novotny and B. Hecht, *Principles of nano-optics*, Cambridge university press, 2012.

[37] S. Weiss, *Fluorescence spectroscopy of single biomolecules*, Science **283**, 1676 (1999).

[38] R. E. Dale and J. Eisinger, *Intramolecular energy transfer and molecular conformation*, Proceedings of the National Academy of Sciences of the United States of America **73**, 271 (1976).

[39] C. R. Kagan, C. B. Murray, M. Nirmal, and M. G. Bawendi, *Electronic energy transfer in CdSe Quantum dot solids*, Physical Review Letters **76**, 1517 (1996).

[40] H. Van Amerongen et al., *Photosynthetic excitons*, World Scientific, 2000.

[41] M. Achermann, M. A. Petruska, D. D. Koleske, M. H. Crawford, and V. I. Klimov, *Nanocrystal-based light-emitting diodes utilizing high-efficiency nonradiative energy transfer for color conversion*, Nano Letters **6**, 1396 (2006).

[42] S. Pimputkar, J. S. Speck, S. P. Denbaars, and S. Nakamura, *Prospects for LED lighting*, Nature Photonics **3**, 180 (2009).

[43] T. T. Tran, K. Bray, M. J. Ford, M. Toth, and I. Aharonovich, *Quantum emission from hexagonal boron nitride monolayers*, Nature Nanotechnology **11**, 37 (2016).

[44] T. T. Tran, C. Zachreson, A. M. Berhane, K. Bray, R. G. Sandstrom, L. H. Li, T. Taniguchi, K. Watanabe, I. Aharonovich, and M. Toth, *Quantum Emission from Defects in Single-Crystalline Hexagonal Boron Nitride*, Physical Review Applied **5**, 2 (2016).

[45] C. Ferrante, G. Di Battista, L. E. López, G. Batignani, E. Lorchat, A. Virga, S. Berciaud, and T. Scopigno, *Picosecond energy transfer in a transition metal dichalcogenide-graphene heterostructure revealed by transient Raman spectroscopy*, Proceedings of the National Academy of Sciences of the United States of America **119**, 1 (2022).

[46] A. Raja, A. Chaves, J. Yu, G. Arefe, H. M. Hill, A. F. Rigosi, T. C. Berkelbach, P. Nagler, C. Schüller, T. Korn, C. Nuckolls, J. Hone, L. E. Brus, T. F. Heinz, D. R. Reichman, and A. Chernikov, *Coulomb engineering of the bandgap and*

excitons in two-dimensional materials, Nature Communications **8**, 1 (2017).

[47] M. Parzefall, P. Bharadwaj, and L. Novotny, *Antenna-coupled tunnel junctions*, in *Quantum plasmonics*, pages 211–236, Springer, 2017.

[48] J. Bardeen, *Tunnelling from a Many-Particle Point of View*, Phys. Rev. Lett. **6**, 57 (1961).

[49] M. Parzefall and L. Novotny, *Light at the End of the Tunnel*, ACS Photonics **5**, 4195 (2018).

[50] G. Ford and W. Weber, *Electromagnetic interactions of molecules with metal surfaces*, Physics Reports **113**, 195 (1984).

[51] M. Parzefall, P. Bharadwaj, A. Jain, T. Taniguchi, K. Watanabe, and L. Novotny, *Antenna-coupled photon emission from hexagonal boron nitride tunnel junctions*, Nature nanotechnology **10**, 1058 (2015).

[52] H. Qian, S. W. Hsu, K. Gurunatha, C. T. Riley, J. Zhao, D. Lu, A. R. Tao, and Z. Liu, *Efficient light generation from enhanced inelastic electron tunnelling*, Nature Photonics **12**, 485 (2018).

[53] J. Kern, R. Kullock, J. Prangsma, M. Emmerling, M. Kamp, and B. Hecht, *Electrically driven optical antennas*, Nature Photonics **9**, 582 (2015).

[54] S. de Vega and F. J. García de Abajo, *Plasmon generation through electron tunneling in twisted double-layer graphene and metal-insulator-graphene systems*, Phys. Rev. B **99**, 115438 (2019).

[55] Y. Zhang, V. W. Brar, F. Wang, C. Girit, Y. Yayon, M. Panlasigui, A. Zettl, and M. F. Crommie, *Giant phonon-induced conductance in scanning tunnelling spectroscopy of gate-tunable graphene*, Nature Physics **4**, 627 (2008).

[56] M. Parzefall, Á. Szabó, T. Taniguchi, K. Watanabe, M. Luisier, and L. Novotny, *Light from van der Waals quantum tunneling devices*, Nature communications **10**, 1 (2019).

[57] M. Goryca, J. Li, A. V. Stier, T. Taniguchi, K. Watanabe, E. Courtade, S. Shree, C. Robert, B. Urbaszek, X. Marie, and S. A. Crooker, *Revealing exciton masses and dielectric properties of monolayer semiconductors with high magnetic fields*, Nature Communications **10**, 4172 (2019).

[58] J. Binder, F. Withers, M. R. Molas, C. Faugeras, K. Nogajewski, K. Watanabe, T. Taniguchi, A. Kozikov, A. K. Geim, K. S. Novoselov, and M. Potemski, *Sub-bandgap Voltage Electroluminescence and Magneto-oscillations in a WSe2 Light-Emitting van der Waals Heterostructure*, Nano Letters **17**, 1425 (2017).

[59] H. Cao, G. Klimovitch, G. Björk, and Y. Yamamoto, *Direct creation of quantum well excitons by electron resonant tunneling*, Physical review letters **75**, 1146 (1995).

[60] S. S. Baik, S. Im, and H. J. Choi, *Work Function Tuning in Two-Dimensional*

MoS 2 Field-Effect-Transistors with Graphene and Titanium Source-Drain Contacts, Scientific Reports **7**, 1 (2017).

[61] R. L. Olmon, B. Slovick, T. W. Johnson, D. Shelton, S.-H. Oh, G. D. Boreman, and M. B. Raschke, *Optical dielectric function of gold*, Phys. Rev. B **86**, 235147 (2012).

[62] C. Manolatou, H. Wang, W. Chan, S. Tiwari, and F. Rana, *Radiative and nonradiative exciton energy transfer in monolayers of two-dimensional group-VI transition metal dichalcogenides*, Physical Review B **93** (2016).

[63] S. K. Lyo, *Energy transfer of excitons between quantum wells separated by a wide barrier*, Physical Review B - Condensed Matter and Materials Physics **62**, 13641 (2000).

[64] D. L. Andrews and D. S. Bradshaw, *Virtual photons, dipole fields and energy transfer: a quantum electrodynamical approach*, European Journal of Physics **25**, 845 (2004).

[65] P. Anger, P. Bharadwaj, and L. Novotny, *Enhancement and Quenching of Single-Molecule Fluorescence*, Phys. Rev. Lett. **96**, 113002 (2006).

[66] C. Hsu, R. Frisenda, R. Schmidt, A. Arora, S. M. de Vasconcellos, R. Bratschitsch, H. S. van der Zant, and A. Castellanos-Gomez, *Thickness-Dependent Refractive Index of 1L, 2L, and 3L MoS2, MoSe2, WS2, and WSe2*, Advanced Optical Materials **7** (2019).

[67] A. Raja, . Andres, A. Montoya, . Castillo, J. Zultak, X.-X. Zhang, Z. Ye, C. Roquelet, D. A. Chenet, A. M. V. D. Zande, P. Huang, S. Jockusch, J. Hone, D. R. Reichman, L. E. Brus, and T. F. Heinz, *Energy Transfer from Quantum Dots to Graphene and MoS 2 : The Role of Absorption and Screening in Two-Dimensional Materials*, Nano Lett **16** (2016).

[68] F. Prins, A. J. Goodman, and W. A. Tisdale, *Reduced dielectric screening and enhanced energy transfer in single- and few-layer MoS2*, Nano Letters **14**, 6087 (2014).

[69] A. Splendiani, L. Sun, Y. Zhang, T. Li, J. Kim, C. Y. Chim, G. Galli, and F. Wang, *Emerging photoluminescence in monolayer MoS2*, Nano Letters **10**, 1271 (2010).

[70] M. Paur, A. J. Molina-Mendoza, R. Bratschitsch, K. Watanabe, T. Taniguchi, and T. Mueller, *Electroluminescence from multi-particle exciton complexes in transition metal dichalcogenide semiconductors*, Nature Communications **10**, 1 (2019).

[71] R. J. Peña Román, Y. Auad, L. Grasso, F. Alvarez, I. D. Barcelos, and L. F. Zagonel, *Tunneling-current-induced local excitonic luminescence in p-doped WSe2monolayers*, Nanoscale **12**, 13460 (2020).

[72] C. Palacios-Berraquero, M. Barbone, D. M. Kara, X. Chen, I. Goykhman, D. Yoon, A. K. Ott, J. Beitner, K. Watanabe, T. Taniguchi, A. C. Ferrari, and M. Atatüre, *Atomically thin quantum light-emitting diodes*, Nature Communications **7**, 1 (2016).

[73] L. A. Jauregui, A. Y. Joe, K. Pistunova, D. S. Wild, A. A. High, Y. Zhou, G. Scuri, K. de Greve, A. Sushko, C. H. Yu, T. Taniguchi, K. Watanabe, D. J. Needleman, M. D. Lukin, H. Park, and P. Kim, *Electrical control of interlayer exciton dynamics in atomically thin heterostructures*, Science **366**, 870 (2019).

[74] R. S. Sundaram, M. Engel, A. Lombardo, R. Krupke, A. C. Ferrari, P. Avouris, and M. Steiner, *Electroluminescence in Single Layer MoS2*, Nano Letters **13**, 1416 (2013).

[75] J. S. Ross, P. Klement, A. M. Jones, N. J. Ghimire, J. Yan, D. G. Mandrus, T. Taniguchi, K. Watanabe, K. Kitamura, W. Yao, D. H. Cobden, and X. Xu, *Electrically tunable excitonic light-emitting diodes based on monolayer WSe2 p-n junctions*, Nature Nanotechnology **9**, 268 (2014).

[76] S. Z. Uddin, N. Higashitarumizu, H. Kim, I. K. M. R. Rahman, and A. Javey, *Efficiency Roll-Off Free Electroluminescence from Monolayer WSe 2* , Nano Letters (2022).

[77] F. Withers, O. Del Pozo-Zamudio, S. Schwarz, S. Dufferwiel, P. M. Walker, T. Godde, A. P. Rooney, A. Gholinia, C. R. Woods, P. Blake, S. J. Haigh, K. Watanabe, T. Taniguchi, I. L. Aleiner, A. K. Geim, V. I. Fal'Ko, A. I. Tartakovskii, and K. S. Novoselov, *WSe2 Light-Emitting Tunneling Transistors with Enhanced Brightness at Room Temperature*, Nano Letters **15**, 8223 (2015).

[78] Q. Fu, Z. Hu, M. Zhou, J. Lu, and Z. Ni, *Excitonic Emission in Atomically Thin Electroluminescent Devices*, Laser and Photonics Reviews **2000587**, 1 (2021).

[79] J. Binder, J. Howarth, F. Withers, M. R. Molas, T. Taniguchi, K. Watanabe, C. Faugeras, A. Wysmolek, M. Danovich, V. I. Fal'ko, A. K. Geim, K. S. Novoselov, M. Potemski, and A. Kozikov, *Upconverted electroluminescence via Auger scattering of interlayer excitons in van der Waals heterostructures*, Nature Communications **10**, 1 (2019).

[80] G. Clark, J. R. Schaibley, J. Ross, T. Taniguchi, K. Watanabe, J. R. Hendrickson, S. Mou, W. Yao, and X. Xu, *Single defect light-emitting diode in a van der Waals heterostructure*, Nano letters **16**, 3944 (2016).

[81] L. E. P. López, A. Rosławska, F. Scheurer, S. Berciaud, and G. Schull, *Tip-induced excitonic luminescence nanoscopy of an atomically-resolved van der Waals heterostructure*, page 1 (2022).

[82] R. J. P. Román, D. Pommier, R. Bretel, L. E. P. López, E. Lorchat, J. Chaste, A. Ouerghi, S. L. Moal, E. Boer-Duchemin, G. Dujardin, A. G. Borisov, L. F.

Zagonel, G. Schull, S. Berciaud, and E. L. Moal, *Electroluminescence of monolayer WS_2 in a scanning tunneling microscope: the effect of bias polarity on the spectral and angular distribution of the emitted light*, (2022).

[83] J. Feng, Y. Li, J. Zhang, Y. Tang, H. Sun, L. Gan, and C. Z. Ning, *Injection-free multiwavelength electroluminescence devices based on monolayer semiconductors driven by an alternating field*, Science Advances **8**, 1 (2022).

[84] J. A. Schuller, S. Karav eli, T. Schiros, K. He, S. Yang, I. Kymissis, J. Shan, and R. Zia, *Orientation of luminescent excitons in layered nanomaterials*, Nature nanotechnology **8**, 271 (2013).

[85] B. Song, H. Gu, S. Zhu, H. Jiang, X. Chen, C. Zhang, and S. Liu, *Broadband optical properties of graphene and HOPG investigated by spectroscopic Mueller matrix ellipsometry*, Applied Surface Science **439**, 1079 (2018).

[86] S. Y. Lee, T. Y. Jeong, S. Jung, and K. J. Yee, *Refractive Index Dispersion of Hexagonal Boron Nitride in the Visible and Near-Infrared*, Physica Status Solidi (B) Basic Research **256**, 1 (2019).

[87] A. Karmakar, A. Al-Mahboob, C. E. Petoukhoff, O. Kravchyna, N. S. Chan, T. Taniguchi, K. Watanabe, and K. M. Dani, *Dominating Interlayer Resonant Energy Transfer in Type-II 2D Heterostructure*, ACS Nano **16**, 3861 (2022).

[88] I. Medintz and N. Hildebrandt, *FRET - Foerster Resonance Energy Transfer - From Theory to Applications*, Wiley-VCH, 2013.

[89] G.-H. Lee, Y.-J. Yu, C. Lee, C. Dean, K. L. Shepard, P. Kim, and J. Hone, *Electron tunneling through atomically flat and ultrathin hexagonal boron nitride*, Appl. Phys. Lett. **99**, 243114 (2011).

[90] G. Wang, A. Chernikov, M. M. Glazov, T. F. Heinz, X. Marie, T. Amand, and B. Urbaszek, *Colloquium: Excitons in atomically thin transition metal dichalcogenides*, Rev. Mod. Phys. **90**, 021001 (2018).

[91] Y. Luo, W. Wu, P. Lyu, F. Huang, S. Zeng, J. Ke, and al, *Orbital, spin and valley contributions to Zeeman splitting of excitonic resonances in MoSe 2 , WSe 2 and WS 2 Monolayers You may also like Single Information Extraction Algorithm of Mechanical Equipment Usage Information Recording Based on Deep Learning Quantitative Analysis in Nuclear Medicine Imaging John Fleming-A Video Description Model with Improved Attention Mechanism This content was downloaded from IP address*, (2018).

[92] A. T. Hanbicki, M. Currie, G. Kioseoglou, A. L. Friedman, and B. T. Jonker, *Measurement of high exciton binding energy in the monolayer transition-metal dichalcogenides WS2 and WSe2*, Solid State Communications **203**, 16 (2015).

[93] J. Jadczak, J. Kutrowska-Girzycka, P. Kapuściński, Y. S. Huang, A. Wójs, and L. Bryja, *Probing of free and localized excitons and trions in atomically thin*

WSe2, WS2, MoSe2 and MoS2 in photoluminescence and reflectivity experiments, Nanotechnology **28** (2017).

[94] T. Y. Jeong, H. Kim, S. J. Choi, K. Watanabe, T. Taniguchi, K. J. Yee, Y. S. Kim, and S. Jung, *Spectroscopic studies of atomic defects and bandgap renormalization in semiconducting monolayer transition metal dichalcogenides*, Nature Communications **10** (2019).

[95] C. Zhang, Y. Chen, A. Johnson, M. Y. Li, L. J. Li, P. C. Mende, R. M. Feenstra, and C. K. Shih, *Probing Critical Point Energies of Transition Metal Dichalcogenides: Surprising Indirect Gap of Single Layer WSe2*, Nano Letters **15**, 6494 (2015).

[96] A. Kormányos, G. Burkard, M. Gmitra, J. Fabian, V. Zólyomi, N. D. Drummond, and V. Fal'ko, *$K \cdot P$ Theory for Two-Dimensional Transition Metal Dichalcogenide Semiconductors* , 2D Materials **2**, 022001 (2015).

[97] M. Parzefall and L. Novotny, *Optical antennas driven by quantum tunneling: a key issues review*, Reports on Progress in Physics **82**, 112401 (2019).

[98] Editorial, *Testing memory downsizing limits*, Nature Nanotechnology **14**, 1 (2019).

[99] T. Hasegawa, K. Terabe, T. Tsuruoka, and M. Aono, *Atomic switch: Atom/ion movement controlled devices for beyond von-Neumann computers*, Advanced Materials **24**, 252 (2012).

[100] D. S. Jeong and C. S. Hwang, *Nonvolatile Memory Materials for Neuromorphic Intelligent Machines*, Advanced Materials **30**, 1704729 (2018).

[101] L. Chua, *Memristor-The missing circuit element*, IEEE Transactions on Circuit Theory **18**, 507 (1971).

[102] D. B. Strukov, G. S. Snider, D. R. Stewart, and R. S. Williams, *The missing memristor found*, Nature **453**, 80 (2008).

[103] R. Waser, R. Dittmann, C. Staikov, and K. Szot, *Redox-based resistive switching memories nanoionic mechanisms, prospects, and challenges*, Advanced Materials **21**, 2632 (2009).

[104] H. S. Wong, H. Y. Lee, S. Yu, Y. S. Chen, Y. Wu, P. S. Chen, B. Lee, F. T. Chen, and M. J. Tsai, *Metal-oxide RRAM*, Proceedings of the IEEE **100**, 1951 (2012).

[105] H.-S. Wong, S. Raoux, S. Kim, J. Liang, J. Reifenberg, B. Rajendran, M. Asheghi, and K. Goodson, *Phase change memory*, Proceedings of the IEEE **98**, 2201 (2010).

[106] A. Emboras, A. Alabastri, F. Ducry, B. Cheng, Y. Salamin, P. Ma, S. Andermatt, B. Baeuerle, A. Josten, C. Hafner, M. Luisier, P. Nordlander, and J. Leuthold, *Atomic Scale Photodetection Enabled by a Memristive Junction*, ACS Nano **12**, 6706 (2018).

[107] W. Sun, B. Gao, M. Chi, Q. Xia, J. J. Yang, H. Qian, and H. Wu, *Understanding memristive switching via in situ characterization and device modeling*, Nature Communications **10**, 1 (2019).

[108] S. Pi, C. Li, H. Jiang, W. Xia, H. Xin, J. J. Yang, and Q. Xia, *Memristor crossbar arrays with 6-nm half-pitch and 2-nm critical dimension*, Nature Nanotechnology **14**, 35 (2019).

[109] Q. Zhao, Z. Xie, Y. P. Peng, K. Wang, H. Wang, X. Li, H. Wang, J. Chen, H. Zhang, and X. Yan, *Current status and prospects of memristors based on novel 2D materials*, Materials Horizons **7**, 1495 (2020).

[110] F. Zhang, H. Zhang, S. Krylyuk, C. A. Milligan, Y. Zhu, D. Y. Zemlyanov, L. A. Bendersky, B. P. Burton, A. V. Davydov, and J. Appenzeller, *Electric-field induced structural transition in vertical $MoTe_2$ and $Mo_{1-x}W_xTe_2$ - based resistive memories*, Nature Materials **18**, 55 (2019).

[111] P. Cheng, K. Sun, and Y. H. Hu, *Memristive Behavior and Ideal Memristor of 1T Phase MoS_2 Nanosheets*, Nano Letters **16**, 572 (2016).

[112] Y. Wang, J. Xiao, H. Zhu, Y. Li, Y. Alsaid, K. Y. Fong, Y. Zhou, S. Wang, W. Shi, Y. Wang, A. Zettl, E. J. Reed, and X. Zhang, *Structural phase transition in monolayer $MoTe_2$ driven by electrostatic doping*, Nature **550**, 487 (2017).

[113] X. Wu, R. Ge, P. A. Chen, H. Chou, Z. Zhang, Y. Zhang, S. Banerjee, M. H. Chiang, J. C. Lee, and D. Akinwande, *Thinnest Nonvolatile Memory Based on Monolayer h-BN*, Advanced Materials **31**, 1806790 (2019).

[114] H. K. He, R. Yang, W. Zhou, H. M. Huang, J. Xiong, L. Gan, T. Y. Zhai, and X. Guo, *Photonic Potentiation and Electric Habituation in Ultrathin Memristive Synapses Based on Monolayer MoS2*, Small **14**, 1 (2018).

[115] R. Ge, X. Wu, M. Kim, J. Shi, S. Sonde, L. Tao, Y. Zhang, J. C. Lee, and D. Akinwande, *Atomristor: Nonvolatile Resistance Switching in Atomic Sheets of Transition Metal Dichalcogenides*, Nano Letters **18**, 434 (2018).

[116] A. Krishnaprasad, N. Choudhary, S. Das, D. Dev, H. Kalita, H.-S. Chung, O. Aina, Y. Jung, and T. Roy, *Electronic synapses with near-linear weight update using MoS 2 /graphene memristors* , Applied Physics Letters **115**, 103104 (2019).

[117] D. Akinwande, *Memory, memristors, and atomristors*, IEEE Micro **38**, 50 (2018).

[118] S. Bhattacharjee, E. Caruso, N. McEvoy, C. Ó Coileáin, K. O'Neill, L. Ansari, G. S. Duesberg, R. Nagle, K. Cherkaoui, F. Gity, and P. K. Hurley, *Insights into Multilevel Resistive Switching in Monolayer MoS2*, ACS Applied Materials and Interfaces **12**, 6022 (2020).

[119] I. M. Datye, M. M. Rojo, E. Yalon, S. Deshmukh, M. J. Mleczko, and E. Pop,

Localized Heating and Switching in MoTe 2 -Based Resistive Memory Devices , Nano Letters , 1461 (2020).

[120] P. J. Zomer, M. H. Guimarães, J. C. Brant, N. Tombros, and B. J. Van Wees, *Fast pick up technique for high quality heterostructures of bilayer graphene and hexagonal boron nitride*, Applied Physics Letters **105**, 013101 (2014).

[121] Y. Liu, J. Guo, E. Zhu, L. Liao, S.-J. Lee, M. Ding, I. Shakir, V. Gambin, Y. Huang, and X. Duan, *Approaching the Schottky-Mott limit in van der Waals metal-semiconductor junctions*, Nature **557**, 696 (2018).

[122] S. Papadopoulos, T. Agarwal, A. Jain, T. Taniguchi, K. Watanabe, M. Luisier, A. Emboras, and L. Novotny, *Ion Migration in Monolayer* MoS_2 *Memristors*, Phys. Rev. Applied **18**, 014018 (2022).

[123] M. Calderara, S. Brück, A. Pedersen, M. H. Bani-Hashemian, J. VandeVondele, and M. Luisier, *Pushing Back the Limit of Ab-initio Quantum Transport Simulations on Hybrid Supercomputers*, Proceedings of the International Conference for High Performance Computing, Networking, Storage and Analysis. , 1 (2018).

[124] A. Kuzmina, M. Parzefall, P. Back, T. Taniguchi, K. Watanabe, A. Jain, and L. Novotny, *Resonant Light Emission from Graphene/Hexagonal Boron Nitride/Graphene Tunnel Junctions*, Nano Lett. **21**, 8332 (2021).

[125] S. H. Oh, H. Altug, X. Jin, T. Low, S. J. Koester, A. P. Ivanov, J. B. Edel, P. Avouris, and M. S. Strano, *Nanophotonic biosensors harnessing van der Waals materials*, Nature Communications **12**, 1 (2021).

[126] T. Pham, G. Li, E. Bekyarova, M. E. Itkis, and A. Mulchandani, *MoS 2 -Based Optoelectronic Gas Sensor with Sub-parts-per-billion Limit of NO 2 Gas Detection*, ACS Nano **13**, 3196 (2019).

[127] Y. Ye, Z. J. Wong, X. Lu, X. Ni, H. Zhu, X. Chen, Y. Wang, and X. Zhang, *Monolayer excitonic laser*, Nature Photonics **9**, 733 (2015).

[128] E. Y. Paik, L. Zhang, G. W. Burg, R. Gogna, E. Tutuc, and H. Deng, *Interlayer exciton laser of extended spatial coherence in atomically thin heterostructures*, Nature **576**, 80 (2019).

[129] D. Kozawa, A. Carvalho, I. Verzhbitskiy, F. Giustiniano, Y. Miyauchi, S. Mouri, A. H. Castro Neto, K. Matsuda, and G. Eda, *Evidence for Fast Interlayer Energy Transfer in MoSe2/WS2 Heterostructures*, Nano Letters **16**, 4087 (2016).

[130] N. Flöry, P. Ma, Y. Salamin, A. Emboras, T. Taniguchi, K. Watanabe, J. Leuthold, and L. Novotny, *Waveguide-integrated van der Waals heterostructure photodetector at telecom wavelengths with high speed and high responsivity*, Nature Nanotechnology **15**, 118 (2020).

[131] A. Emboras, I. Goykhman, B. Desiatov, N. Mazurski, L. Stern, J. Shappir, and

U. Levy, *Nanoscale plasmonic memristor with optical readout functionality*, Nano Letters **13**, 6151 (2013).

List of Publications

This thesis is based in part on the following publications:

S. Papadopoulos, T. Agarwal, A. Jain, T. Taniguchi, K. Watanabe, M. Luisier, A. Emboras and L. Novotny, *Ion Migration in Monolayer MoS_2 Memristors*, Phys. Rev. Applied 18, 01401 (2022).

S. Papadopoulos *, L. Wang *, T. Taniguchi, K. Watanabe and L. Novotny, *Energy transfer from tunneling electrons to excitons*, arXiv: 2209.11641 (2022).

L. Wang *, **S. Papadopoulos** *, F. Iyikanat *, J. Zhang, J. Huang, T. Taniguchi, K. Watanabe, M. Galame, M. L. Perrin, F. J. Garcia de Abajo and L. Novotny, *Exciton assisted electron tunneling in van der Waals heterostructures*, just accepted in Nature Materials (2023).

* These authors contributed equally.

Other publications by the author:

Journals:

S. Busschaert, N. Flöry, **S. Papadopoulos**, M. Parzefall, S. Heeg and L. Novotny, *Beam steering with a nonlinear optical phased array antenna*, Nano Letters 19 (9), 6097-6103 (2019).

A. L. Luna, **S. Papadopoulos**, T. Kyburz, E. Tervoort, L. Novotny and M. Niederberger, *Insights into light and mass transport in nanoparticle-based aerogels: the advantages of monolithic 3D photocatalysts*, Journal of Materials Chemistry A 9 (39), 22380-22391 (2021).

Conferences:

K. Papke, U. van Rienen, **S. Papadopoulos**, E. Pilicer, F. Pillon, F.Gerigk, S. Horvath-Mikulas, *Mode sensitivity analysis of 704.4 MHz superconducting RF cavities*, 17th International Conference on RF Superconductivity, Whistler, Canada (2015)

S. Papadopoulos, J.M. Balula, F. Gerigk, J.M. Giguet, J. Hansen, A. Michet, S. Ramberger, N. Thaus, R. Wegner, *Experience with the Conditioning of Linac4 RF Cavities*, Proc. Linac'16 Conf., East Lansing (2016)

S. Papadopoulos, L. Dassa, J.P. Dequaire, F. Gerigk, F. Pillon, S. Ramberger, P. Yilmazer, *Sub-micro-Tesla Magnetic Shielding Design for Cryomodules in the High-gradient Program at CERN*, 18th Int. Conf. on RF Superconductivity (SRF'17), Lanzhou, China (2017)

Curriculum Vitae

Sotirios Papadopoulos, born on July, 31st, 1988

Professional Experience

2018–2022	Doctoral Student and Research Assistant ETH Zürich, Photonics Laboratory
2015–2018	Research Fellow at the European Organization for Nuclear Research (CERN)
2013–2014	Visiting Student Researcher, École Polytechnique Fédérale de Lausanne (EPFL), Group for Fiber Optics

Education

2014	Diploma in Electrical Engineering and Computer Science Aristotle University of Thessaloniki, Greece

Fellowships / Scholarships

2019	Stavros Niarchos Foundation Fellow
2014	AUTH-EPFL Scholarship